Validation of large eddy simulations for modeling micro-structured enhanced heat transfer surfaces

by

Puxuan Li

B.S., Ningbo University, 2009
M.S., McNeese State University, 2012

AN ABSTRACT OF A DISSERTATION

submitted in partial fulfillment of the requirements for the degree

DOCTOR OF PHILOSOPHY

Department of Mechanical and Nuclear Engineering
College of Engineering

KANSAS STATE UNIVERSITY
Manhattan, Kansas

2019

Abstract

The focus of this research is to investigate the relationship between the flow characteristics and heat transfer on enhanced surfaces. Internally enhanced surfaces, such as micro-fins, are an important class of heat transfer enhancement in commercial applications. Many research papers discuss the design and optima of these surfaces. However, most previous studies have demonstrated only the macro relationship between the geometries of the micro-fins and heat transfer. The need for a deeper understanding of these fins arose from some currently unsolved problems that limit future development of enhanced surfaces. First, why are increases of heat transfer larger than area increases in micro-finned tubes in most cases? Second, why do internally micro-finned tubes typically have lower heat-transfer-enhanced ratios in laminar and transition flows?

First, a comprehensive literature review on internal micro-fins is conducted in this dissertation. Previous experimental and numerical results of internal micro-fins are addressed in the chapter. Second, the dissertation introduces comprehensive experimental measurements including particle image velocimetry (PIV), measurement of the heat transfer coefficient, and accuracy of pressure-drop measurements. Third, validated numerical simulations are then used to predict flow characteristics and heat transfer. Large eddy simulations (LES) are mainly applied to the numerical simulations. The setup of inlet conditions for a LES is a complex and important problem if an accurate numerical result is desired. In this study, PIV results are incorporated into boundary conditions of LES. Parallel processing is an effective computation strategy in which many calculations are carried out simultaneously. In this dissertation, effects of shared-memory parallel processing on LES are presented. The numerical simulations are conducted in the duct with smooth surfaces and enhanced surfaces. The numerical simulation includes both heat

conduction in the metal structure and heat convection on the solid-fluid interface. Finally, the dissertation documents how the flow characteristics link with the enhancement of heat transfer in the micro-finned duct, which answers the two problems mentioned in the beginning.

The study in the dissertation shows that: (1) a method for generating inflow boundary conditions in a square duct by using PIV measurement results is developed. The new method of generating boundary conditions for LES satisfies the features of good boundary conditions. (2) a new numerical model with LES is used to study the relationship between flow characteristics and heat transfer in a square duct with micro-fins. Good agreements are found when the experimental results are compared to the numerical simulation results.

Validation of large eddy simulations for modeling micro-structured enhanced heat transfer surfaces

by

Puxuan Li

B.S., Ningbo University, 2009
M.S., McNeese State University, 2012

A DISSERTATION

submitted in partial fulfillment of the requirements for the degree

DOCTOR OF PHILOSOPHY

Department of Mechanical and Nuclear Engineering
College of Engineering

KANSAS STATE UNIVERSITY
Manhattan, Kansas

2019

Approved by:

Major Professor
Steven Eckels

Copyright

Abstract

The focus of this research is to investigate the relationship between the flow characteristics and heat transfer on enhanced surfaces. Internally enhanced surfaces, such as micro-fins, are an important class of heat transfer enhancement in commercial applications. Many research papers discuss the design and optima of these surfaces. However, most previous studies have demonstrated only the macro relationship between the geometries of the micro-fins and heat transfer. The need for a deeper understanding of these fins arose from some currently unsolved problems that limit future development of enhanced surfaces. First, why are increases of heat transfer larger than area increases in micro-finned tubes in most cases? Second, why do internally micro-finned tubes typically have lower heat-transfer-enhanced ratios in laminar and transition flows?

First, a comprehensive literature review on internal micro-fins is conducted in this dissertation. Previous experimental and numerical results of internal micro-fins are addressed in the chapter. Second, the dissertation introduces comprehensive experimental measurements including particle image velocimetry (PIV), measurement of the heat transfer coefficient, and accuracy of pressure-drop measurements. Third, validated numerical simulations are then used to predict flow characteristics and heat transfer. Large eddy simulations (LES) are mainly applied to the numerical simulations. The setup of inlet conditions for a LES is a complex and important problem if an accurate numerical result is desired. In this study, PIV results are incorporated into boundary conditions of LES. Parallel processing is an effective computation strategy in which many calculations are carried out simultaneously. In this dissertation, effects of shared-memory parallel processing on LES are presented. The numerical simulations are conducted in the duct with smooth surfaces and enhanced surfaces. The numerical simulation includes both heat

conduction in the metal structure and heat convection on the solid-fluid interface. Finally, the dissertation documents how the flow characteristics link with the enhancement of heat transfer in the micro-finned duct, which answers the two problems mentioned in the beginning.

The study in the dissertation shows that: (1) a method for generating inflow boundary conditions in a square duct by using PIV measurement results is developed. The new method of generating boundary conditions for LES satisfies the features of good boundary conditions. (2) a new numerical model with LES is used to study the relationship between flow characteristics and heat transfer in a square duct with micro-fins. Good agreements are found when the experimental results are compared to the numerical simulation results.

Table of Contents

List of Figures

List of Tables

Acknowledgements

Funding for this research was partially obtained from the Institute for Environmental Research (IER). IER is a multidisciplinary research group focused on heat transfer and interactions of humans with the environment. Research on human interactions with environment focus on clothing and personal cooling systems [1]–[7]. Heat transfer research ranges from work on environmentally friendly refrigerants [8]–[16] to enhanced heat transfer surfaces [17]–[21]. IER allowed me to explore research without restraint and, while it wasn't always successful, I was always learning new things.

I would like to thank my advisor Professor Steven Eckels for his endless support. Steven was a great listener and placed the well-being of his students, while always pushing us to be our best. Thanks to my lab mates in the past and present: Matthew Campbell and Garrett Mann. I also would like to appreciate the useful help from our research group of enhanced heat transfer. A special thanks to Dr. Ning Zhang, Shima Soleimani, Hatim Alrifaai and Seth Heronemus.

Dedication

This dissertation is dedicated to my father (Dali Li), my mother (Chao Peng), my wife (Yuqi Song) and my daughter (Abby Lee). Thank you all for helping to give me the life I love today.

Chapter 1 - Introduction

1.1. Introduction of internal micro-finned tubes

Fig. 1.1 shows a tube with a certain number and shape of protruding micro-fins. Internally micro-finned tubes used for heat transfer enhancement have become important in many commercial applications, such as air conditioners and refrigerators, due to the relatively low cost of production, reliability and low pressure drop. The goal of the design for micro-fins is to increase heat transfer with a minimum pressure drop penalty. The weaknesses of the internal integral finned tubes are the lower heat transfer enhanced ratio at lower Reynold number, such as laminar and transition flow region. The liquid used the systems must be as clean as possible to avoid depositions.

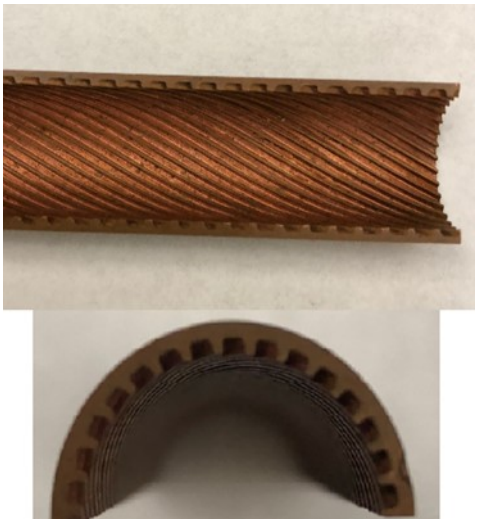

Figure 1.1: Micro-finned Tubes

To depict different kind of micro-fins, the geometric parameters of finned tube include the internal diameter of tube (d_i), inner fin height (e), number of starts (N_s), helix angle (α), fin base thickness (t_b), fin pitch ($pi, \pi d_i/N_s$) [22] and wall thickness (δ_t). Normally, the parameters of internally-finned tube are within the range of $0.01 \leq e/d_i \leq 0.4$, $1 \leq N_s \leq 82$, $1.5 \leq pi/e \leq$

46.7, $1.5 \leq t_b/e \leq 2.5$, and $0^\circ \leq \alpha \leq 90^\circ$. The above parameters have significant effects on heat transfer coefficient in the turbulent flow regime. With the increment of e/d_i, N_s, or α, both the friction factor and Nusselt number increase [23]–[25], and the effects are nonlinear. High-height fins are mainly used for fluids that have lower convective heat transfer coefficients or that with high viscosity.

1.2 Correlations for heat transfer coefficient and friction factor

Due to the complexity of turbulent flow, the predictions on the heat transfer and friction factors still mostly rely on empirical correlations. The correlations can be derived from similarity theory or dimensional analysis based on the experimental data.

As early as 1950, Nikuradse [26] firstly established the correlation for friction factors of internally roughed tube. The friction similarity law of Nikuradse was shown as follow:

$$\bar{B}(e^+) = \sqrt{2/f} + 2.5 \ln\left(\frac{2e}{d_i}\right) + 3.75 \tag{1.1}$$

Where e^+ the roughness Reynolds number, $e^+ = \frac{eu^*}{\nu} = (e/d_i)Re\sqrt{f/2}$, and $\bar{B}(e^+)$ was a friction similarity function determined empirically. It was a constant of 8.48 when $e^+ > 70$. Based on the above correlation, in 1963, Dipprey et al. [27] developed a friction correlation and a heat transfer correlation for smooth and granular roughed tubes. The correlations were written as:

$$f = 2[2.5 \ln\left(\frac{d_i}{2e}\right) - 3.75 + \bar{B}(e^+)]^{-2} \tag{1.2}$$

$$Nu = \frac{(f/2)RePr}{1+\sqrt{f/2}[\bar{g}(e^+)Pr^n - \bar{B}(e^+)]} \tag{1.3}$$

Where $\bar{g}(e^+)$ was a dimensionless heat transfer similarity function, which depended on different types of roughness. The validation range was $1.20 \leq Pr \leq 5.94$. The deviation was $\pm 10\%$. The fluid was water. Then Webb et al. [28] suggested that the heat-momentum transfer analogy should

be applicable to any basic type of roughness. Webb et al. developed new correlations for repeated transverse ribs as follow:

$$f = 2[2.5\ln\left(\frac{d_i}{2e}\right) + 0.95\left(\frac{pi}{e}\right)^{0.53} - 3.75]^{-2} \tag{1.4}$$

$$Nu = \frac{(f/2)RePr}{1+\sqrt{f/2}[4.5(e^+)^{0.28}Pr^{0.57}-0.95(pi/e)^{0.53}]} \tag{1.5}$$

The validation range was $6000 \le Re \le 100000$ and $0.71 \le Pr \le 37.6$. The deviation was $\pm 11\%$. The correlation was suitable for air, water and n-butyl alcohol. According to different conditions, Han et al. [29] developed new correlations for repeated transverse ribs in 1987. The correlations were shown as:

$$f = 2(Re^+ - 2.5\ln\left(\frac{2e}{d_h}\right) - 3.75)^{-2} \tag{1.6}$$

Where $Re^+ = 4.9\left(\frac{e^+}{35}\right)^m/[(\alpha/90^\circ)^{0.35}(\frac{10}{pi}/e)^n(\beta/45)^{0.57}]$. If $e^+ < 35$, $m = -0.4$; If $e^+ \ge 35$, $m = 0$; If $pi/e < 10$, $n = -0.13$; If $pi/e \ge 10$, $n = 0.53(\beta/90^\circ)^{0.71}$. The correlation for heat transfer as:

$$Nu = \frac{fRePr}{[He^+ - Re^+]2f^{1/2}+2} \tag{1.7}$$

Where $He^+ = 10(e^+/35)^i/(\alpha/45^\circ)^j$. $i = 0$, when $e^+ < 35$; $i = 0.28$, when $e^+ \ge 35$; $j = 0.5$, when $\beta < 45^\circ$; $j = -0.45$, when $\beta \ge 45^\circ$. The validation range was $7.5 \times 10^4 \le Re \le 2 \times 10^5$. The deviation was $\pm 40\%$. The fluid was air. In 1980, Gee and Webb et al. [30] improved the

correlation for transverse and helical ribs. They tried different helix angles (30°, 49° and 70°). Their correlations were shown as:

$$f = 2\left[\frac{\bar{B}(e^{+},\alpha)}{\left(\frac{\alpha}{50}\right)^{0.16}} - 2.5\ln\left(\frac{2e}{d_i}\right) - 3.75\right]^{-2} \tag{1.8}$$

$$Nu = \frac{1.42\left(\frac{f}{2}\right)^{0.5} RePr}{1+\sqrt{\frac{f}{2}}\left[\frac{\bar{g}(e^{+},Pr,\alpha)}{\left(\frac{\alpha}{50}\right)^{j}} - \bar{B}(e^{+},\alpha)\right]} \tag{1.9}$$

Where $\bar{B}(e^{+},\alpha)$ was friction similarity function and $\bar{g}(e^{+},Pr,\alpha)$ was heat transfer similarity function. $j = 0.37$, when $\alpha < 50^{\circ}$. $j = -0.16$, when $\alpha > 50^{\circ}$. The validation range was $Pr = 0.71$ and $6 \times 10^{3} \leq Re \leq 6.5 \times 10^{4}$. The fluid was air. In 1996, Wang et al. [31] tested helical fins with different parameters. The ranges of parameters were $7.00\text{ mm} \leq d_o \leq 9.52\text{ mm}$, $6.46\text{ mm} \leq d_i \leq 8.96\text{ mm}$, $0.15\text{ mm} \leq e \leq 0.2\text{ mm}$, $17^{\circ} \leq \alpha \leq 25^{\circ}$ and $0.26\text{ mm} \leq \delta_t \leq 0.8\text{ mm}$. The fluid was water. The correlations were shown as:

$$f = 2\left(\frac{d_i e^{+}}{e}\right)^{2} Re^{-2} \tag{1.10}$$

$$Nu = \frac{fRePr}{2\left(1+\sqrt{\frac{f}{2}}[\bar{g}(e^{+})Pr^{n} - B(e^{+})]\right)} \tag{1.11}$$

Where $e^{+} = 0.1407 + 0.093675X_f + 0.58464/\ln(X_f)$. For $e^{+} \leq 23$, $e^{+} = 0.07313 + 0.09571X_f$; for $e^{+} > 23$, $X_f = Re(\frac{e}{d_i+0.005})\frac{Ns^{0.25}}{(cos\alpha)^{0.5}}$. Furthermore, $B(e^{+}) = \exp(y_b)\,X_b, y_b = 2.45805 - 0.987261ne^{+}$, $X_b = Re\left(\frac{e}{d_i}\right)\frac{\cos x}{n_f^{0.7}}$, $B(e^{+}) = y_g Xg$, and $Xb = \frac{n_f(tg\alpha)^{0.1}}{(\frac{e}{d_i})^{0.4}}$. For $e^{+} \leq 23$, $y_g = 0.007705 + 0.321(lne^{+})/e^{+}$; for $e^{+} \geq 23$, $y_g = 0.06501 - \frac{0.51903}{e^{+}} + 5.5956/(e^{+})^{2}$.

Regression of experimental data among some dimensionless parameters was mainly used to obtain the other correlations. In 1980, Carnavos [32] collected the heat transfer characteristics of water and air in turbulent flow for 11 tubes having longitudinal and helical integral fins. The

ranges of the parameters were 8 mm $\leq d_i \leq$ 22.2 mm, $6 \leq N_s \leq 38$, 0.6 mm $\leq e \leq$ 2 mm, $0 \leq \alpha \leq 30^{\circ}$ and 0.26 mm $\leq \delta_t \leq$ 0.8 mm. The fluids were air, water and ethylene glycol-water. The validation ranges were $1 \times 10^4 \leq Re \leq 10^5$ and $0.7 \leq Pr \leq 30$. The deviation was within $\pm 10\%$. The correlations were:

$$f = 0.046Re^{-0.2}(F^*)^{-1} \tag{1.12}$$

$$Nu = 0.023Re^{0.8}Pr^{0.4}(F) \tag{1.13}$$

Where $F^* = (A_{fa}/A_{fn})^{0.5}(sec\alpha)^{0.75}$ and $F = (A_{fa}/A_{fn})^{0.1}(A_n/A_a)^{0.5}(sec\alpha)^3$. The correlation worked well for tubes with a higher helix angle and a larger internal heat transfer surface area. However, it was not suitable for the higher helix angles with lower Reynold numbers.

Nusselt number and friction factor were also correlated with some detailed geometric parameters, such as e/d_i, pi/e, and α. In 1996, Ravigururajan and Bergles [33] developed a correlation based on experimental data in 17 research papers. The ranges of the internally finned parameters are $0.01 \leq e/d \leq 0.2$, $0.1 \leq pi/d \leq 7.0$, $0.3 \leq \alpha/90^0 \leq 1.0$, $5000 \leq Re \leq 250000$, and $0.66 \leq Pr \leq 37.6$. It was claimed that the correlation for friction could predict 96% of the database (1658 points) within the deviations of $\pm 50\%$ and 70% database within $\pm 20\%$ deviations. For the equation of Nusselt number, prediction results were within $\pm 50\%$ for 99% of the data (18070 points) and 69% within $\pm 20\%$. The correlations were shown as:

$$\frac{f}{f_p} = 0.25 \times \{1 + [29.1Re^{\left(0.67 - \frac{0.06pi}{d} - \frac{0.49\alpha}{90}\right)} \times \left(\frac{e}{d}\right)^{\left(1.37 - \frac{0.157pi}{d}\right)} \times \left(\frac{pi}{d}\right)^{\left(-1.66Re \times 10^{-6} - 0.15\frac{pi}{d}\right)} \times \left(1 + 2.94\sin\left(\frac{45}{N_s}\right)\right)]^{15/16}\}^{16/15} \tag{1.14}$$

$$\frac{Nu}{Nu_p} = \{1 + [2.64Re^{0.036}(e/d)^{0.212} \times (pi/d)^{-0.21} \times (\alpha/90)^{0.29}(Pr)^{0.024}]^7\}^{1/7} \tag{1.15}$$

Webb et al. [34] developed a new correlation for 7 tubes with helical ribs by the same way. The ranges of the geometries were $0.024 \leq e/d_i \leq 0.041$, $2.39 \leq pi/e \leq 12.84$, $25^{\circ} \leq \alpha \leq 45^{\circ}$,

and $\frac{t_t}{d_i} = 0.015$ (t_t is fin tip thickness). They claimed the deviations within 2.9% for friction factor and 3.8% for Nusselt number of the 7 tubes. After that, Wang and Rose [35] established a comprehensive database of friction factor for internal micro-finned tubes. The database was used to evaluate the friction correlations of Carnavos [32], Ravigururajan and Bergles [33], Wang et al. [35], Jensen and Vlakancic [23], and Webb et al. [34]. They indicated that the correlation of Jensen and Vlakancic [23] was the best and represented most of the database within $\pm 21\%$ deviation.

Generally, we can assume the increase in friction factor leads to an increase in heat transfer for internally grooved tubes. The correlation of Ji et al. [36] was based on this assumption. The ranges of the tube geometries were $1 \leq N_s \leq 45$, $0.016 \leq e/d_i \leq 0.04$, and $13^{\circ} \leq \alpha \leq 45^{\circ}$. The correlation was good for $10000 \leq Re \leq 100000$ and $4.98 \leq Pr \leq 8.22$. It was claimed that the deviation of more than 89% of data was within $\pm 20\%$. The correlations were shown as:

$$f = \frac{\Delta p d_i}{2L\rho v^2} \tag{1.16}$$

$$Nu = \frac{\left(\frac{f}{8}\right)(Re-1000)Pr}{1+12.7\left(\frac{fp}{8}\right)^{\frac{1}{2}}(Pr^{\frac{2}{3}}-1)}[1+(d_i/L)^{2/3}]\left(\frac{Pr}{Pr_w}\right)^{0.11} \tag{1.17}$$

The correlation above was similar with that created by Kader and Yaglom [37].

1.3. Experimental results of internally finned tube

It should be noted that more than 90% of experimental data of plain tube agree with Dittus–Boelter and Fanning equations with the deviations of $\pm 20\%$ [22]. Dittus-Boelter equation proposed by Incropera [38]:

$$Nu = 0.023 Re^{0.8} Pr^n \tag{1.18}$$

And Fanning equation [39] as:

$$f = 0.079 Re^{-1/4} \tag{1.19}$$

It was noted that more than 90% of experimental data of plain tube in the survey agree with these two equations with the deviations of $\pm 20\%$. Experimental studies of internally-finned tube with different geometrical parameters were reported in the literature [22]. Reynolds number in the research was within the range from 2500 to 100,000, mostly in the turbulent flow region. Test fluids included water, air, oil, and refrigerant, with most data being of water.

The experimental system usually was a closed liquid loop. The loop consisted a pump, liquid storage tank, flow meter, temperature and pressure drop transducers. The liquid temperature and stability were precisely controlled before entering the test section. The system also included the liquid heating or cooling system for the test section [22].

The history of experimental data of internally finned tubes for water flow is shown in this paragraph. In 1996, Wang et al. tested 7 micro-fins. The ranges of friction enhancement and heat enhancement were $1.5 \leq f/f_r \leq 2.2$ and $0.8 \leq Nu/Nu_r \leq 2.1$. The feature of the best tube was $\frac{e}{d_i} = 0.022$, $N_s = 60$, $\frac{pi}{e} = 7.22$, $\alpha = 18^\circ$ and $d_i = 8.96\,\text{mm}$. In 1997, Brognaux et al. [40] improved Wang et al.'s design. Brognaux et al. tested 6 micro-fins. The enhancement of friction and heat transfer became $1.1 \leq f/f_r \leq 1.7$ and $1.6 \leq Nu/Nu_r \leq 1.8$. The best feature was $\frac{e}{d_i} = 0.036$, $N_s = 78$, $\frac{pi}{e} = 1.66$, $\alpha = 22^\circ$ and $d_i = 14.57\,\text{mm}$. In 2000, Webb et al. [34] tested 7 micro-fins. The heat transfer enhancement was increased to 2.2-2.3. However, the friction was also increase to 2.1-2.4. The best geometry for the design was $\frac{e}{d_i} = 0.021$, $N_s = 45$, $\frac{pi}{e} = 2.81$, $\alpha = 45^\circ$ and $d_i = 15.54\,\text{mm}$. In 2004, Copetti et al. [41] designed a micro-fin for low Reynolds number, $0 \leq Re \leq 20 \times 10^3$. Their tube was wrapped up with an electrical resistance tape to supply a constant heat flux to its surface. The micro-fin tube provided higher heat transfer performance than the smooth tube ($\frac{Nu}{Nu_r} = 2.8$). In spite of the increase, the friction was increased

less ($\frac{f}{f_r} = 1.9$). The parameters for the micro-fin were $\frac{e}{d_i} = 0.022$, $N_s = 60$, $\frac{pi}{e} = 2.34$, $\alpha = 18^{\circ}$ and $d_i = 8.95$ mm. In 2005, Han and Lee [42] designed 4 different micro-finned tubes with varying Re (3000-40000). From the point of efficiency index, the tube with higher relative roughness and smaller spiral angle showed better heat transfer performance than the tube with larger spiral angle and smaller relative roughness. The parameters for the best design were $\frac{e}{d_i} = 0.013$, $N_s = 60$, $\frac{pi}{e} = 8.33$, $\alpha = 25^{\circ}$ and $d_i = 8.92$ mm. In 2006, Naphon and Sriromruln [43] designed a micro-fin for horizontal double pipes with and without coiled wire. The test runs were performed at the cold and hot water mass flow rates ranging between 0.01 and 0.07 kg/s and between 0.04 and 0.08 kg/s, respectively. The results obtained from the micro-fin tube with coiled wire insert were compared with those obtained from the smooth and micro-fin tubes. Nu/Nu_r was only 1.0-1.3. The features of the micro-fin were $\frac{e}{d_i} = 0.022$, $N_s = 60$, and $d_i = 8.92$ mm. In 2008, Siddique and Alhazmy [44] investigated heat transfer and pressure drop characteristics of a commercially available internally micro-finned tube with a nominal outside diameter of 7.94 mm. Data were taken for turbulent flow with $3300 \leq Re \leq 22500$ and $2.9 \leq Pr \leq 4.7$. The parameters for the micro-fin were $\frac{e}{d_i} = 0.027$, $N_s = 50$, $\alpha = 18^{\circ}$ and $d_i = 7.3$ mm. It was found that the Nusselt numbers obtained from the present correlation fall in the middle region between the Copetti et al. and the Gnielinski smooth tube correlation predicted Nusselt number values. For friction, the correlation predicted friction factors values were nearly double that of the Blasius smooth tube correlation predicted friction factors. The enhancement of friction and heat transfer were $1.6 \leq f/f_r \leq 2.0$ and $1.0 \leq Nu/Nu_r \leq 2.1$. In the same year, Zdaniuk et al. [24] tested 8 helically-finned tubes and 1 smooth tube using liquid water at Reynolds numbers ranging from 12,000 to 60,000. Power-law correlations for Fanning friction and Colburn j-factors were

developed using a least-squares regression. The performance of the correlations was evaluated with data of other researchers with average prediction errors between 30% and 40%. In 2012, Ji et al. [36] tested 16 internally micro-finned tubes with different geometrical parameters. Experiments were conducted for the 16 tubes with the Reynolds number range from 10,000 to 100,000 and Prandtl number from 4.98 to 8.22. Other parameter ranges were: $1 \leq N_s \leq 45$, $0.016 \leq e/d_i \leq 0.04$, and $13^\circ \leq \alpha \leq 45^\circ$. The best feature was $\frac{e}{d_i} = 0.021$, $N_s = 45$, $\alpha = 40^\circ$ and $d_i = 16.61$ mm. Nu/Nu_r was 2.9 and f/f_r was from 2.9 to 3.2. An equation for predicting the average heat transfer of the inner helically ribbed tubes was presented based on Gnielinski equation with the friction factor in the numerator of the original Gnielinski equation being replaced by the measured friction factor in the fully developed flow region of the internally grooved tubes. As shown in the history, the largest heat transfer enhancement ratio of the internally micro-finned tube was 2.9, and that of friction factor was 3.2. The largest enhancement ratios of heat transfer and friction factors were roughly the same for the internally finned tubes.

1.4. Numerical results of internally finned tube

Since the micro-fin tube was first developed, there were numerous numerical investigations on the micro-fins. Patankar et al. [45] carried out one of the earliest numerical investigations on turbulent flow and heat transfer in axial finned tubes. In 1999, Liu and Jensen [46] modeled periodically fully developed, single-phase turbulent flow and heat transfer in two helical finned tubes. The parameters for the two micro-fins: (1) $\frac{e}{d_i} = 0.015$, $\alpha = 30^\circ$, $N_s = 30$; (2) $\frac{e}{d_i} = 0.05$, $\alpha = 30^\circ$, $N_s = 8$. The range of the Reynolds number was from 6000 to 70000. The Prandtl number was 4. In 2000, Webb et al. [34] numerically predicted heat transfer and friction losses for micro-finned tubes using the commercial CFD program, Fluent. *k-ε* turbulence models were used in their numerical simulations. The fiction losses were predicted for five tube geometries. The prediction

fiction factor was within $\pm 13\%$ of the experimental values. The heat transfer simulation was done for only one tube geometry with helix angle of 17.5°. The simulation was carried out for $1 < Pr < 4$. The Nusselt number was over predicted, ranging from 29% to 55% as the Prandtl number was increased from 1 to 4. The numerical results for 14.9 mm tube internal diameter showed an increasing trend in fiction factor and Nusselt number with helix angle and fin height. The results also showed little dependence on the width of the fin tip, and apex angle for the range simulated. In 2007, Ryu et al. [47], [48] studied the flow characteristics and heat-transfer characteristics in channels with micro-fins. Reynolds-averaged Navier–Stokes equations (RANS), coupled with k-ε turbulence models, were solved by a finite-volume method. The friction function depended on the micro-fin shapes and the pitch ratio. In 2016, Dupuis et al. [49] identified and analyzed flow structures in pyramidal-pin fin arrays with k-ε turbulence models. Their fins were sprayed on aluminum substrates with dimensions of 7 mm × 51 mm. Fin height was 1.0 mm, and fin base length was 1.5 mm. The flow in their study was pure nitrogen. Flow structures obtained in the micro-channel affected flow stability, structure and turbulence level, which contributed to the increase of the convective heat transfer coefficient. In 2017, Xia et al. [50] presented numerical simulations of the laminar-flow behavior of water in circular micro pin-fin, square micro pin-fin and diamond micro pin-fin heat sinks with PIV. The entire dimension with the micro-pin fin arrays was 10 mm (length) × 2.2 mm (width) × 0.1 mm (height). Vortexes in their study explained why the best heat transfer enhancement behaviors were in the diamond micro pin-fin heat sink. With an increasing Reynolds number, vortexes in the diamond micro pin-fin occurred the earliest and had the most complicated structure, which effectively improved the mixing of fluid and heat transfer.

Previously, there had been numerous numerical investigations of the micro-fins [47]–[49], [51]–[54]. *k*-*ε* turbulence models were used in most of the papers mentioned above. However, two drawbacks existed in the turbulence model. First, the *k*-*ε* turbulence model was not suitable for the laminar and transition flow region of micro-fin flows, which led to faulty predictions of heat transfer and pressure drops [55]. Second, the turbulence model developed from Reynolds Averaged Navier–Stokes equations (RANS) was not able to simulate the dynamic process of fluid mixing caused by flow separation and reattachment within the inter-fin region. The authors were aware of only a few systematic studies in the literature on implementing LES in wall-bounded flows with heat transfer in micro-fins. In 2003, Cui et al. [56] used large eddy simulations (LES) to simulate the flow in 2D channel with ribs. They showed that a logarithmic layer existed in the space-average velocity distributions some distance above the ribs. They also identified the location of the so-called virtual origin with the position of zero space-average velocity. Similar studies were reported by Miyake et al. [57] and Ikeda and Durbin [58]. In 2019, Campet et al. [54] presented a LES approach to study the turbulent flow in a single-started helically ribbed tube.

Optimization with numerical simulations faces various problems. First, the significant computational cost is a big challenge. Thus, the optimum for one system may not be broadly applicable to many different design scenarios. One way to produce optimization results that are more general is to consider the problem explicitly as a multi-objective optimization. The goal of such a problem is to find the Pareto front (i.e., the set of all non-dominated solutions). The Pareto front thus represents all possible optimal solutions over the design space and can be computed without selecting the relative importance of the objectives [21]. Common multi-objective optimization genetic algorithms (MOGA) combine the non-dominated sorting genetic algorithm II (NSGA-II) [59] with the strength Pareto evolutionary algorithm 2 (SPEA2) [60]. MOGAs have

been applied to entire heat exchangers in several studies including optimization of shell-and-tube [61]–[65], compact [66]–[68], fin and tube [69], and plate heat exchangers [70]–[72], all of which use some form of correlation to evaluate the objectives. Studies can be found evaluating the objectives using higher-accuracy computational fluid dynamics (CFD) simulation.

1.5. Outline

The experimental apparatuses are described in chapter 2 of this dissertation. The measurements and uncertainty analysis for heat transfer coefficient (*HTC*), pressure drop, and velocity are discussed briefly. Chapter 3 introduces the numerical simulations for the study. LES is sensitive with inlet boundary conditions. Chapter 4 proposes a new method to incorporate PIV data to LES boundary conditions directly. The numerical simulations were conducted in ANSYS Fluent. Chapter 5 tests the effect of parallel processing on LES in Fluent. Chapter 6 is to validate the experimental and numerical results in a smooth duct, which can be a benchmark for the start of micro-finned tubes. Chapter 7 investigates the relationship between turbulent structures and heat transfer in micro-fin enhanced surfaces. Finally, chapter 8 concludes and proposes future work.

Chapter 2 - Experimental Set-up

2.1. Water Loop

The system as shown in Fig. 2.1 [18] consists of two connected loops: the by-pass loop and the test section loop. A 1/3 hp centrifugal water pump drives the system. A heat exchanger is installed in the by-pass loop to remove the heat generated in the system. The majority of the system is built with 15.9 mm copper tubes. Each of these loops utilizes a 12.7 mm gate valve to control the flow of water through the test section. A pressure transducer is connected to the test section to measure pressure drops. A Micro Motion CFM025 flow meter measures the flow rate through the test section, with an uncertainty of ±0.1%. Average bulk velocities in the duct are calculated from the measured flow rate.

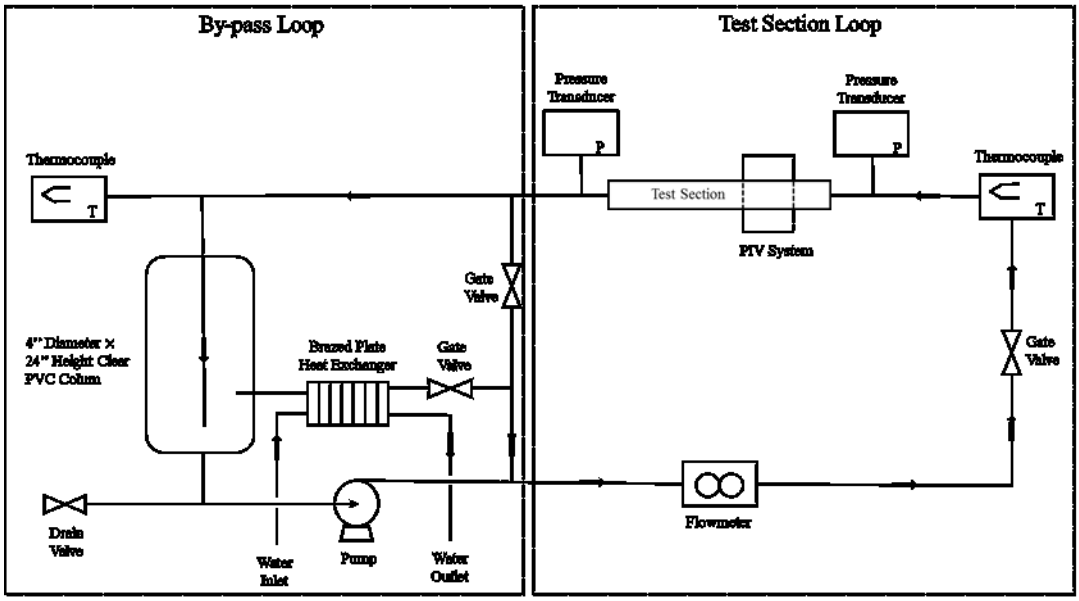

Figure 2.1: Schematic for water flow loop

2.2. Test Section

The primary test section is a square channel with clear upper and side walls on a solid copper block as shown schematically in Fig. 2.2 (a). The cross-section of the channel is 15.2 mm

square and 609.6 mm long. The test section has an extended length to allow the study of the hydrodynamic fully developed region. Water flows in the direction of the arrow, which is in the direction of X-axis. PIV collected the experimental results at the fully developed region in zoom-in rectangular, and its distance from the entrance is approximately 460 mm. The range of the Reynolds numbers is from 7600 to 28000. Fig. 2.2 (b) is a zoom-in view at the micro-fins. The micro-fins have a 45° helix angle. Fig. 2.2 (c) illustrates the schematic for the micro-fins with dimensions. The height of the micro-fins is 0.33 mm.

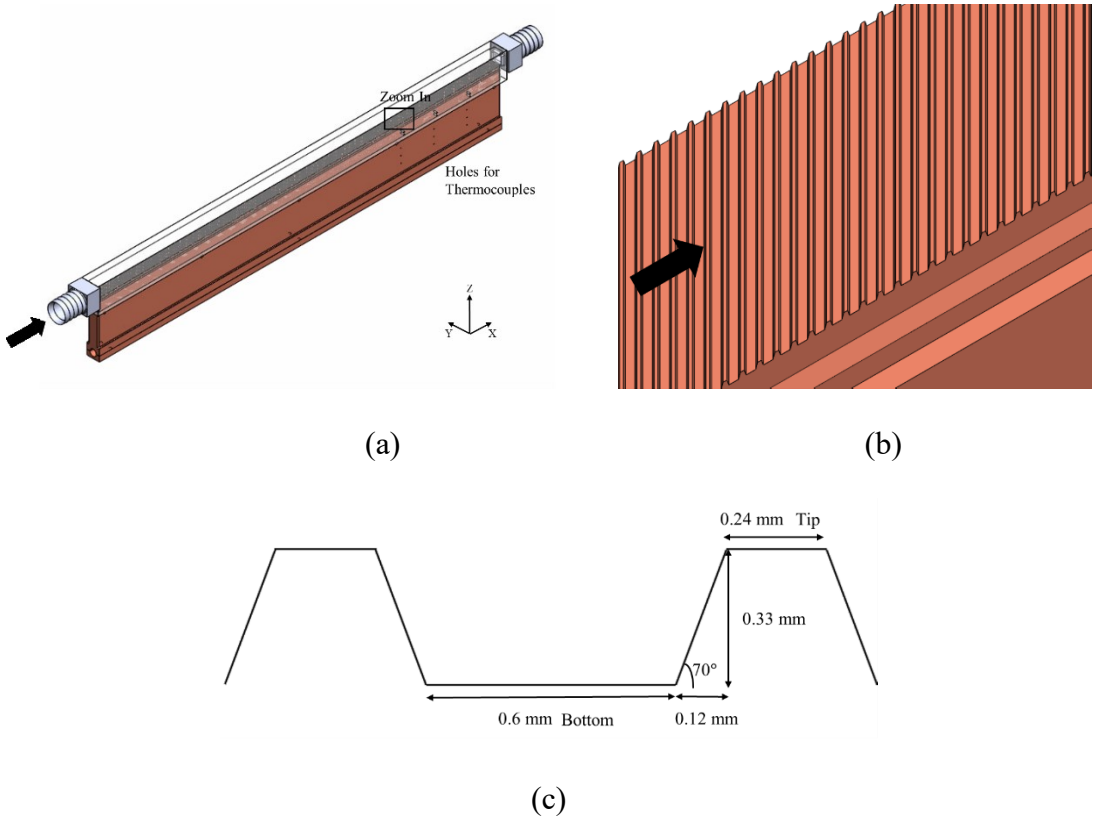

Figure 2.2: (a) schematic for test section (b) zoom-in view at micro-fins (c) schematic for micro-fins

2.3. Measurement of Heat Transfer Coefficient

The convective heat transfer coefficient (*HTC*) was measured as a semi-local surface average [73], [74]. The heat transfer coefficient is calculated by:

$$HTC = \frac{q''}{\Delta T} \tag{2.1}$$

q'' is the amount of heat flux, which is determined by the temperature distribution in the solid copper block. ΔT is the difference between the surface temperature and the water flow temperature. Two high-power heaters are installed in the system. Furthermore, the test section is isolated by the wood boards. We assume that the heat conductivity in the copper block is linear. Therefore, the heat flux, q'', is determined from the following equation:

$$q'' = -k\frac{dT(z)}{dz} \tag{2.2}$$

k is the thermal conductivity for the copper block, z represents the locations of the thermocouples and T represents the temperatures corresponding to the thermocouples. In Fig. 2.2 (a), there are three columns of thermocouple holes at the downstream of the duct. There are 6 thermocouples in each column. The distance between the first top hole and the surface is 2.3 mm. The interval between each hole is 10 mm. Linear regression as follow is used to predict the heat flux and the surface temperature:

$$a = \bar{z} - b\overline{T} \tag{2.3}$$

$$b = \frac{\sum_{i=1}^{6}(T_i - \bar{T})(z_i - \bar{z})}{\sum_{i=1}^{6}(T_i - \bar{T})^2} \tag{2.4}$$

a in Eq. 2.3 is the z-intercept and b in Eq. 2.4 is the slope of the linear regression.

2.4. Measurement Uncertainties for *HTC*

Uncertainty analyses were performed for *HTC* and PIV measurements to judge the accuracy of the experimental results. Based on the calculation of *HTC* in chapter 2.3, the uncertainty of *HTC* was determined by

$$UN_{HTC} = [(\frac{\partial HTC}{\partial un_{q''}} \cdot un_{q''})^2 + (\frac{\partial HTC}{\partial un_{T_{surf}}} \cdot un_{T_{surf}})^2 + (\frac{\partial HTC}{\partial un_{T_{flow}}} \cdot un_{T_{flow}})^2]^{1/2} \tag{2.5}$$

where the un is an uncertainty of each source. Due to the heat flux and surface temperature were calculated by linear regression. Eq. 2.5 is converted to the following format:

$$UN_{HTC} = [\left(\frac{\partial HTC}{\partial un_a} \cdot un_a\right)^2 + \left(\frac{\partial HTC}{\partial un_b} \cdot un_b\right)^2 + (\frac{\partial HTC}{\partial un_z} \cdot un_z)^2 + (\frac{\partial HTC}{\partial un_{T_{flow}}} \cdot un_{T_{flow}})^2]^{1/2} \quad (2.6)$$

Table 2.1 shows an example of the *HTC* uncertainty calculation for a case (inlet velocity ≈ 0.5 m/s). In this cases, k was 345.8 $\mathrm{W/(m \cdot K)}$, T_{flow} was 293.6 K, a was 60.5 m, b was -192.9 $\mathrm{m/K}$, and Z_{surf} was 0.052 m. Fluke 7321, a compact constant temperature bath, was used to calibrate the thermocouples. The uncertainty of the thermocouples was $\pm$0.2 K. 95% confidence interval was used to estimate the uncertainties for a and b. We got a total uncertainty after we substituted the estimated uncertainties into Eq. 2.6. The total uncertainty for the case was $\pm 73.2\ \mathrm{W/m^2 \cdot K}$. The average *HTC* was 2236.2 $\mathrm{W/m^2 \cdot K}$. Therefore, the relative uncertainty was $\pm$3.3%.

Table 2.1: Uncertainties on *HTC* Measurement

Uncertainty Source	Uncertainty Weight		Estimated Uncertainty (UN)
a	$\frac{\partial HTC}{\partial un_a}$	-74.35	0.0570
b	$\frac{\partial HTC}{\partial un_b}$	37.77	1.8835
z	$\frac{\partial HTC}{\partial un_z}$	14342.41	0.0005
T_{flow}	$\frac{\partial HTC}{\partial un_{T_{flow}}}$	74.35	0.2
Total Uncertainty			73.2
Relative Uncertainty			3.27 %

Maximum *HTC* uncertainty was approximately $\pm$4%. The main uncertainty for the *HTC* measurement was from the slope of the linear regression, b. The linear slope increased as the power

of the heater increased, which led to the decrease of slope uncertainty. Uncertainty for *HTC* was low because a high-power heater was used in the study.

2.5. Measurement of Pressure Drops

A pressure transducer from Omega Engineering Inc. is mounted in the system. The range of the pressure transducer is from 0 to 2490.9 Pa and the accuracy is ±0.05% (full scale). Therefore, the absolute uncertainty of the pressure transducer is 1.25 Pa. The pressure transducer is an industrial transmitter with high accuracy and low noise, 4-20 mA output. A broad temperature range and excellent temperature compensation make the pressure transducer stable at fluctuating temperatures.

2.6. Particle Image Velocimetry Measurement and Instrumentation

A commercial, telescopic, particle image velocimetry (PIV) system captured flow characteristics in the duct. PIV is a powerful tool used in many configurations [18], [19], [75]–[78]. However, it is rarely used to collect flow characteristics near heat transfer fins. Dupuis et al. [49] identified and analyzed flow structures in pyramidal-pin fin arrays for laminar flow. Their fins were sprayed on aluminum substrates with dimensions of 7 mm × 51 mm. Fin height was 1.0 mm, and fin base length was 1.5 mm. In their study, PIV measured not only instantaneous velocity fields but also other related properties such as turbulent intensity. The flow in their study was pure nitrogen. Flow structures obtained in the micro-channel affected flow stability, structure and turbulence level, which contributed to the increase of the convective heat transfer coefficient. In 2017, Xia et al. [50] presented experimental results of the laminar-flow behavior of water in circular micro pin-fin, square micro pin-fin and diamond micro pin-fin heat sinks with PIV. The entire dimension with the micro-pin fin arrays was 10 mm (length) × 2.2 mm (width) × 0.1 mm (height). Vortexes in their study explained why the best heat transfer enhancement behaviors were

in the diamond micro pin-fin heat sink. With an increasing Reynolds number, vortexes in the diamond micro pin-fin occurred the earliest and had the most complicated structure, which effectively improved the mixing of fluid and heat transfer. In the above examples, PIV was applied to micro-channels. For the current study, PIV was used in a larger passage with smaller micro-fins (micro-fin height/duct height$\approx$0.022).

Fig. 2.3 shows the PIV set-up in this experiment. Water flows from the left side to the right side. In this study, 3.2 μm diameter fluorescent particles were used for the PIV measurements. Particle density was about 0.004 particle/pixel. The pixel size of the camera used in this experiment was 7.4 pixel/μm. The dimension of the camera's view was 2048 pixel × 2048 pixel (3 mm × 3 mm). The view of the camera was in the X-Y plane. The camera was moved in the Z direction and was mounted on a translating stage with an inch micrometer traverse. The precision of the micrometer was 0.001 inches. The movement of the camera was corrected to reflect the true movement of the focal plane due to the difference in optical path length caused by the air/water interface. Therefore, the true movement is equal to micrometer movement multiplied by the refractive index of water, 1.33. This correction is necessary for volume-illuminated PIV as referenced by Meinhart et al. [78], [79]. A 532 nm band-stop filter was placed over the optics to filter out laser reflections and only capture the particle fluorescence. The width and height of the PIV interrogation region were 128 pixels with 0.5 overlap. A microscope system, 610088w cf-4, used in this experiment had a magnification of 5. The pulse repetition rate for the laser was 7.25 Hz and the pulse separation was 25 μs.

INSIGHT 4G was used for global image capture, analysis, and display purposes [80]. It implemented the PIV processing algorithm in the following four plugin engines: (1) grid engines, (2) spot mask engines, (3) correlation engines, and (4) peak engines. Nyquist grid, Gaussian mask,

fast Fourier transform correlation, and Gaussian peak, respectively, were applied to data processing.

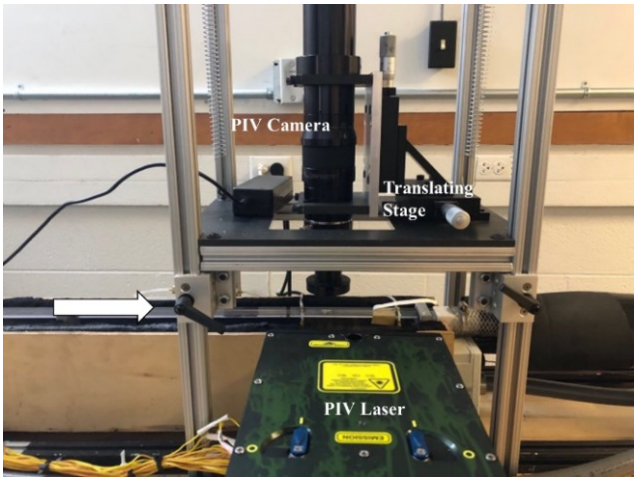

Figure 2.3: Experimental setup and PIV instrumentations

2.7. Uncertainty Methodology for PIV

The Visualization Society of Japan (VSJ) proposed a method for uncertainty analysis on PIV measurement [81]. The method infers the velocity of a flow field through the following equation:

$$UN_{piv} = \alpha\left(\frac{\Delta x}{\Delta t}\right) + \delta u \tag{2.7}$$

where Δx is the displacement of a local region of the flow, Δt is the time elapsed between a pair of images, δu represents the variation between the particle velocity and the actual flow velocity, and α represents the camera model which for 2D-PIV is simply a magnification factor. Thus, there are four areas as follows in which uncertainty is added to the measurement [81]: (1) Camera model uncertainties; (2) Pixel displacement uncertainties; (3) Time interval uncertainties; (4) Particle/fluid interaction uncertainties. As an example, the summary of PIV uncertainties for highest velocity (u=0.62 m/s, Z=7.6 mm) for Case 1 in Chapter 4 is shown in Table 2.2, and the combined uncertainty calculated by using the root-sum-square of the product of standard

uncertainty and sensitivity coefficient, c_i, was ±128 mm/s (≈ ±0.13 m/s). The relative error for the velocity is approximately 10%. The largest uncertainty for the PIV system is from laser power fluctuation. The maximum uncertainty from laser power fluctuation can be in the length of particle diameter [81]. The second largest uncertainty source is the mis-matching error between particle image pairs. Therefore, the pixel displacement uncertainties dominate the combined uncertainty. According to Table 2.2, velocity affects the combined uncertainty slightly, hence the combined uncertainty for other velocities in Case 1 and Case 2 is also ±0.13 m/s. The largest relative error is approximately 30% at the smallest measured velocity of 0.435 m/s. The larger the velocity is, the smaller the relative error. The error bars presented with the PIV data represent the constant combined uncertainty of ±0.13 m/s.

Table 2.2: Summary of Uncertainties on PIV Measurement

Parameter	Category	Error Sources	$un(x_i)$	Unit	C_i	Unit	$C_iu(x_i)$	u_c
α	Calibration	Reference Image	0.7	Pixel	7.153E-07	mm/pixel^2	5.007E-07	
		Physical Distance	0.3	mm	4.883E-04	1/pixel	1.465E-04	
		Image Distortion by Lens	10.24	Pixel	7.153E-07	mm/pixel^2	7.325E-06	
		Image Distortion by CCD	0.006	Pixel	7.153E-07	mm/pixel^2	4.006E-09	
		Reference Board Position	0.040	mm	2.764E-05	1/pixel	1.106E-06	
		Parallel Board	0.035	rad	2.301E-03	mm/pixel	8.053E-05	1.673E-04
ΔX	Acquisition	Laser Power Fluctuation	3.200E-03	mm	6.827E+02	pixel/mm	2.185E+00	
		Image Distortion by CCD	3.000E-03	pixel	1		3.000E-03	
	Reduction	Mis-matching Error	0.2	pixel	1		0.2	
		Sub-pixel Analysis	0.03	pixel	1		0.03	2.194
Δt	Acquisition	Delay Generator	2.00E-09	s	1		2.000E-09	
		Pulse Timing Accuracy	5.00E-09	s	1		5.000E-09	5.385E-09
δu	Experiment	Particle Trajectory	0.103	mm/s	1		0.103	0.103

Parameter	Error Sources	$un(x_i)$	Unit	C_i	Unit	$C_iu(x_i)$
α	Magnification Factor	1.673E-04	mm/pixel	6.827E+02	pixel/s	0.114
ΔX	Image Displacement	2.194E+00	pixel	5.859E+01	mm/pixel/s	1.285E+02
Δt	Image Interval	5.385E-09	s	4.000E+04	mm/s^2	2.154E-04
δu	Experiment	0.103	mm/s	1		0.103
			Combined Uncertainty		mm/s	128.548

2.8. Conclusions

The chapter introduces the experimental set-ups in the study. Chapters 2.1 and 2.2 introduces the water loop and the test section, respectively. The measurements of *HTC* are mainly shown in chapters 2.3 and 2.4. Chapter 2.5 presents the measurements of pressure drops. Chapters 2.6 and 2.7 introduces the measurement and the uncertainty analysis of PIV.

Chapter 3 - Governing Equations for Numerical Simulations

3.1. Flow Model

Computational fluid dynamics (CFD) is applied to in a wide range of fields [19], [75], [82]–[88]. In this study, Navier-Stokes equations were used to simulate the fluid transport process. The equation for conservation of mass, or continuity equation, is written as follows [55], [89]:

$$\frac{\partial \rho}{\partial t} + \nabla \cdot (\rho \vec{u}) = 0 \tag{3.1}$$

In this equation, ρ is fluid density and u is fluid velocity vector.

Conservation of momentum in an inertial reference frame is described by [55], [90]:

$$\frac{\partial}{\partial t}(\rho \vec{u}) + \nabla \cdot (\rho \vec{u} \otimes \vec{u}) = -\nabla p + \nabla \cdot (\bar{\bar{\tau}}) + \rho \vec{g} + \vec{F} \tag{3.2}$$

Where p is the static pressure, $\bar{\bar{\tau}}$ is the stress tensor, and $\rho \vec{g}$ and $\vec{F}$ are the gravitational body force and external body forces, respectively.

3.2. Viscous Models

Reynolds Stress Model (RSM) and Large Eddy Simulation (LES) were used in the simulations.

RSM closes the Reynolds-averaged Navier-Stokes equations by solving transport equations for the Reynolds stresses, together with an equation for the dissipation rate. This means that seven additional transport equations must be solved for three dimensions. Quadratic Pressure-Strain model proposed by Speziale et al. [91] was selected in Reynolds-Stress Model. This model has been demonstrated to give superior performance in a range of basic shear flows, including plane strain. Scalable wall functions were used as near-wall treatment. The near-wall values of the Reynolds stresses and turbulence dissipation rate were computed from wall functions.

LES is another popular technique for simulating turbulent flows, which allows one to explicitly solve for the large eddies in a calculation and implicitly account for the small eddies by using a sub-grid scale model (SGS model). Mathematically, one may think of separating the velocity field into a resolved and sub-grid part. Formally, one may think of filtering as the convolution of a function with [55], [89]:

$$\bar{u}_i(\vec{x}) = \int G(\vec{x} - \vec{\xi}) u(\vec{\xi})\, d\vec{\xi} \tag{3.3}$$

resulting in

$$u_i = \bar{u}_i + u_i' \tag{3.4}$$

where $\bar{u}_i$ is the resolvable scale part and u_i' is the sub-grid scale part. The research is mainly focused on LES of incompressible flows. The filter equations are developed from the incompressible Navier-Stokes equations of motion:

$$\frac{\partial u_i}{\partial t} + u_j \frac{\partial u_i}{\partial x_j} = -\frac{1}{\rho}\frac{\partial p}{\partial x_i} + \frac{\partial}{\partial x_j}\left(\mu \frac{\partial u_i}{\partial x_j}\right) \tag{3.5}$$

Substituting in the decomposition $u_i = \bar{u}_i + u_i'$ and $p = \bar{p} + p'$ and then filtering the resulting equation gives the equations of motion for the resolved field:

$$\frac{\partial \bar{u}_i}{\partial t} + \bar{u}_j \frac{\partial \bar{u}_i}{\partial x_j} = -\frac{1}{\rho}\frac{\partial \bar{p}}{\partial x_i} + \frac{\partial}{\partial x_j}\left(\mu \frac{\partial \bar{u}_i}{\partial x_j}\right) + \frac{1}{\rho}\frac{\partial \tau_{ij}}{\partial x_j} \tag{3.6}$$

The $\frac{\partial \tau_{ij}}{\partial x_j}$ extra term in Eq. (13) arises from the non-linear advection terms, due to the fact that

$$\overline{u_j \frac{\partial u_i}{\partial x_j}} \neq \bar{u}_j \frac{\partial \bar{u}_i}{\partial x_j} \tag{3.7}$$

The extra term mentioned above must be modeled for the sub-grid scales. A simple model was first proposed by Smagorinsky [89]. In the Smagorinsky-Lilly model (Lilly Model), the eddy-viscosity is modeled by

$$\mu_t = \rho L_s^2 |\bar{S}| \tag{3.8}$$

where L_s is the mixing length for sub-grid scales and $|\bar{S}| \equiv \sqrt{2\bar{S}_{ij}\bar{S}_{ij}}$. S is the rate-of-strain tensor for the resolved scale. L_s is computed by using

$$L_s = \min(k_s d_w, C_{smag}\Delta) \tag{3.9}$$

where k_s is the von Kármán constant, d_w is the wall distance, C_{smag} is the Smagorinsky constant, and Δ is the local grid scale. Germano et al. [92] conceived a procedure in which the Smagorinsky model constant, C_{smag}, is dynamically computed based on the information provided by the resolved scales of motion. The dynamic procedure therefore obviates the need for users to specify the model constant C_{smag} in advance [55].

In the Wall-Modeled LES model (WMLES), the eddy viscosity is calculated with the use of a hybrid length scale [93]:

$$\mu_t = \min\left[(k_s d_w)^2, \left(C_{Smag}\Delta\right)^2\right] \cdot S \cdot \{1 - \exp[-(y^+/25)^3]\} \tag{3.10}$$

where d_w is the wall distance, S is the rate-of-strain tensor, $k_s = 0.41$ and $C_{Smag} = 0.2$ are constants, and y^+ is the normal to the wall inner scaling.

The subgrid-scale stress,$\tau_{SGS_{ij}}$, is modeled by

$$\tau_{SGS_{ij}} = \overline{u_\iota u_J} - \bar{u}_i \bar{u}_j \tag{3.11}$$

The subgrid-scale kinetic energy for LDKM is defined as [92]

$$k_{SGS} = \frac{1}{2}(\overline{u_k^2} - \bar{u}_k^2) \tag{3.12}$$

The subgrid-scale stress can then be written as

$$\tau_{SGS_{ij}} = -2C_k k_{SGS}^{1/2}\bar{\Delta}\bar{S}_{ij} + \frac{2}{3}k_{SGS}\delta_{ij} \tag{3.13}$$

where $\bar{\Delta}$ is grid width. $\bar{S}_{ij}$ is the resolved-scale strain-rate tensor, which is defined as

$$\bar{S}_{ij} = \frac{1}{2}\left(\frac{\partial \bar{u}_i}{\partial x_j} + \frac{\partial \bar{u}_j}{\partial x_i}\right) \tag{3.14}$$

This derived the transport equation for LDKM as [94]

$$\frac{\partial k_{SGS}}{\partial t} + \bar{u}_i \frac{\partial k_{SGS}}{\partial x_i} = -\tau_{SGS_{ij}} \frac{\partial \bar{u}_i}{\partial x_j} - C_\varepsilon \frac{k_{SGS}^{3/2}}{\bar{\Delta}} + \frac{\partial}{\partial x_i}(\mu_t \frac{\partial k_{SGS}}{\partial x_i}) \tag{3.15}$$

In the above equations, model constants, C_k and C_ε, were determined dynamically. For LDKM, the subgrid-scale eddy viscosity, μ_t, was modeled by [55], [94]

$$\mu_t = C_k \bar{\Delta} k_{SGS}^{1/2} \tag{3.16}$$

Some LES with other SGS models, such as the Smagorinsky-Lilly Model (Lilly model) and Algebraic Wall-Modeled LES Model (WMLES model), etc., were also tried in the study. It was found these LES models failed to validate against the experimental data.

3.3. Energy Equations

ANSYS Fluent solves the energy equation in the following form [55]:

$$\frac{\partial}{\partial t}(\rho E) + \nabla \cdot \left(\vec{v}(\rho E + p)\right) = \nabla \cdot \left(k_{eff} \nabla T - \sum_j h_j \overrightarrow{J_j} + \left(\overline{\overline{\tau_{eff}}} \cdot \vec{v}\right)\right) + S_h \tag{3.17}$$

Where k_{eff} is the effective conductivity, and $\overrightarrow{J_j}$ is the diffusion flux. The first three terms on the right-hand side of Eq. 3.17 represent energy transfer due to conduction, species diffusion, and viscous dissipation, respectively. S_h includes the heat of chemical reaction, and any other volumetric heat sources you have defined.

The energy equation for LES is solved in the following form [54], [55]:

$$\frac{\partial \bar{T}}{\partial t} + \nabla \cdot (\bar{u}\bar{T}) = \nabla \cdot (\beta \nabla \bar{T}) - \frac{\nabla \cdot q''_{SGS}}{\rho e} \tag{3.18}$$

$\bar{T}$ is filtered temperature for LES. β and e are thermal diffusivity and heat capacity, respectively. q''_{SGS} is subgrid-scale heat flux.

3.4. Conclusions

The chapter introduces the governing equations in the numerical simulations. Chapter 3.1 presents the Navier-Stokes equations. Chapter 3.2 introduces all viscous models we used in the study. Chapter 3.3 presents the energy equations.

Chapter 4 - Incorporating Particle Image Velocimetry (PIV) Data into Boundary Conditions of Large Eddy Simulations (LES)

4.1. Overview for LES Boundary Conditions

Inlet boundary conditions affect the accuracy of large eddy simulations (LES) significantly, and the treatment of inlet conditions for LES is a complicated problem. Theoretically, a good boundary condition for LES should contain the following features: (1) providing accurate information of flow characteristics, i.e. velocity and turbulence; (2) satisfying the Navier-Stokes equations and other physics; (3) being easy to implement and adjust to different cases. Currently, methods of generating inlet conditions for LES are broadly divided into two categories as classified by Tabor et al. [95]. The first method [96]–[100] for generating turbulent inlets is to synthesize them according to particular cases, such as Fourier techniques, principle orthogonal decomposition (POD) and vortex methods. The synthesis techniques attempt to construct turbulent fields at inlets that have suitable turbulence-like properties and make it easy to specify parameters of the turbulence, such as turbulent kinetic energy and turbulent dissipation rate. In addition, inlet conditions generated by using random numbers are computationally inexpensive. However, one serious drawback exists in the method. The synthesized turbulence does not satisfy the physical structure of fluid flow governed by Navier-Stokes equations. The second method [84], [85], [101]–[105] involves a separate and precursor calculation to generate a turbulent database which can be introduced into the main computation at the inlets. The database (sometimes named as 'library') can be generated in a number of ways, such as cyclic domains, pre-prepared library and internal mapping. However, the method of generating turbulent inflow by precursor simulations requires large calculation capacity. Researchers examining the application of various types of synthetic and precursor calculations have found that the more realistic the inlet turbulence, the more accurate

LES predicts results [95]. The current research proposes a method to directly use experimental data to obtain inlet boundary conditions for LES.

The numerical simulations in the chapter were conducted in commercial software, ANSYS Fluent 15.0.0, which contains the broad physical modeling capabilities needed to model flow and turbulence. Fluent offers different parallel processing options [106] to increase the calculation speeds and provides a user-defined function (UDF) which can be used to customize boundary conditions. Fluent provides vortex methods for generating LES inlet conditions. Furthermore, the Reynolds-Stress Model (RSM) is available. The results simulated by the new inlet generation method are compared with other numerical results and PIV results for validation and discussion. Two frequently-used LES turbulent models were selected in the current study, namely Dynamic Smagorinsky-Lilly Model (Lilly model) [92] and Wall Modeled Large Eddy Simulation (WMLES model) [93]. Two broad cases of flow in a duct (Case 1: average velocity at inlet ≈ 0.5 m/s, Reynolds number ≈ 9000, transition flow; Case 2: average velocity at inlet ≈ 0.9 m/s, Reynolds number ≈ 14000, fully turbulent flow) are investigated in the present study.

From the PIV data, two kinds of inlet boundary conditions are generated for the numerical simulations, i.e. the previously used steady spatial distributed inlet (SSDI) and the proposed method denoted unsteady spatial distributed inlet (USDI). For SSDI, time-averaged values of velocity magnitude, turbulent kinetic energy and turbulent dissipation rate are mapped to grid structures as the inflow boundary conditions. SSDI then uses the vortex method to synthesize turbulent inlets for LES. For USDI, PIV time series data, i.e. velocity magnitude, are directly mapped to grid structures at inlets. Therefore, the turbulence in the duct is generated by the fluctuation of the time series of PIV data. The USDI has similarities to precursor simulation methods, but it directly applies experimental data to the boundary conditions of LES. The influence

of these methods on flow predictions such as velocity profiles, turbulent structures, system pressures, and pressure drops are discussed in the chapter.

The study explores a method of generating boundary conditions for LES by experimental data. The experimental data set generated with PIV at the inlet and in the fully developed region provide the unique opportunity to compare simulation techniques and make recommendations for generating boundary conditions in LES for wall-bounded flows.

4.2. Inferring Flow Characteristics from PIV Data

One method of specifying the nature of the turbulence in a flow is through velocity magnitude, turbulent kinetic energy and turbulent dissipation rate as is common in RSM and LES. Thus, these parameters need to be estimated by the series of velocity fields captured by the PIV system.

The direction of inlet velocity is normal to the boundary, so velocity magnitude at the inlet is directly calculated by the y velocity component as follows:

$$V = \sqrt{(u_y^2)} \tag{4.1}$$

The velocity magnitude at the downstream is calculated by the three velocity components, u_x, u_y and u_z. For 2D-PIV, the third velocity component u_z cannot be measured, so we assume velocity components and turbulent fluctuations in Z direction are same with those in X direction.

The turbulent kinetic energy, k, is the kinetic energy per unit mass of the turbulent fluctuations u_i' in a turbulent flow. The unit of k is J/kg=m^2/s^2. The equation of k is:

$$k = \frac{1}{2}(\overline{u_x'^2} + \overline{u_y'^2} + \overline{u_z'^2}) \tag{4.2}$$

where the overbar indicates a time average. The time average must be done long enough for these variables to become stationary. For the work in this chapter, these averages were calculated from a set of 2700 PIV samples.

The local dissipation rate is calculated by the second order velocity structure function [107], [108] as follow:

$$D_{ij}(\vec{e},t) \equiv \overline{\left(u_x(\vec{R}+\vec{e},t)-u_x(\vec{R},t)\right)\left(u_y\left(\vec{R}+\vec{e},t\right)-u_y\left(\vec{R},t\right)\right)} \tag{4.3}$$

D_{ij} can be computed using PIV data measured at points $\vec{R}$ and $\vec{R}+\vec{e}$. $\vec{e}$ represents a displacement vector. Assuming isotropic turbulence, in inertial subrange, the longitudinal structure function is related to turbulent dissipation rate:

$$D_{LL}(e) \equiv D_{11}(e) = C_2(\varepsilon e)^{2/3} \tag{4.4}$$

where C_2 is a universal constant (C_2=2.12, as suggested by Sreenivasan [109]). This leads to the estimate of ε:

$$\varepsilon = \frac{1}{e}\left(\frac{D_{LL}(e)}{C_2}\right)^{3/2} \tag{4.5}$$

Using these equations, turbulent kinetic energy and turbulent dissipation rate are found from 2700 independent PIV velocities from each measurement location. The details of PIV measurement are in Chapter 2.6.

Taylor microscale, λ, is calculated by turbulent kinetic energy and turbulent dissipation rate as follow [107]:

$$\lambda \approx \sqrt{10\nu\frac{k}{\varepsilon}} \tag{4.6}$$

where ν is the kinematic viscosity. The Taylor microscale for the cases is between 0.8 mm to 2.5 mm.

4.3. Autocorrelation for PIV Data

Assumptions about the independence of the PIV velocity samples affect how data is used in computations. If the samples are time-independent, the averaged quantities from the PIV data will yield statistically stationary values. Autocorrelation of a time series refers to the correlation

between its own past and future values, which is sometimes called lagged correlation or serial correlation [110]. The range of correlation coefficient is from -1 to 1. That correlation coefficient is close to 1 means that the time series is statistically dependent. If the correlation coefficient is close to 0, the time series is statistically independent. The first-order autocorrelation coefficient is the simple correlation coefficient of the first $N-1$ observations,a_n, $n = 1, 2, \cdots, N-1$ and the next $N-1$ observations, $a_n, n = 2, 3, \cdots, N$. The correlation between a_n and a_{n+1} is given by [110]

$$r = \frac{\sum_{n=1}^{N-1}(a_n - \bar{a}_{(1)})(a_{n+1} - \bar{a}_{(2)})}{[\sum_{n=1}^{N-1}(a_n - \bar{a}_{(1)})^2]^{1/2}[\sum_{n=2}^{N}(a_n - \bar{a}_{(2)})^2]^{1/2}} \tag{4.7}$$

Where $\bar{a}_{(1)}$ is the mean of the first $N-1$ observations and $\bar{a}_{(2)}$ is the mean of the last $N-1$ observations.

For the raw PIV data, the absolute value of the autocorrelation coefficient is approximately from 0.001 to 0.1 (very close to 0), which indicates the PIV data is nearly statistically independent and suitable for calculating average turbulent statistics. Careful consideration of this characteristic is needed when using PIV as part of LES simulations as will be seen later in the chapter.

4.4. Geometry

To reduce computational time, the simulation was conducted in a half duct with symmetrical boundary conditions as shown in Fig. 4.1. The height of the geometry is 15.2 mm and the width is 7.6 mm. The total length of the duct is 609.6 mm. Line 1 in Fig. 4.1 (a) is the location where numerical results and experimental results are compared. Line 1 is on the symmetrical boundary, and its distance from the exit is 150 mm. The rectangular box highlights the area where inlet PIV measurements were taken. Figures 4.1 (b) and (c) are the zoom-in view of the inlet. The geometry with uniform meshes in Fig. 4.1 (b) was applied to the cases simulated by RSM. Figure

4.1 (c) shows the geometry with refined meshes for LES. Point 1 in Fig. 4.1 (b) and (c) is located at the center of the inlet.

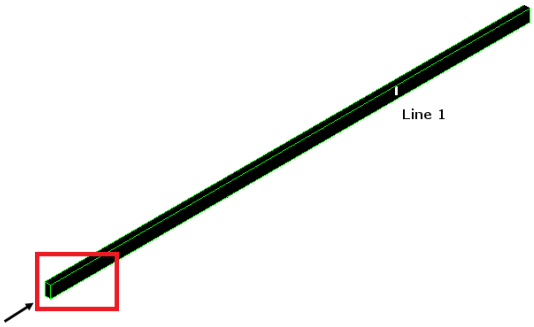

(a)

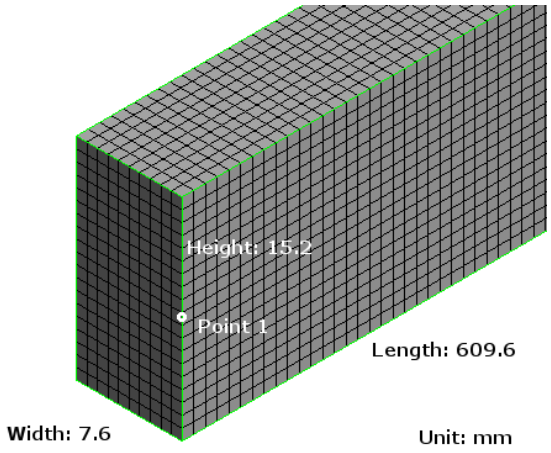

(b)

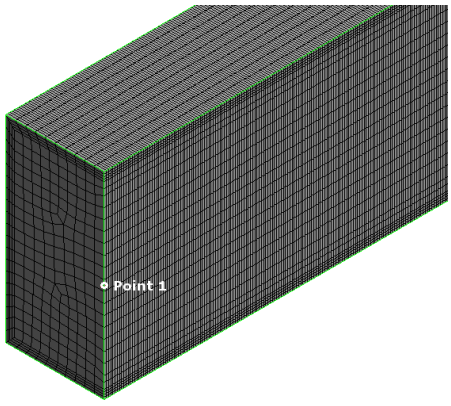

(c)

Figure 4.1: Geometry with Meshes: (a) Whole Domain, (b) Zoom-in View at Inlet for RSM, (c) Zoom-in View at Inlet for LES

4.5. Boundary Conditions for Steady Inlets (SSDI)

Velocities at the inlet were measured by PIV in one quadrant (upper left) at the inlet of the duct. The time-averaged values of velocity and turbulence were calculated from PIV data and then assigned to each grid as shown in Fig. 4.2. Each grid in Fig. 4.2 occupies a certain domain. The coordinate range of each domain is known. Time-averaged values are assigned to the domain of each grid with UDF, which generates the steady spatial distributed inlet (SSDI). In Fig. 4.2, the velocity magnitudes around the center of the inlet are relatively high. The turbulence around the center is very low. However, turbulence close to the walls of the duct is high. For the geometries with refined meshes for LES, the SSDI for LES is generated in the same manner.

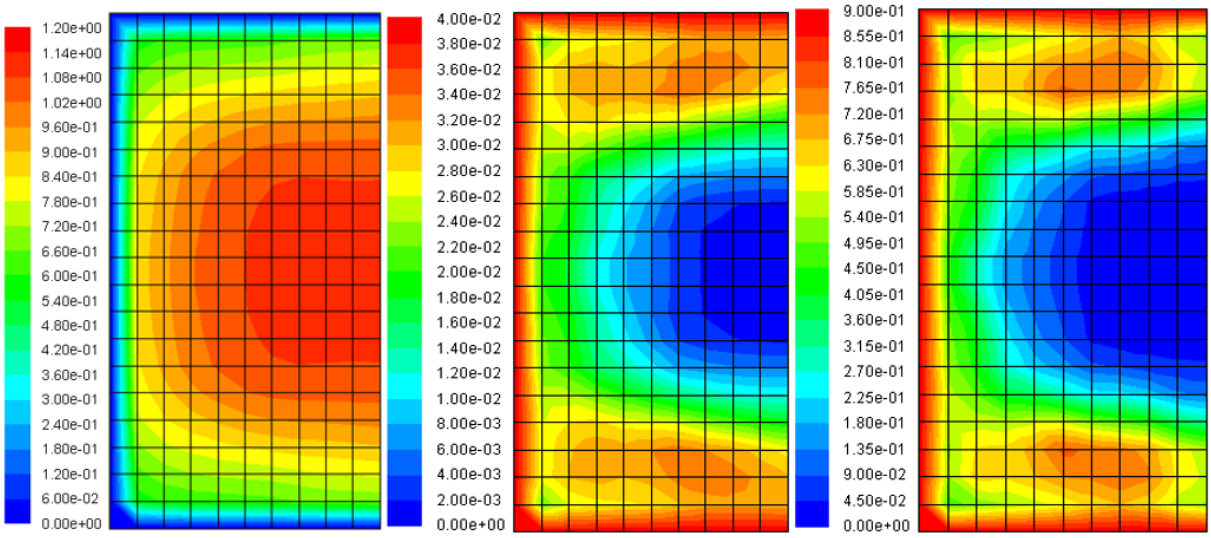

(a) (b) (c)

Figure 4.2: Boundary Conditions for Case 2 with PIV Measurement Data: (a) Velocity Magnitude (m/s), (b) Turbulent Kinetic Energy (m^2/s^2), (c) Turbulent Dissipation Rate (m^2/s^3)

4.6. Boundary Conditions for Unsteady Inlets (USDI)

In this case, the inlet surface is divided into several square domains. PIV time series data (velocity) within the domains are measured and recorded. Then the data are directly mapped to each domain with UDF at every simulation time step. According to the assignment, each grid obtains a velocity at each time step, which generates the unsteady spatial distributed inlet (USDI). Therefore, the turbulence in the duct is generated by the fluctuation of the velocities. The frequency of PIV data collection is 7.25 Hz, but the time step size in the numerical simulations is much smaller (dt=0.0005 s). Linear fitting was used to interpolate 275 data between each two PIV data to expand the time series of the PIV data to generate a database for the boundary conditions.

4.7. Grid-independence Study

A grid-size independence study was performed to determine the resolution of the simulations. Structured grids with hexahedral cells with equal length edges (shown in Fig. 4.1) are used in the numerical simulations. Four grid size levels were chosen: finer, normal, coarser and coarsest. The grid size of each level was 3.38 mm, 1.69 mm, 0.845 mm, and 0.4225 mm, respectively. Figure 4.1 (a) shows the exact position of line 1 (located in the fully developed region) where the velocity profiles for grid-independence study are located. Figure 4.3 is the comparison of average velocity magnitudes on line 1 in Z direction for Case 1 with RSM. Y-axis represents the distance from the location of velocity magnitude to the top surface of the duct. The time step for RSM was 0.001 s. In Fig. 4.3, the results of the normal grid and finer grid are much closer to each other than the coarser grid results and the coarsest grid results. There are little noticeable differences (the maximum relative error around Z=1.7 mm is smaller than 5%.) between the finer- and normal-grid results, which indicates the grid convergence has been reached for RSM. The 0.845 mm grid is sufficient for RSM with SSDI.

The grid size for LES should be close to Taylor microscale [107]. Therefore, the coarse grid size in Fig. 4.1 (c) falls within the computed Taylor microscale range. The refined grid size in Fig. 4.1 (c) is 0.169 mm. The smaller the refined grid size, the more elements are generated. Further refinement of the mesh was not judged to be worth the additional computational effort. y^+, the dimensionless wall distance, depends on the grid sizes close to walls. y^+ at the walls is approximately equal to 3. The ratio of kinematic viscosity to friction velocity, y^*, is approximately equal to 4.1×10^{-2} mm. The time step for LES was 0.0005 s to satisfy $dt \leq \frac{\Delta}{V}$ [111]. The total simulation time was 41 s for RSM and LES.

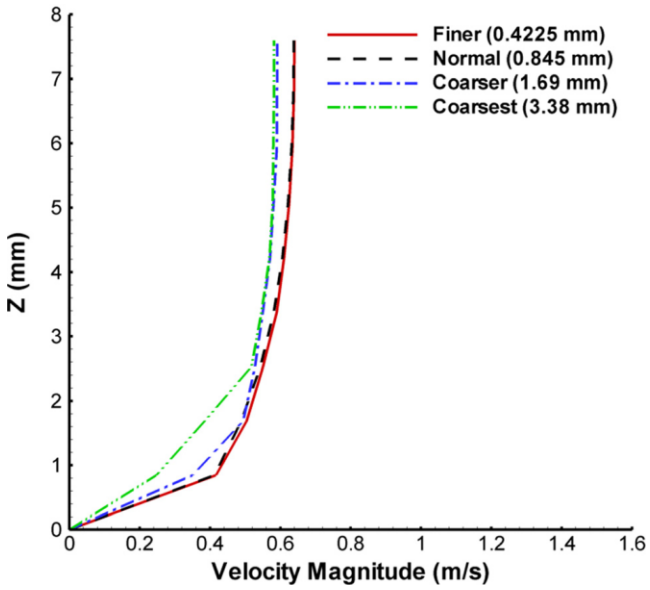

Figure 4.3: Grid-independence Study for RSM with SSDI

4.8. Numerical Results for Reynolds Stress Model

Figure 4.4 (a) and (c) display velocity profiles on line 1 for the two cases. The velocity profiles measured by PIV agree with those simulated by RSM with SSDI very well. Figure 4.4 (b) and (d) show the distributions of turbulent kinetic energy on line 1. The distributions of kinetic energy in the experiment match those simulated by RSM, which indicates the experimental results

and the numerical results are reasonable. LES results are compared with the PIV results and RSM results in the section for discussion and validation.

Figures 4.5 (a), (b) and (c) show the contours of velocity magnitude, turbulent kinetic energy and turbulent dissipation rate in the cross sections for Case 2 after the RSM results are converged. The distance from cross-section to the exit surface (from left to right) is 450 mm, 250 mm and 50 mm, respectively. According to Fig. 4.5 (a), the velocity magnitude at the center of the duct increases with the flow direction. In Figs. 4.5 (b) and (c), high turbulence is always close to the walls.

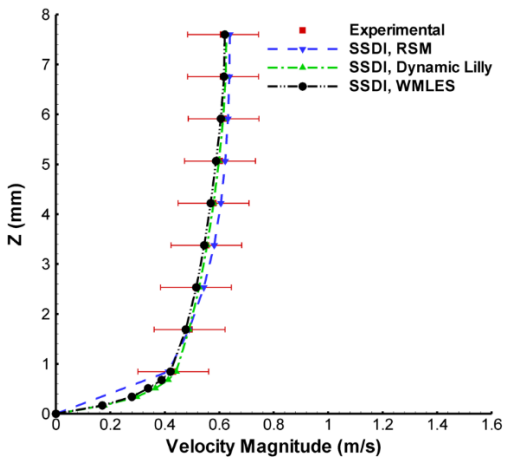

(a)

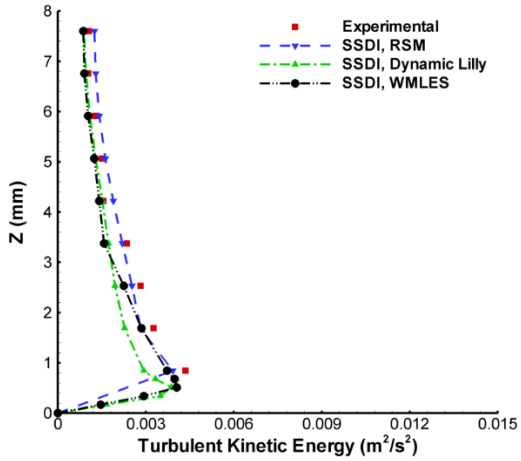

(b)

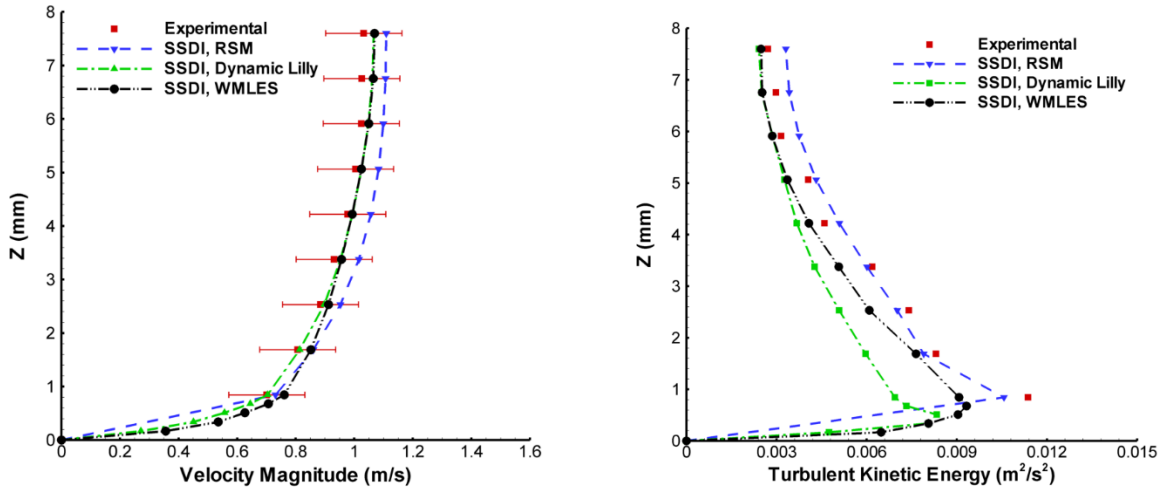

(c) (d)

Figure 4.4: Experimental Results and Numerical Results with SSDI on Line 1: (a) Velocity Profiles for Case 1, (b) Turbulent Kinetic Energy for Case 1, (c) Velocity Profiles for Case 2, (d) Turbulent Kinetic Energy for Case 2

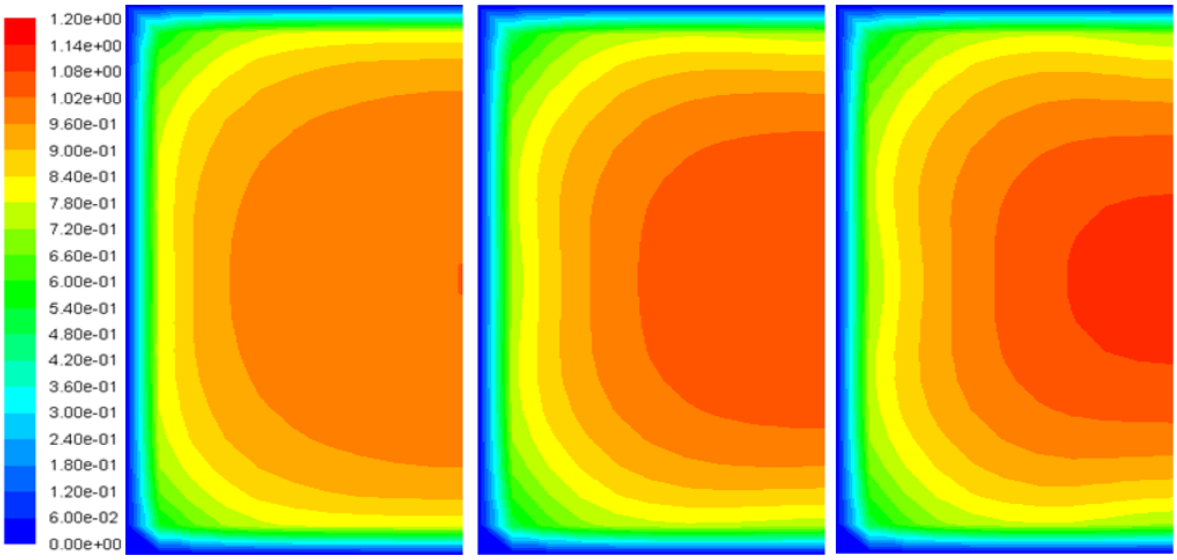

(a)

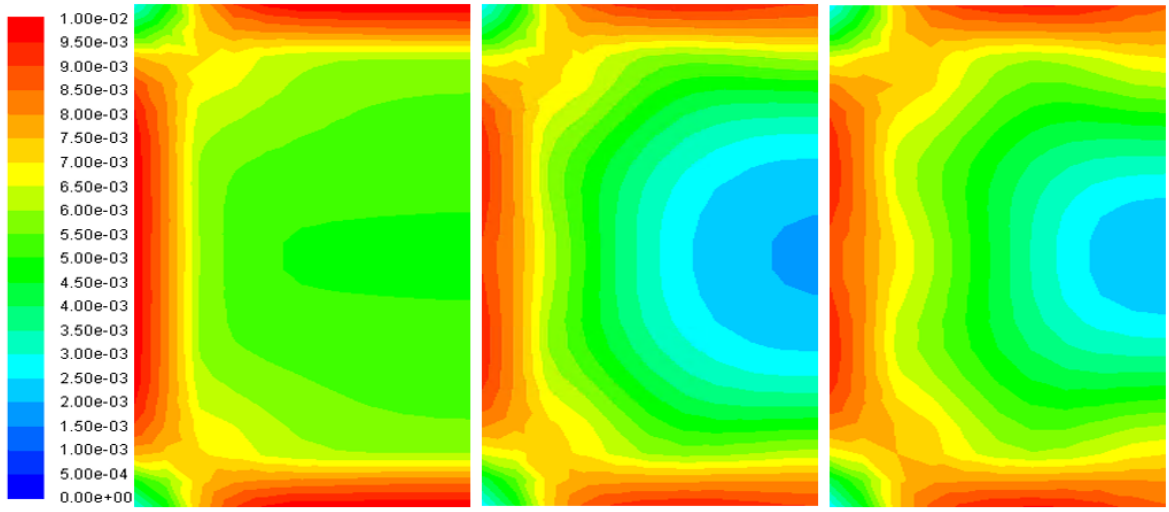

(b)

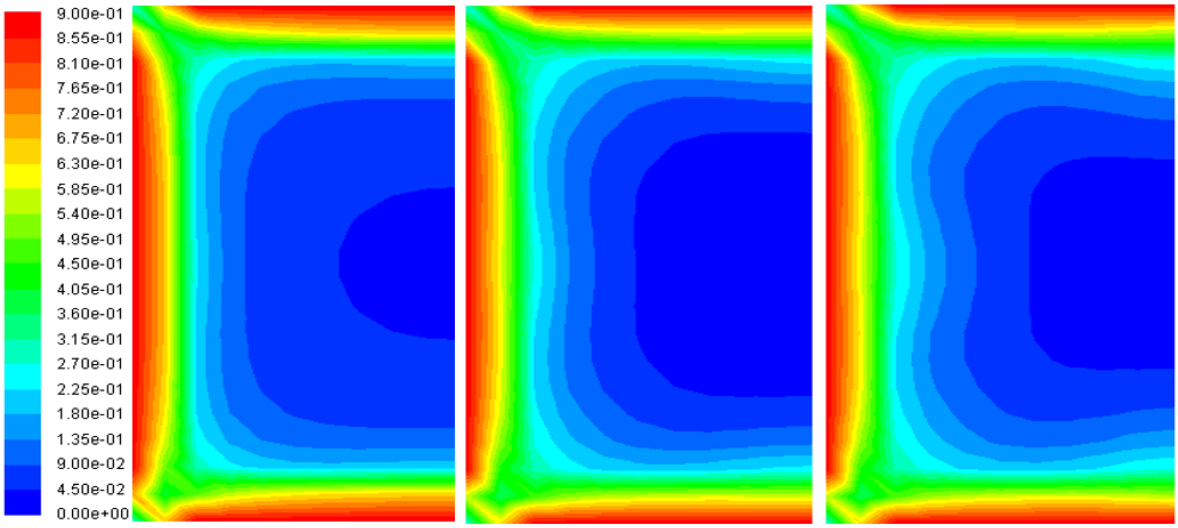

(c)

Figure 4.5: Contours for the RSM Results in Cross Sections: (a) Velocity Magnitude (m/s), (b) Turbulent Kinetic Energy (m^2/s^2), (c) Turbulent Dissipation Rate (m^2/s^3)

4.9. Numerical Results for LES with Steady Inlets

4.9.1. Dynamic Smagorinsky-Lilly Model (Lilly Model)

The velocity profiles simulated by Dynamic Smagorinsky-Lilly Model with SSDI are shown in Figs. 4.4 (a) and (c). It is obvious that the velocity profiles simulated by the Lilly model

with SSDI match PIV and RSM profiles very well. The distributions of turbulent kinetic energy simulated by the Lilly model with SSDI are plotted in Figs. 4.4 (b) and (d). For Case 1, the kinetic energy simulated by the Lilly model with SSDI is close to the experimental results and the RSM results, except the region from 0.5 mm to 2.0 mm. In Fig. 4.4 (d), the results simulated by Lilly model for Case 2 are still much lower than the experimental results and the RSM results within the region close to the wall.

4.9.2. Wall Modeled Large Eddy Simulation (WMLES Model)

In Figs. 4.4 (a) and (c), velocity profiles simulated by WMLES model with SSDI agree with the other three results. The profiles of kinetic energy simulated by WMLES Model with steady inlets are shown in Figs. 4.4 (b) and (d). The results of turbulent kinetic energy agree with PIV results and RSM results very well, both in Figs. 4.4 (b) and (d). Compared with Lilly Model, WMLES is a better LES for the numerical simulations in square ducts with SSDI, especially for the prediction close to the walls.

4.9.3. Static Pressure for Steady Inlets

Figure 4.6 shows time histories of static pressure simulated by WMLES model at Point 1 with SSDI. The time scale is from 5 s to 10 s. Point 1 is in the middle of the right edge of the inlet surface (on the symmetrical boundary in Fig. 4.1). In Fig. 4.6, the fluctuations of the static pressure at Point 1 are too large to be realistic. The range of the static pressure is approximately from -40000 Pa to 40000 Pa. It is unrealistic that sometimes the static pressure at the inlet is lower than that at the outlet. For the cases with SSDI, the boundary conditions are distributed constant values. This is due to the fact that the boundary of turbulence generation does not consider the constraints of the momentum equation, thus leading to large pressure variations in the flow to accommodate.

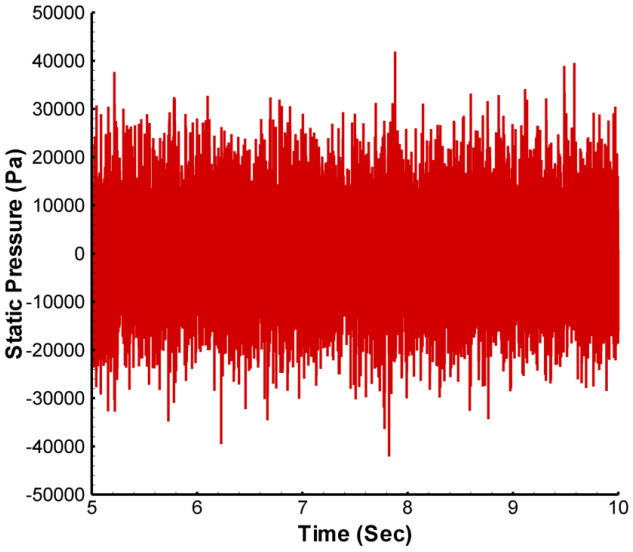

Figure 4.6: Time Histories of Static Pressure Simulated by WMLES Model with SSDI at Point 1 for Case 2

4.10. Numerical Results for LES with Unsteady Inlets

4.10.1. Dynamic Smagorinsky-Lilly Model (Lilly Model) and Wall Modeled Large Eddy Simulation (WMLES Model)

Figures 4.7 (a) and (c) show velocity with USDI. The velocity profiles simulated by Lilly model and WMLES model with USDI match the experimental results and RSM results very well. Figures 4.7 (b) and (d) illustrate the profiles of turbulent kinetic energy with USDI. Turbulent kinetic energy simulated by the Lilly model is much lower than PIV and RSM results, especially for the high-velocity case. However, WMLES model accurately predicts the results of turbulent kinetic energy with USDI, which indicates that USDI is suitable for WMLES model for the cases.

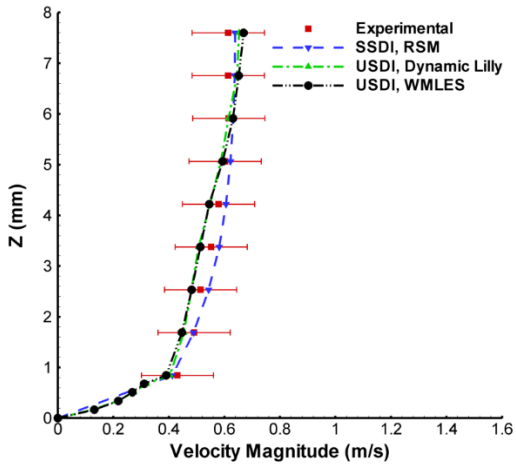

(a)

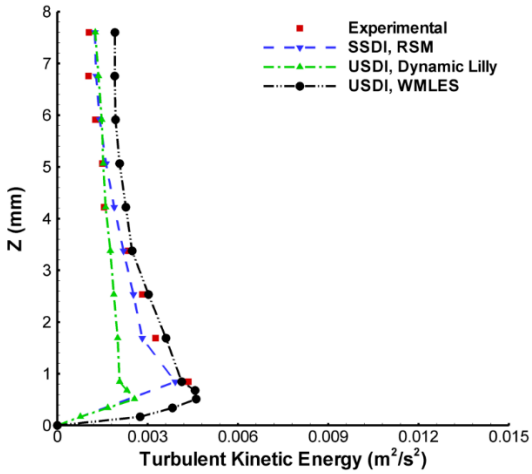

(b)

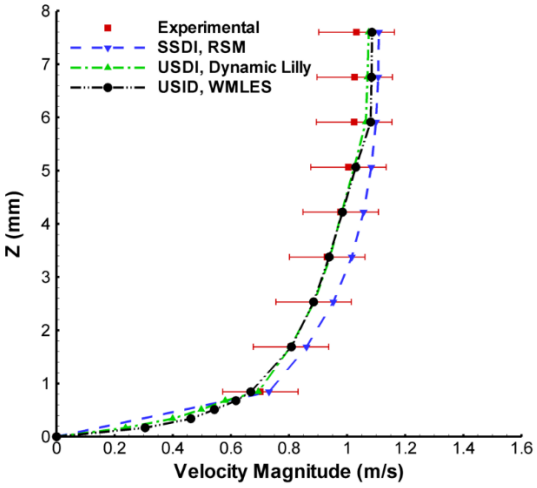

(c)

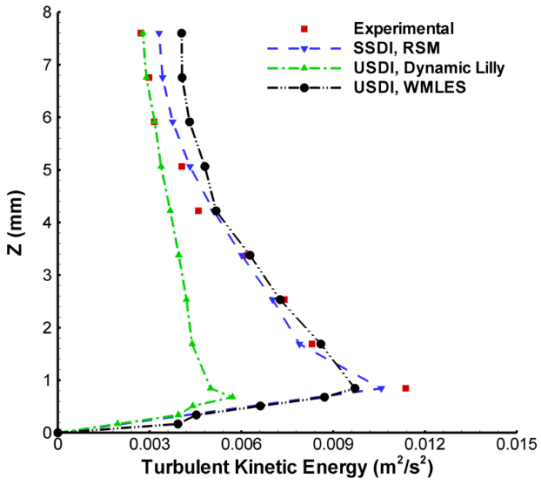

(d)

Figure 4.7: Experimental Results and Numerical Results with USDI on Line 1: (a) Velocity Profiles for Case 1, (b) Turbulent Kinetic Energy for Case 1, (c) Velocity Profiles for Case 2, (d) Turbulent Kinetic Energy for Case 2

4.10.2. Static Pressure for USDI

Figure 4.8 shows time histories of static pressure simulated by the two LES models at Point 1 with USDI for Case 2. In Fig. 4.8, the fluctuations of the static pressure are more reasonable than those with SSDI (Fig. 4.6). The oscillation range of the static pressure is approximately from 0 Pa to 700 Pa. Furthermore, the static pressure for WMLES model is a little bit higher than that for Lilly model, but the trends of the two histories are very close to each other indicating that the unsteady inlet dominates the fluctuation of the static pressure. The LES model dictates the quality of velocity profile and turbulent kinetic energy. It is important to set up appropriate boundary conditions and select appropriate turbulence models.

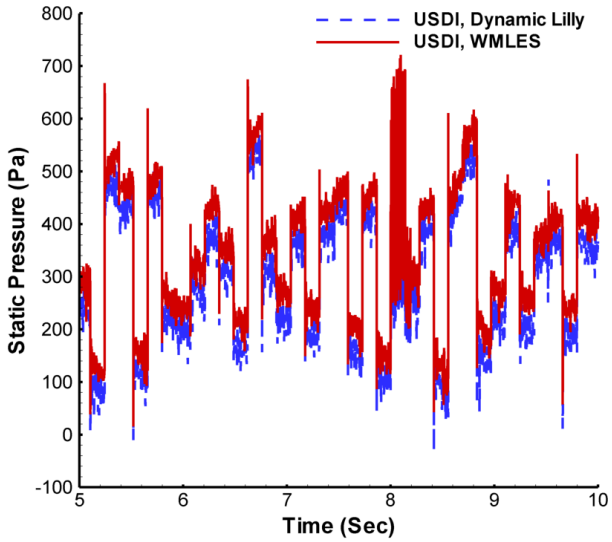

Figure 4.8: Time Histories of Static Pressure Simulated by the Two LES at Point 1 with USDI for Case 2

4.11. Pressure Drops

Table 4.1 shows pressure drops and standard deviations for the different methods for Case 2. According to Table 4.1, the pressure drops simulated by WMLES model are very close to those

in experiments and RSM. The maximum relative error is approximately 8%. However, the pressure drops predicted by Lilly model are much lower than the experimental and RSM result. The relative error is about 14%. In Table 4.1, standard deviations for USDI are much better than that for SSDI. Specifically, the SSDI provides a standard deviation two orders of magnitude higher than the experimental values while the USDI is about 30% lower than the experimental values. The authors speculate that as higher speed PIV data is utilized the standard deviation will move closer to the experimental values. But it is clear the USDI utilizing 7.25 Hz PIV inlet data provides a significantly improved method for inlet turbulence generation.

Table 4.1: Pressure Drops and Standard Deviations for Different Methods

Methods	Experimental	RSM, SSDI	Lilly, SSDI	WMLES, SSDI	Lilly, USDI	WMLES, USDI
Pressure Drop (Pa)	439.8	425.3	385.7	441.2	378.3	401.8
Standard Deviation (Pa)	185.2	N/A	10328.9	10308.1	128.5	126.2

4.12. Conclusions for the Method

A method for generating inflow boundary conditions in a square duct by using PIV measurement results is developed in the chapter. The study shows that: (1) For certain models, LES is highly sensitive to boundary conditions, which indicates a good simulation with LES requires unsteady inlets. (2) WMLES is suitable for the numerical simulations in square ducts. (3) USDI makes the fluctuation of static pressure in LES weaker to conform physics. USDI is highly recommended when the prediction of static pressure plays a critical role. (4) The new method of generating boundary conditions (USDI) for LES satisfies the three features in the introduction.

Chapter 5 - Effect of Parallel Processing on Large Eddy Simulations in ANSYS Fluent

5.1. Introduction for Parallel Processing on LES

There are two fundamental types of parallel processing: (1) A single computer with multiple internal processors, named as a shared-memory parallel processing; (2) A set of computers interconnected through a network, named as a distributed-memory parallel processing [112]. Each of these can be referred to as a Parallel Processing. Two benefits are obtained from parallel processing: (1) splitting a job to two or more small partitions, hence to take less time to complete and thus cut down the time to solution; (2) large scale job that has no way or, if not, impossible to be processed on a single CPU due to the restriction of hardware (i.e., RAM) and time, can become doable after being segmented to many small partitions which could then be handled by many CPUs [113]. Fluent is well suited to parallel processing, because users do not have to write codes to run parallel simulations. The parallel performances using Fluent was investigated and discussed in the chapter.

With development of computers, CFD is widely use to investigate the characteristics of turbulent flow in ducts. In 1992, Gavrilakis [114] numerically simulated mean flow and turbulent statistics through a straight duct with square cross-section. Talukdar et al. [115] simulated heat and mass transfer with CFD for laminar flow of moist air in a 3D rectangular duct. Large eddy simulations (LES) is one of the most popular viscous models in computational fluid dynamics (CFD). It was initially proposed in 1963 by Joseph Smagorinsky to simulate atmospheric air currents [116] and first explored by Deardorff in 1970 [117]. LES is currently applied in a wide variety of engineering applications, including combustion [118], acoustics [119], and simulations of the atmospheric boundary layer [120].

It takes considerable time to simulate a large model with millions of derivatives of functions (DOF) or a medium-sized model with nonlinearities that needs many iterations to reach convergence. To decrease simulation time, parallel processing has been widely applied to CFD. In 2001, William et al. [121] conducted fluid dynamics simulations based on finite discretizations on static grids scale well with parallel processing. Renan et al. [122] performed a multi-objective design optimization concerning the blade shape of a heat exchanger, considering the coupled solution of the flow/heat transfer processes with parallel algorithms. In 2015, Adam et al. [123] investigated the parallel performance of flow over flapping wing using OpenFoam. ANSYS Fluent offers different parallel processing options that increase the model-solving power of Fluent by using multiple processors (also known as cores or CPUs). In the chapter, the test cases were run in ANSYS Fluent on a single computer, which means to run solver on one or more CPUs simultaneously to calculate a computational fluid dynamics (CFD) job. Fluent provides a user-defined function (UDF) in which boundary conditions can be customized with experimental results. Three frequently-used LES sub-grid turbulent velocity models were tested: Smagorinsky-Lilly Model (Lilly model) [116], Wall-Adapting Local Eddy-viscosity Model (WALE model) [124] and Wall Modeled Large Eddy Simulation (WMLES model) [93].

5.2. Efficiency for Parallel Processing

The most obvious benefit of using a parallel computer is the reduction in the running time of the code. Therefore, a straightforward measure of the parallel performance would be the ratio of the execution time on a single processor to that on a multicomputer. This ratio is defined as the speedup factor and is given as [112]

$$R(n) = \frac{t_s}{t_n} = \frac{Execution\ time\ using\ one\ processor}{Execution\ time\ using\ N\ processors} \tag{5.1}$$

where t_s is the execution time on a single processor and t_n is the execution time on a parallel computer. $R(n)$, named as speedup, describes the scalability of the system as the number of processors is increased.

Amdahl's law gives the theoretical speedup in latency of the execution of a task at fixed workload, which is often used in parallel computing to predict the theoretical speedup [125]. The law can be formulated as follow:

$$S_{latency}(n) = \frac{1}{1-Per+\frac{Per}{sp}} \tag{5.2}$$

$S_{latency}$ is the theoretical speedup in latency of the execution of the whole task. sp is the speedup in latency of the execution of the part of the task that benefits from the improvement of the resources of the system. Per is the percentage of the execution time of the whole task concerning the part that benefits from the improvement of the resources of the system before the improvement [125].

5.3. Geometry and Boundary Conditions

To reduce computational time, the simulation was conducted in a half square duct with symmetrical boundary conditions as shown in Fig. 4.1. The height of the geometry is 15.2 mm and the width is 7.6 mm. The total length of the duct is 609.6 mm.

Velocities were measured for each grid at inlet surface (shown in Fig. 4.2) by Particle Image Velocimetry (PIV). Velocity magnitude, turbulent kinetic energy and turbulent dissipation rate are calculated from Eq. 4.2 and Eq. 4.3 and assigned to each grid at inlet as inflow boundary conditions by UDF. Average velocity magnitude is 0.50 m/s, average turbulent kinetic energy is 0.0073 $\mathrm{m^2/s^2}$ and average turbulent dissipation rate is 0.55 $\mathrm{m^2/s^2}$.

5.4. Basic Information about the Computer

The basic information about the computer which was used to run the test cases is shown in Table 5.1:

Table 5.1: Basic Information about the Computer

Windows Edition
Windows Server 2012 R2 Standard
System
Processor: Intel ® Xeon® CPU E5-2630v3@2.40GHz 2.40 GHz (2 processor)
Installed Memory (RAM): 64.0 GB
System Type: 64-bit Operating System, x64-based processor

5.5. Grid-independence Study

The grid-size independence study has been performed to determine the resolution for the simulations. There are four levels of grid sizes: finer, normal, coarser and coarsest. The grid size of each level is 3.38 mm, 1.69 mm, 0.845 mm, and 0.4225 mm, respectively. The number of nodes is 15628, 89348, 613607 and 4305248, respectively. Figure 5.1 shows the velocity profiles at downstream for the grid-independence study. Figure 5.1 is the comparison of average velocity magnitudes on line 1 (Fig. 4.1 (a)) in Z direction. Y axis represents the distance from the location of velocity magnitude to the top surface of the duct. The files with numerical data were output after 12000 steps, 6 s in the simulations. Because the pulse repetition rate for the laser was 7.25 Hz (1/7.25 Hz $\approx$ 0.138 s), the files were recorded every 276 steps (276 step * 0.0005s = 0.138 s). To calculate average velocity magnitudes, 300 exported files were recorded for one period of the simulation time series.

Figure 5.1 illustrates comparison among the results of different grid sizes for WMLES on line 1. It can be found than the results of 0.4225 mm and 0.845 mm grid resolutions are closer to each other than the coarser grid results, especially within the range from Z=0 to Z=3 mm. This

means the 0.845 mm grid is sufficient for WMLES. Therefore, normal grids (0.845 mm) were used in all the cases. Although there is difference between RSM results and WMLES results, it is still reasonable due to different flow models.

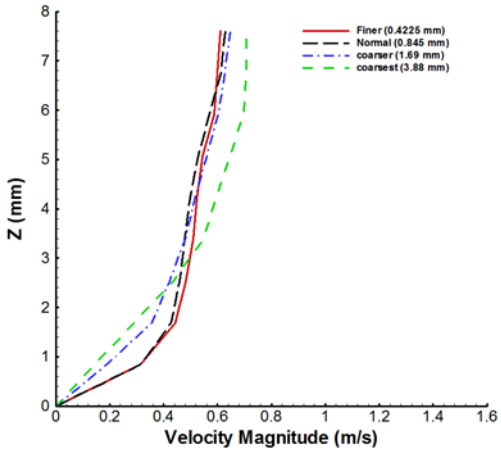

Figure 5.1: Velocity Profiles for Grid-independence Study

5.6. Results and Discussions

Figure 5.2 shows the relationship between the average wall-lock time per iteration (AWTPI) and number of processors. Wall-clock time, or wall time, is the human perception of the passage of time from the start to the completion of a task. The performance is studied for 1, 2, 4, 8 and 16 processors, respectively. Each case runs 10 time steps with 20 iterations in each step. ANSYS Fluent shows AWTPI in performance list after running program. According to Fig. 5.2, wall-clock time and number of processors are in inverse proportion. WMLES model spends the most time among the three models, which means WMLES model has the most complicated sub-grid model among these three LES. Lilly model spends the least time among these three models. When the maximum number of the processors are used to run the program, the efficiency of the processors for these three models are close to each other.

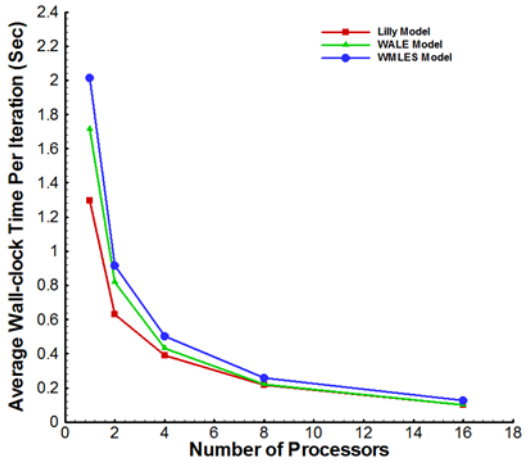

Figure 5.2: Wall-clock Time vs. Number of Processors

Figure 5.3 illustrates the speedup comparison calculated from Eq. 5.1. It can be seen in Fig. 5.3 that although Lilly model needs the least time to run with limit variances, the speedup of Lilly model is the slowest in these three models. The speedup of WALE model and WMLES model are very close to each other.

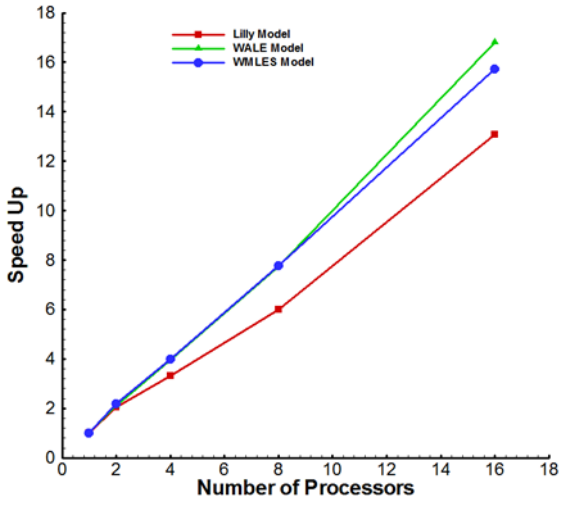

Figure 5.3: Speedup Comparison

Figure 5.4 shows the comparison of the speedup per processor, which indicates the efficiency of each processor when parallel processing is utilized. According to Fig. 5.4, speedup

per process for WALE model and WMLES model is around 1 or over 1, which means the efficiency of each processor is still high when multiple processors are used in simulations. On the other hand, speedup per process decreases significantly, when multiple processors are applied to Lilly model, which explains the speedup of Lilly model is slowest in Fig. 5.3.

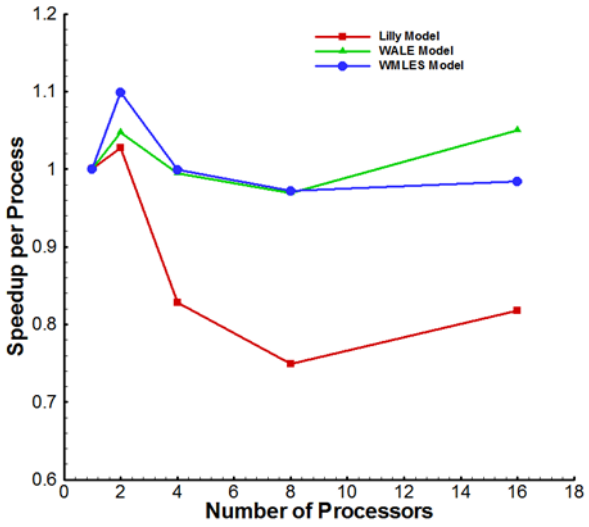

Figure 5.4: Speedup per Processor

Figure 5.5 (from Wikipedia) shows evolution according to Amdahl's law of the theoretical speedup in latency of the execution of a program in function of the number of processors executing it [125]. The speedup is limited by the serial part of the program. For example, if 95% of the program can be parallelized (green line), the theoretical maximum speedup using parallel computing would be 20 times. Furthermore, if 8 processors are applied to the program (green line), the theoretical maximum speedup would be 6 times. Based on comparison between Fig. 5.3 and Fig. 5.5, the parallel portions for WALE model and WMLES model exceed 95%. For Lilly model, when number of processors is less than 8, the parallel portion is lower than 95%, which explains why the speedup for Lilly model in Fig. 5.3 is the lowest. However, when the number of processor is 16, the parallel portion for Lilly model is higher than 95%, which leads to the enhancement of

the slope in Lilly model. In Fig. 5.3, from 8 processors to 16 processors, red line is almost parallel to blue line.

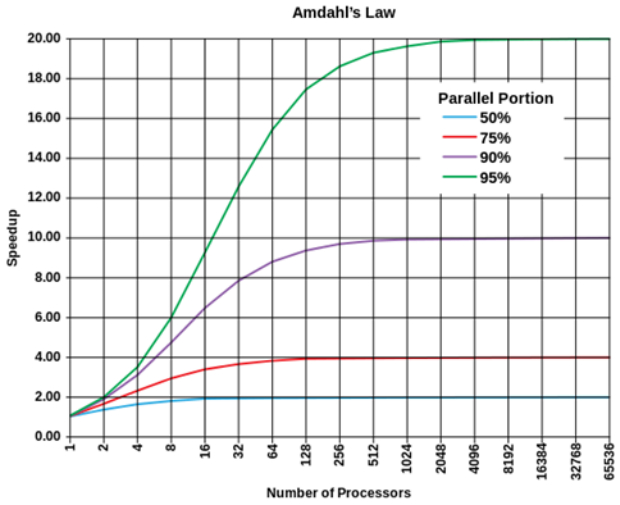

Figure 5.5: Evolution according to Amdahl's Law of the Theoretical Speedup in Latency [125]

5.7. Conclusions for the Effect of Parallel Processing

This chapter discusses the effects of parallel processing on large eddy simulations in ANSYS Fluent. The relationship between the average wall-clock time per iteration and number of solvers is inverse proportion. Lilly model spends the least time to run in three models, but it has the slowest speedup. The speedup of WALE model and WMLES model are very close to each other.

Chapter 6 - Measurement and Numerical Simulations of Heat Transfer and Pressure Drop in a Duct with Smooth Walls

6.1. Introduction

Carefully designed heat exchangers with enhanced surface technology such as micro-fin is an effective way to remove a large amount of heat from small areas. The goal of the design for in-tube surface geometries is to increase heat transfer with a minimum pressure drop penalty. Confirming the design tools used to model these surfaces is thus important and this requires measuring the parameters mentioned above. The special care for the mesh sizes close to the walls and near-wall treatments are discussed in the chapter. Near-wall meshes should be fine enough to resolve the viscous sublayer. Before studying the cases with complex enhanced surface, a smooth surface is investigated.

Heat transfer coefficient or film coefficient is the proportionality constant between the heat flux and the thermodynamic driving force for the flow of heat [126]. The heat transfer coefficient in combination with the surface area achieves an efficiency the drives performance of a heat exchanger. The heat transfer coefficient in the experiment is measured with a semi-local surface average method. The local heat transfer coefficient is determined from the local temperature distribution in the solid base and a surface temperature. The method has been widely used in variety of previous cases [73], [74], [127]. Betz et al. [73] used the method to determine the surface temperatures and Nusselt numbers in a micro-channel heat sink. Some factors affecting the accuracy of the method for the cases are discussed in the chapter.

Measuring pressure drop in the duct is another important problem for the accurate design and optimization of heat exchanger and micro-fins. The pressure drop in horizontal pipes and ducts has been studied by a number of researchers resulting in the development of empirical models and

numerical models to use in the design of new equipment. For example, Hamad et al. [128] investigated the pressure drop in horizontal pipes with different diameters. Chang et al. [129] examined the pressure drop in a square spiral channel with two opposite walls. The geometry for the current study is a simple square duct with smooth surfaces, but some factors, such as turbulence, still impact the accuracy of the pressure measurement. For the cases, an appropriate pressure transducer need to be carefully selected, including measurement range, sizes of the sensor, etc.

The numerical simulations in the chapter were conducted in commercial software, ANSYS Fluent 15.0.0, which contains the broad physical modeling for heat transfer and pressure drop. Fluent offers different parallel processing options [106] to increase the calculation speeds. Furthermore, Fluent provides several options for generating the interfaces between the fluid section and the solid section. The numerical results are compared with experimental results for validation and discussion. The primary goal for the chapter is to validate the experimental setup and the numerical model. Five broad flow cases with different Reynolds numbers are studied and compared. This kind of numerical simulations has been previous used in many cases [130], [131]. However, the previous works did not study the importance of the near-wall region and near-wall treatments. Actually, viscous models and near-wall treatments affect the results of heat transfer and pressure drop significantly. In the study, Reynolds Stress Model (RSM) is applied to simulate the turbulence. The goal of this chapter is to demonstrate that an accurate simulation of the smooth tube can be obtained as a benchmark for the start of the micro-fin tubes. In the future, the relation between turbulence above the micro-fins and heat transfer will be explored. It is a great challenge to obtain the accurate turbulent information above micro-fins in experiments and in numerical simulations.

6.2. Experimental Set-up

The details of the experimental set-up are in Chapter 2.

6.3. Numerical Simulations

The governing equations of the numerical simulations are in Chapter 3.

6.3.1. Geometry

The simulation was conducted in a duct with a copper base as shown in Fig. 6.1 (a). The height and the width of the duct are 15.2 mm. The total length of the geometry is 609.6 mm. Figure 6.1 (b) is the zoom-in view of the inlet with meshes. Green grids are the inlet of the duct and blue grids are the interface between the fluid section and the solid section. Figure 6.1 (C) shows the zoom-in schematic of the downstream and the outlet of the duct without meshes. The geometry of the copper base with black meshes are shown in the Fig. 6.1 (c). Heat transfer coefficient is output from the three red lines located in the interface (line1, line 2 and line 3). The distance of line 1, line 2 and line 3 from exit is 150 mm, 100 mm and 50 mm, respectively. Line 4 is from the top surface and the center of the duct. It is the location where numerical results and experimental results for velocity profiles and kinetic energy profiles are output and compared. Its distance from exit is also 150 mm. The program was running under steady conditions.

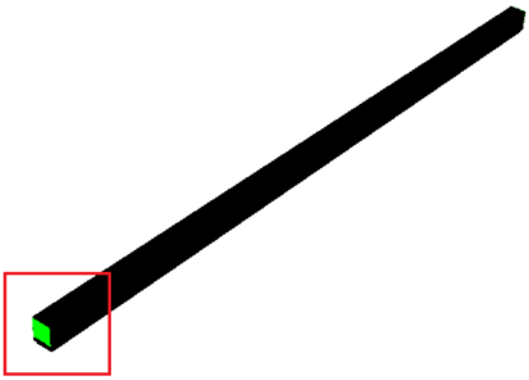

(a)

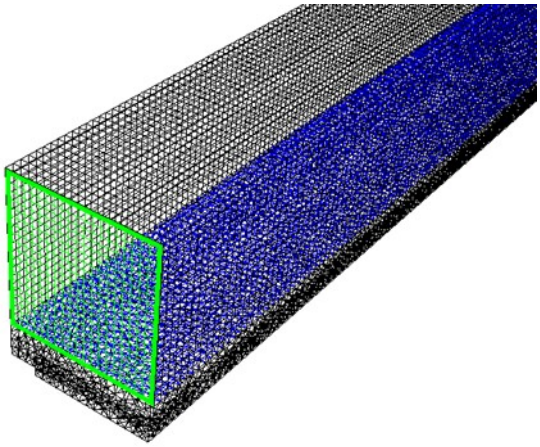

(b)

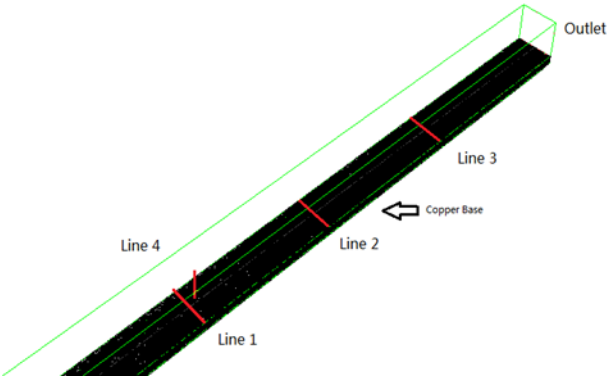

(c)

Figure 6.1: Geometry: (a) Whole Domain with Meshes, (b) Zoom-in View at Inlet, (c) Zoom-in View at the Downstream

6.3.2 Boundary Conditions

Table 6.1 shows boundary conditions set up in numerical simulations. The heat flux in Table 6.1 is the average value calculated from the experimental heat flux above the three arrays. The difference among the heat flux in the table is very small, which is approximately lower than 2%. Therefore, the heat flux is independent on the flow velocity in the duct. The inlet temperatures are also very close to each other.

Table 6.1: Thermal Boundary Conditions for the Five Cases

Velocity (m/s)	0.5	0.9	1.2	1.8	2.3
Inlet Temperature (K)	292.3	292.6	293.3	293.3	293.5
Heat Flux (W/m2)	65400	64647	67007	66965	65249

6.4. Results and Discussions

6.4.1. Heat Transfer Coefficient

Figure 6.2 shows the heat transfer coefficient for the five cases with different Reynolds numbers. Table 6.2 and Table 6.3 illustrate the experimental and numerical results for the all cases. According to Fig. 6.2, the heat transfer coefficient in the numerical simulations matches that in the experiments very well. The maximum difference exiting in the case with U=2.3 m/s is 829 W/m^{2}K. The relative errors are all lower than 10%. Furthermore, the maximum difference for flow temperature is 0.2 K and that for surface temperature is 1.7 K. Therefore, the numerical models predict the heat transfer coefficient in the duct very accurately.

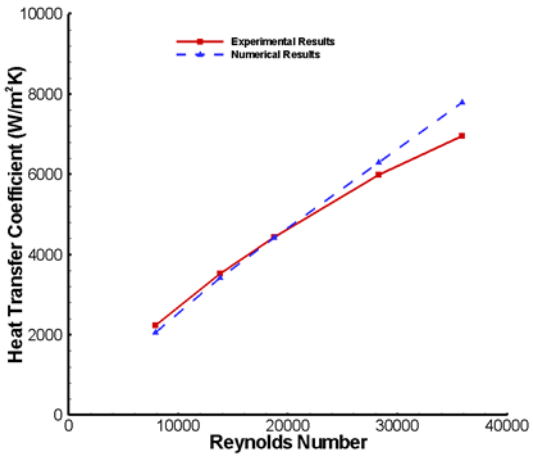

Figure 6.2: Heat Transfer Coefficient for the 5 Cases with Different Reynolds Number

Table 6.2: Experimental Results

Velocity (m/s)	0.5	0.9	1.2	1.8	2.3
Surface Temperature (K)	323.5	312.2	309.3	305.1	303.4
Flow Temperature (K)	293.7	293.4	293.9	293.7	293.9
Heat Flux (W/m2)	66708	66143	68323	67902	66295
Heat Transfer Coefficient (W/m2K)	2236	3521	4436	5987	6957
Pressure Drop (Pa)	136	440	733	1523	2388

Table 6.3: Numerical Results

Velocity (m/s)	0.5	0.9	1.2	1.8	2.3
Surface Temperature (K)	324.7	311.8	308.8	304.1	302.1
Flow Temperature (K)	293.5	293.2	293.8	293.6	293.7
Heat Flux (W/m2)	64458	63775	66197	66329	64759
Heat Transfer Coefficient (W/m2K)	2060	3428	4414	6298	7786
Pressure Drop (Pa)	135	402	694	1467	2314

6.4.2. Pressure Drop

Table 6.2 and Table 6.3 show that pressure drops are very accurately predicted in the duct. The biggest difference exists in the case with U=2.3 m/s, but the relative error (approximately 3%) is still very small. The pressure drop in the numerical simulations is highly associated with the friction coefficient. And the fiction coefficient in the ANSYS Fluent rely on the near-wall treatment. Scalable wall function is selected to simulate the flow characteristics near the walls. Scalable wall functions avoid the deterioration of standard wall functions under grid refinement below y^*<11. For grids that are coarser than y^*>11, the standard wall functions are identical.

6.4.3. Velocity Profile and Kinetic Energy Profile

Figures 6.3 (a) and 6.4 (a) illustrate the velocity profiles for the two cases with U=0.5 m/s and U=0.9 m/s. Experimental results are measured by Particle Image Velocimetry (PIV). The velocity profiles for numerical simulations match the experimental results very well. All the numerical results for the velocity are within the uncertainty bound of the experimental results. Figures 6.3 (b) and 6.4 (b) show the profiles of turbulent kinetic energy. For the lower velocity

case, the kinetic energy simulated by the numerical model are lower than the experimental results within the region close to the wall. The profile of kinetic energy for higher velocity are even worse. Grid sizes lead to the bad results. In the future, grid independence study and grid size close the wall will be studied.

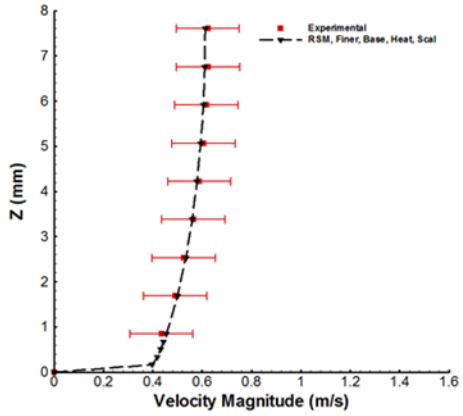

(a) Velocity Profile

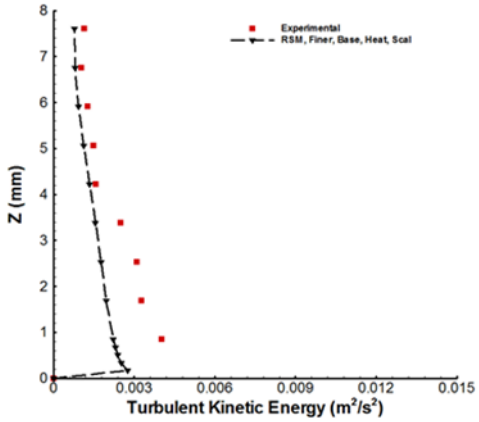

(b) Turbulent Kinetic Energy

Figure 6.3: Experimental Results and Numerical Results on Line 4 for *U*=0.5 m/s

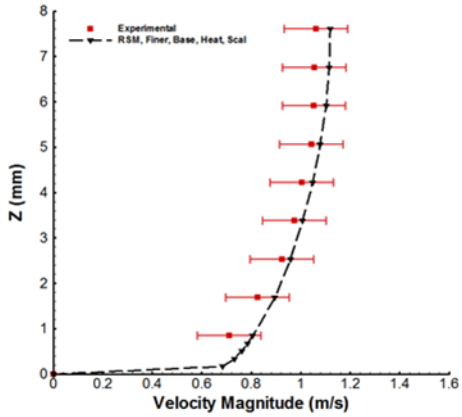

(a) Velocity Profile

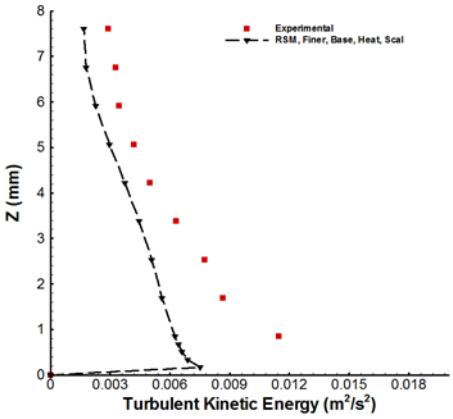

(b) Turbulent Kinetic Energy

Figure 6.4: Experimental Results and Numerical Results on Line 4 for *U*=0.9 m/s

6.5. Conclusions

The numerical model success to simulate the heat conduction, heat convection, pressure drop and flow characteristics with in the geometry with the fluid section and solid section. The numerical results simulated by the numerical model for the smooth tube match the experimental results very well. In the future, the numerical model will be modified and improved for the simulations of the tube with micro-fins.

Chapter 7 - The relationship between turbulent structures and heat transfer in micro-fin enhanced surfaces using large eddy simulations and particle image velocimetry

7.1. Introduction

Internally enhanced surfaces such as micro-fins are an important class of heat transfer enhancement in commercial applications such as air conditioners and refrigerators. Micro-fins are characterized by fin structures less than 1 mm in height that are used in ducts and tubes of a significantly larger diameter. One typical goal of micro-fin design is to increase heat transfer with a minimum pressure-drop penalty. It has been generally reported that two key factors lead to the enhancement of heat transfer. These are the area increase and fluid mixing in the inter-fin region caused by flow separation and reattachment [34]. Normally, researchers follow a fixed procedure to analyze the macro relationship between heat transfer and micro-fins: (1) the study identifies a range of geometries of interest, and physical or numerical models are prepared; (2) then, all collected experimental and numerical results are shown in common plots with heat transfer characteristics (heat transfer coefficient or Nusselt number) versus Reynolds numbers; and (3) finally, physics and mechanics behind the plots are discussed, and correlations are proposed. The correlations reveal how newly designed geometries, i.e., width, height, shape, angle, etc., affect the heat transfer and pressure drops, but are not predictive for new geometries because the detailed flow physics are not identified. Very few studies have explored the link between flow characteristics and heat transfer both experimentally and numerically. The detailed time-resolved characteristics of flow near the wall around the micro-fins are not well understood because experimental and numerical data are limited, which gave rise to some currently unsolved problems.

First, in most cases, it is not well understood why increases in heat transfer are larger than area increases in the micro-finned tubes [22], [24], [25], [34], [36], [41], [132]–[135]. Second, why do internally micro-finned tubes usually have a lower heat-transfer-enhanced ratio in the laminar and transition flow regions [22]? The current study proposes some novel methods of collecting and analyzing the data to figure out the physics and mechanics driving the performance of the micro-finned tubes. The goal of the chapter was not to find a new Reynolds number-based correlation but to find flow patterns responsible for heat transfer enhancement and understand the mechanisms that cause it.

In a micro-finned tube, a certain number and shape of protruding micro-fins were extruded or rolled onto the tube wall. For the convenience of collecting experimental data, the primary test section in the current study was a square duct with clear upper and side walls (vapor-polished polycarbonate) on a solid copper block as shown in Fig. 1 (a). The fin structure matched one used by Webb et al. [34] and was manufactured on the top of the copper block through micro-machining. Webb chose the height of the fin to be located in the viscous sublayer. The fluid flowing in the duct was water. A commercial, telescopic, particle image velocimetry (PIV) system captured flow characteristics in the duct. PIV is a powerful tool used in many configurations [18], [19], [76]–[78]. However, it is rarely used to collect flow characteristics near heat transfer fins. Dupuis et al. [49] identified and analyzed flow structures in pyramidal-pin fin arrays for laminar flow. Their fins were sprayed on aluminum substrates with dimensions of 7 mm × 51 mm. Fin height was 1.0 mm, and fin base length was 1.5 mm. In their study, PIV measured not only instantaneous velocity fields but also other related properties such as turbulent intensity. The flow in their study was pure nitrogen. Flow structures obtained in the micro-channel affected flow stability, structure and turbulence level, which contributed to the increase of the convective heat transfer coefficient. In

2017, Xia et al. [50] presented experimental results of the laminar-flow behavior of water in circular micro pin-fin, square micro pin-fin and diamond micro pin-fin heat sinks with PIV. The entire dimension with the micro-pin fin arrays was 10 mm (length) × 2.2 mm (width) × 0.1 mm (height). Vortexes in their study explained why the best heat transfer enhancement behaviors were in the diamond micro pin-fin heat sink. With an increasing Reynolds number, vortexes in the diamond micro pin-fin occurred the earliest and had the most complicated structure, which effectively improved the mixing of fluid and heat transfer. In the above examples, PIV was applied to micro-channels. For the current study, PIV was used in a larger passage with smaller micro-fins (micro-fin height/duct height$\approx$0.022).

The experimental data also provided an opportunity to validate numerical techniques. Previously, there had been numerous numerical investigations of the micro-fins [47]–[49], [51]–[54]. k-ε turbulence models were used in most of the papers mentioned above. However, two drawbacks existed in the turbulence model. First, the k-ε turbulence model was not suitable for the laminar and transition flow region of micro-fin flows, which led to faulty predictions of heat transfer and pressure drops [55]. Second, the turbulence model developed from Reynolds Averaged Navier–Stokes equations (RANS) was not able to simulate the dynamic process of fluid mixing caused by flow separation and reattachment within the inter-fin region. By carefully utilizing our validation data, we revealed that a large eddy simulation (LES) with a localized dynamic kinetic energy subgrid-scale model (LDKM) [94] predicted the flow observed with PIV. The authors were aware of only a few systematic studies in the literature on implementing LES in wall-bounded flows with heat transfer in micro-fins. In 2019, Campet et al. [54] presented a LES approach to study the turbulent flow in a single-started helically ribbed tube. Numerical simulations in the chapter were conducted in ANSYS Fluent, which comprised the broad physical

modeling capabilities needed to model flow and heat transfer. Fluent offers different parallel processing options [106] to increase calculation speeds. In the current study, a stream-wise periodic boundary condition significantly reduced computational time without sacrificing accuracy. In such flow configurations, the geometry varies in a repeating manner along the direction of the flow, leading to a periodic, fully developed flow regime in which the flow pattern repeats in successive cycles [55]. Campet et al. [54] also used the similar periodic boundaries.

The focus of this work was to experimentally and numerically investigate flow patterns responsible for heat transfer enhancement and understand the mechanisms behind the phenomena. Three "cases" were investigated in this study representing three different velocities: case 1) average velocity $\approx$ 0.5 m/s, Reynolds number $\approx$ 7600; case 2) average velocity $\approx$ 0.9 m/s, Reynolds number $\approx$ 14,000; and case 3) average velocity $\approx$ 1.8 m/s, Reynolds number $\approx$ 28000.

7.2. Numerical Simulations

7.2.1. Geometry and Mesh Sizes

The simulation was conducted in a short duct with periodic boundary conditions, as shown in Fig. 7.1, to reduce computational time. The upper part was a square duct with water flow. Height and the width of the fluid part were15.2 mm. Total length of the numerical geometry was 20.6 mm. In the duct with smooth surfaces, line 1 in Fig. 7.1 (a) was the location where experimental results and numerical results were compared. Line 1, starting from the solid-fluid interface, was at the center of the interface. Lines 2 and 3 in Fig. 7.1 (b) showed the positions where results were output for the micro-finned duct. Line 2 was from the tip of the micro-fins and line 3 was from the bottom of the micro-fins. Center planes are shown in Figs. 7.1 (a) and (b). Arrows in Fig. 7.1 illustrate the direction of water flow.

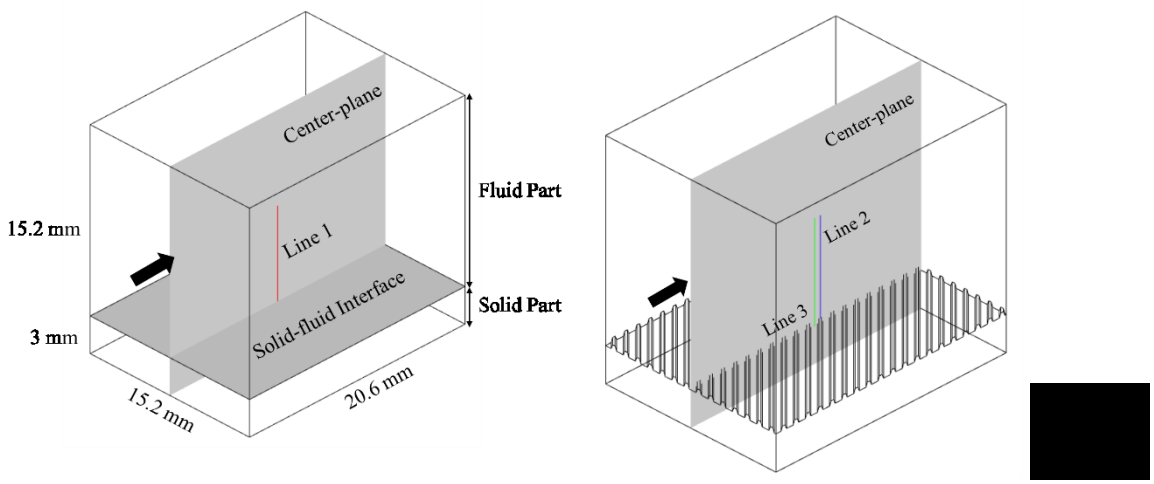

(a) (b)

Figure 7.1: Geometries (a) smooth duct and (b) micro-finned duct

Mesh sizes for LES are dependent on the Reynolds numbers. If mesh sizes are too coarse, it can lead to a bad prediction of flow characteristics. Typical resolution requirements for LES are [55]

$$\Delta x^+ = 40 \tag{7.1}$$

$$\Delta y^+ = 20 \tag{7.2}$$

where Δx^+ is the non-dimensional grid spacing in the stream-wise direction and Δy^+ in the span-wise, with the definitions as follow:

$$\Delta x^+ = \frac{u_\tau \Delta x}{\nu} \tag{7.3}$$

$$\Delta y^+ = \frac{u_\tau \Delta y}{\nu} \tag{7.4}$$

In the study, Δx was equal to Δy. Therefore, Δx^+ was equal to Δy^+. Wall friction velocity, u_τ, was defined as

$$u_\tau = \sqrt{\frac{\tau_w}{\rho}} \tag{7.5}$$

where τ_w was wall shear stress. Wall shear stresses are calculated by pressure drops in the experiments. Mesh sizes for all cases are shown in Table 7.1. The mesh around the solid-fluid interfaces required special attention to improve the numerical prediction of *HTC*. Face sizing was applied to both sides (i.e., solid side and fluid side) of the interface to make the mesh changing around the interface go smoothly. Time-step sizes shown in Table 7.1 satisfy the equation, $dt \leq \frac{\Delta}{U}$ [111].

Table 7.1: Mesh sizes and time-step sizes

Smooth Duct			
Velocity (m/s)	0.5	0.9	1.8
Mesh Sizes (mm)	0.30	0.25	0.20
Time Step Sizes (s)	0.0005	0.0002	0.0001
Δx^+, Δy^+	11.5	13.1	19.3
Micro-finned Duct			
Velocity (m/s)	0.5	0.9	1.8
Mesh Sizes (mm)	0.20	0.15	0.10
Time Step Sizes (s)	0.0002	0.0001	0.00005
Δx^+, Δy^+	15.9	18.5	16.3

7.3. Validation and Comparison

For validation and further discussion, *HTC*, pressure drops, velocity profiles, *TKE* profiles, and vector fields in the numerical simulations were compared with those in the experiment.

7.3.1. Heat Transfer Coefficient and Pressure Drops

Fig. 7.2 (a) shows the experimental and numerical heat transfer coefficient for all cases with uncertainty. The experimental results matched the numerical results very well. All numerical results were within the uncertainty. The heat transfer coefficient increased with the increase of the Reynolds number. The heat transfer coefficients in the micro-finned duct were higher than those in the smooth duct. Fig. 7.2 (b) demonstrates the ratio of heat transfer coefficient in the micro-finned duct to that in the smooth duct. The ratio in transition flow was relatively lower than those

in the fully developed flow. Furthermore, the ratio of heat transfer coefficient was higher than that of area increase (1.6 times). Therefore, enhanced areas of the surfaces were not the only reason for the increase in heat transfer coefficient. Figs. 7.2 (a) and (b) also show Webb's results. Although the micro-fins in Webb's paper were in a circular pipe, results measured in the study were still close to theirs.

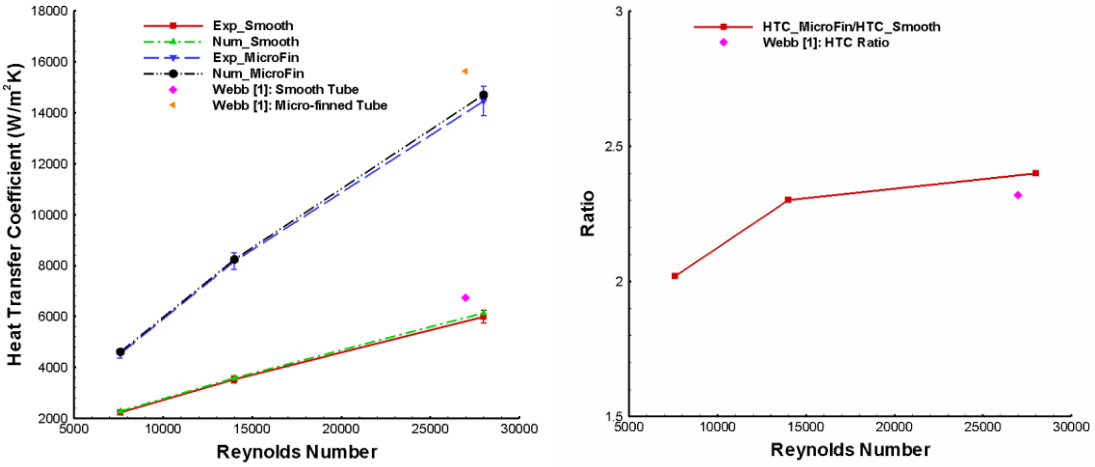

(a) (b)

Figure 7.2: (a) Experimental and numerical heat transfer coefficient; and (b) ratio of *HTC* in the micro-finned duct to *HTC* in smooth duct

Experimental and numerical pressure drops are shown in Fig. 7.3 (a). The maximum relative error between the experimental results and numerical results was approximately equal to 15 percent. Periodic boundary conditions used in the numerical simulations mainly caused the relative error. Fig. 7.3 (b) shows the ratio of pressure drop in the micro-finned duct to that in the smooth duct. The ratio decreased with the increase of Reynolds number. Based on Fig. 7.2 (b) and Fig. 7.3 (b), the micro-fins were better suited for the high Reynolds number cases (around Re $\approx$ 28000).

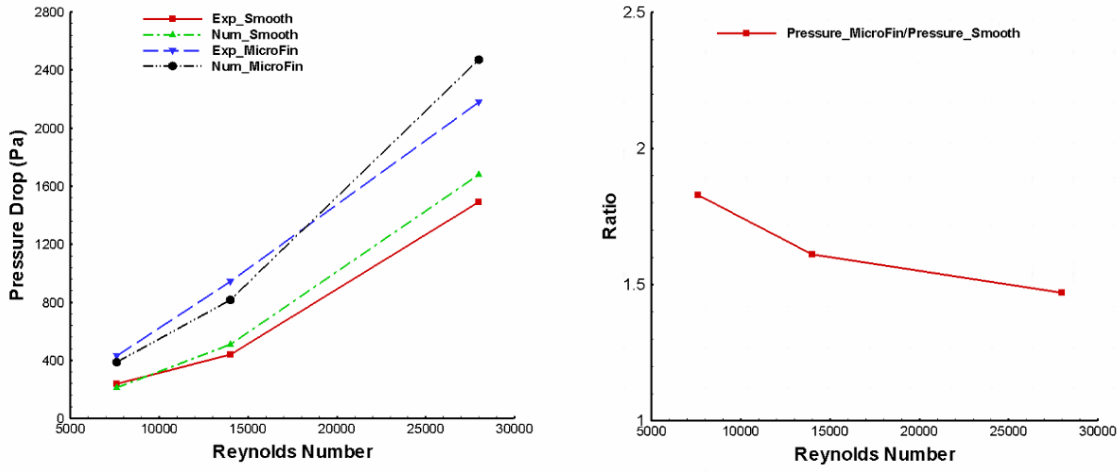

(a) (b)

Figure 7.3: (a) Experimental and numerical pressure drop; and (b) ratio of pressure drop in the micro-finned duct to that in smooth duct

Table 7.2 shows the *HTC* and pressure drops for case 2 with different turbulent models. The numerical results were compared with the experimental results. After the comparison, the numerical simulation with LDKM had the smallest relative error for the prediction of *HTC* and pressure drop. Therefore, LES with LDKM was selected to use in the study.

Table 7.2: *HTC* and pressure drops for case 2 with different turbulent models

	Experimental	LDKM	Lilly	WMLES	RSM	Realizable *k-ε*
HTC (W/(m2·K))	8153.6	8249.4	9792.3	9945.6	8873.1	6112.8
Relative Error of *HTC*	N/A	1.2%	20.1%	22.0%	8.8%	25.0%
Pressure (Pa)	941.4	817.2	733.9	752.7	791.6	648.6
Relative Error of Pressure	N/A	13.2%	22.0%	20.0%	15.9%	31.1%

7.3.2. Velocity Profiles

Fig. 7.4 displays velocity profiles on line 1 in the smooth duct for the three cases. Y-axis, i.e., Z (mm), represents the distance from the location of the velocity magnitude to the bottom of

the duct. It is obvious the velocity profiles simulated by LES with LDKM matched the PIV results very well.

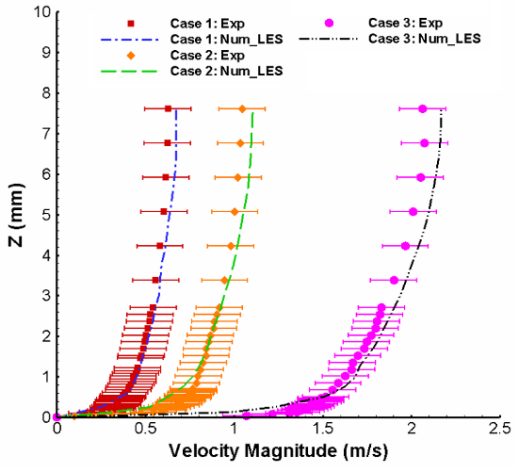

Figure 7.4: Experimental and numerical velocity profiles on line 1 in the smooth duct

The numerical velocity profiles in the micro-finned duct simulated by LES on lines 2 and 3 are shown in Figs. 7.5 (a), (b) and (c). The Y-axis in Fig. 7.5 represents the distance from the velocity location to the bottom of the micro-fins. Therefore, the velocity profiles within the region, $Z \leq 0.33$ mm (micro-fin height), were all zeros. Numerical velocity profiles agreed with those measured by PIV very well. Numerical velocity profiles were all within the uncertainty of the experimental velocity profiles. Fig. 7.6 illustrates the zoom-in view of experimental and numerical velocity profiles near the bottom region in the micro-finned duct for the three cases. The increasing slopes of the velocity profiles above the micro-fin bottom were different from those on the tip. The difference can be seen in the region around $Z = 0.33$ mm. Then the velocity profiles from the tip and the bottom of the micro-fin merged with the increase of Z. Therefore, the micro-fins affected the surrounding velocity profiles significantly.

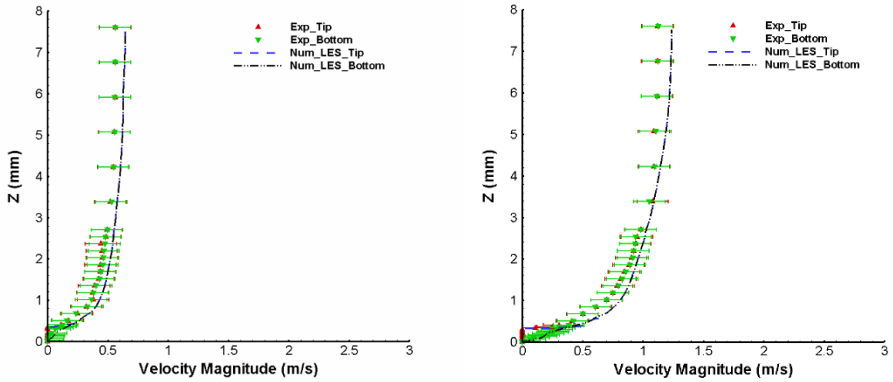

(a) (b)

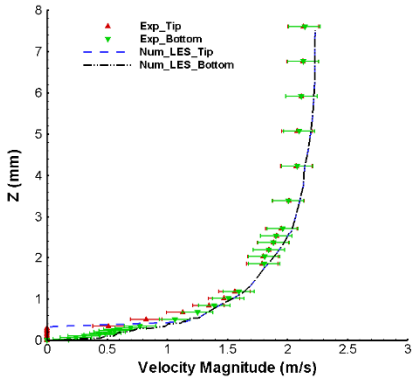

(c)

Figure 7.5: Experimental and numerical velocity profiles on lines 2 and 3 in the micro-finned duct (a) case 1, (b) case 2, and (c) case 3

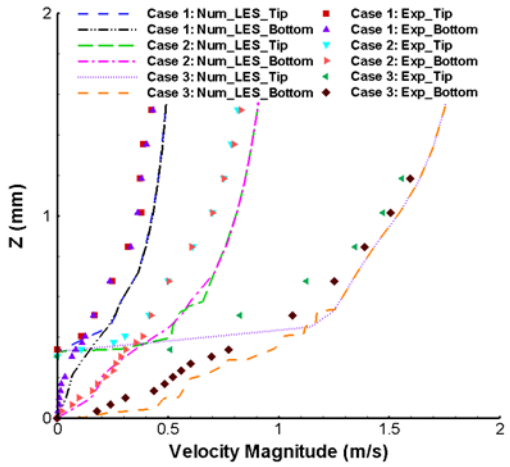

Figure 7.6: Zoom-in view of experimental and numerical velocity profiles in the micro-finned duct for the three cases

7.3.3. Turbulent Kinetic Energy Profiles

Figs. 7.7, (a), (b) and (c,) show the experimental and numerical *TKE* profiles on lines 1, 2, and 3 for the three cases, respectively. The experimental *TKE* profiles agreed with the numerical results very well. The *TKE* profiles for the micro-finned duct within the region, Z $\leqslant$0.33 mm, were lower than those for the smooth duct. *TKE* was weakened within the region by the gap between two micro-fins. Then *TKE* in the micro-finned duct increased, with Z increasing until Z $\approx$ 0.5 mm. Different regions of the micro-fins disturbed the *TKE* differently.

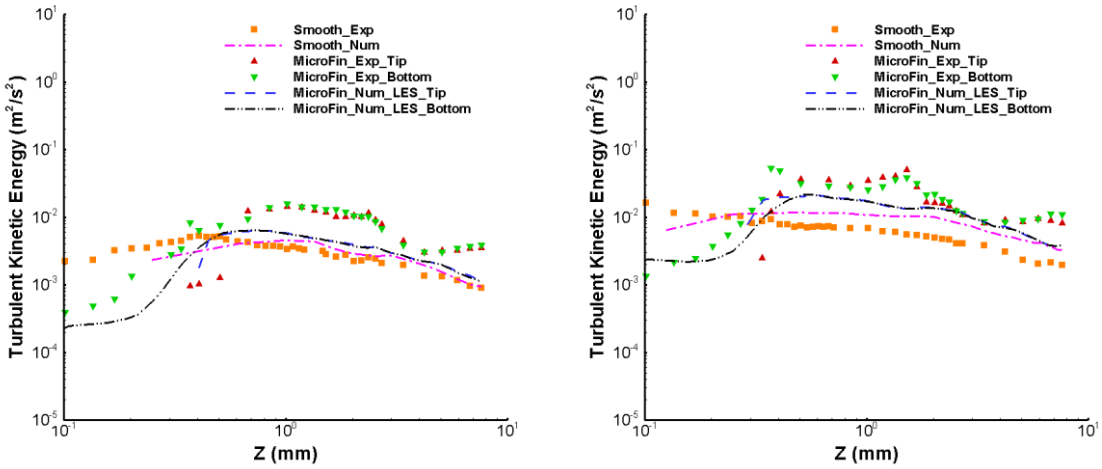

(a) (b)

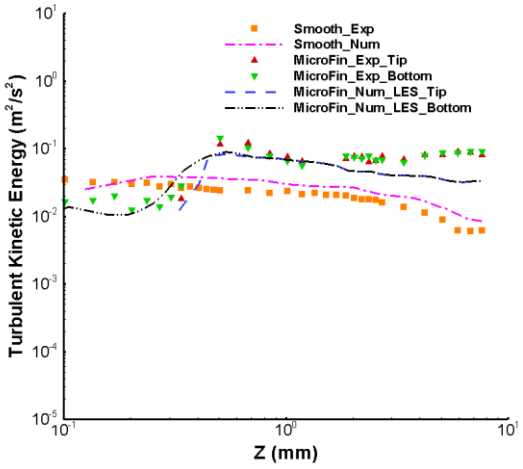

(c)

Figure 7.7: Experimental and numerical *TKE* profiles on lines 1, 2, and 3 in the smooth and micro-finned duct (a) case 1, (b) case 2, and (c) case 3

7.3.4. Vector Fields

Figs. 7.8 (a) and (b) show the transient vector fields' output from the PIV data and numerical simulations, respectively, in the X-Y plane of the micro-finned duct for case 2. The size of the two domains was 3mm × 3 mm, which was the same as the PIV camera's view. Location of

the plane was 1 mm above the tips of the micro-fins. The micro-fins were still seen in the PIV image. In general, vector fields in the numerical simulation were similar to those in the experiment. Similar flow patterns existed around the region.

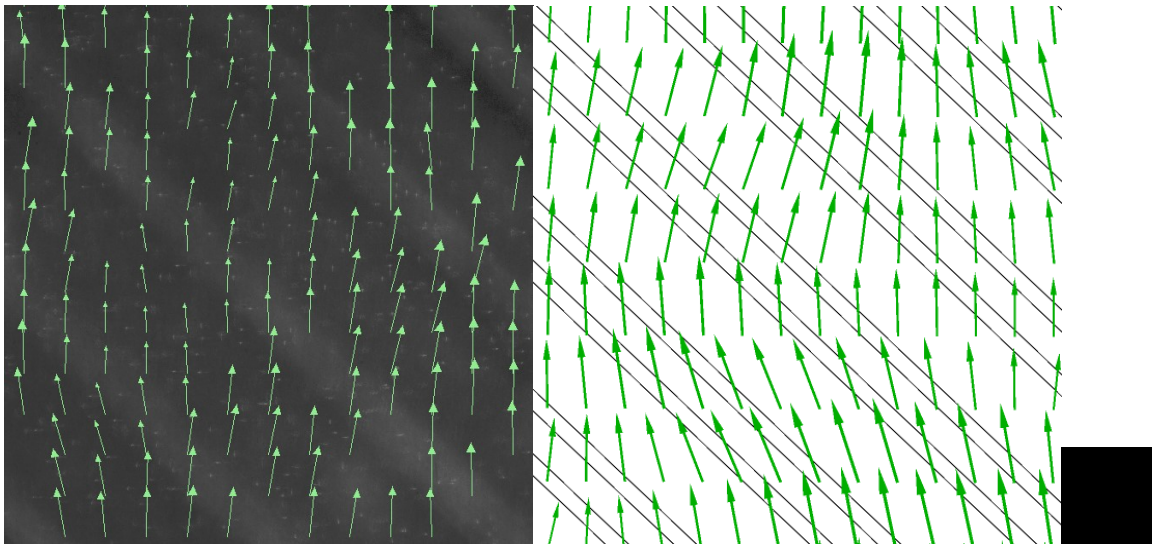

(a) (b)

Figure 7.8: Transient vector fields' output from (a) PIV data and (b) numerical simulations

7.4. Results and Discussion

Relationships between the flow pattern and heat transfer are highlighted in this section. Wall-bounded turbulent flows can generally be broken into three zones: viscous region, log-law region, and bulk flow zones. Two of these zones are particularly important to the micro-fin. Zone 1 (viscous region) here is defined as the gaps between the micro-fins. Zone 2 (log-law region) is the location above the tips of the micro-fins, and here is defined as a height of 4 mm above the fin.

7.4.1. Relationships between *Q* Criterions and Heat Flux

Fig. 7.9 (a) shows the Q criterion in zones 1 and 2 for case 1 in the 3D domain at 5.5 s. The Q criterion value in Fig. 7.9 (a) is 50000 s^{-2}. Black colors on the interface are locations where the heat flux was greater than 20000 $W \cdot m^{-2}$, which is approximately equal to the double average heat flux for case 1. In Fig. 7.9 (a) with Q = 50000 s^{-2}, the coherent structures generally

corresponded to the heat flux. To further analyze details of relationships between the coherent structures and the heat flux, spot 1 in Fig. 7.9 (a) was zoomed-in on and shown in Figs. 7.9 (b)-(h). At t = 5.503 s, there were no coherent structures with Q = 50000 s^{-2} in the spot. Then after a short time, at t = 5.504 s, a tiny coherent structure was generated (an arrow points out the coherent structure). After 0.001 s more, the coherent structure became larger in Fig. 7.9 (d). With growth of the coherent structure, a location with the heat flux greater than 20000 $W \cdot m^{-2}$ (an arrow points it out) gradually appeared in Fig. 7.9 (e). This high-heat flux region appeared on the next downstream micro-fin face, because the coherent structure showed the development of a swirl caused by flow separation. According to Figs. 7.9 (f)-(h), size of the area for the heat flux increased with growth of the coherent structure, which directly demonstrated that the coherent structure affected high-heat flux greater than 20000 $W \cdot m^{-2}$.

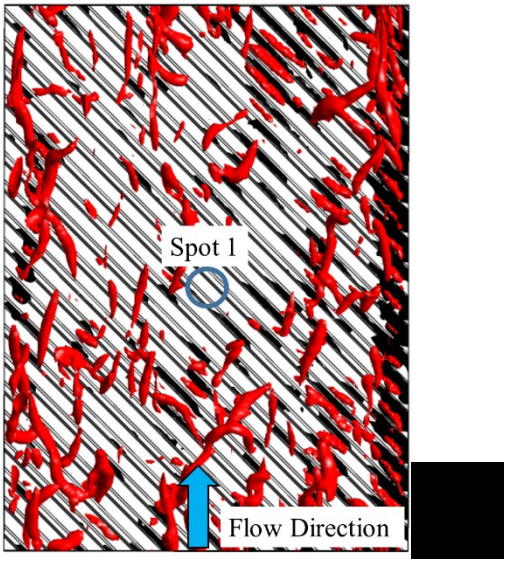

(a)

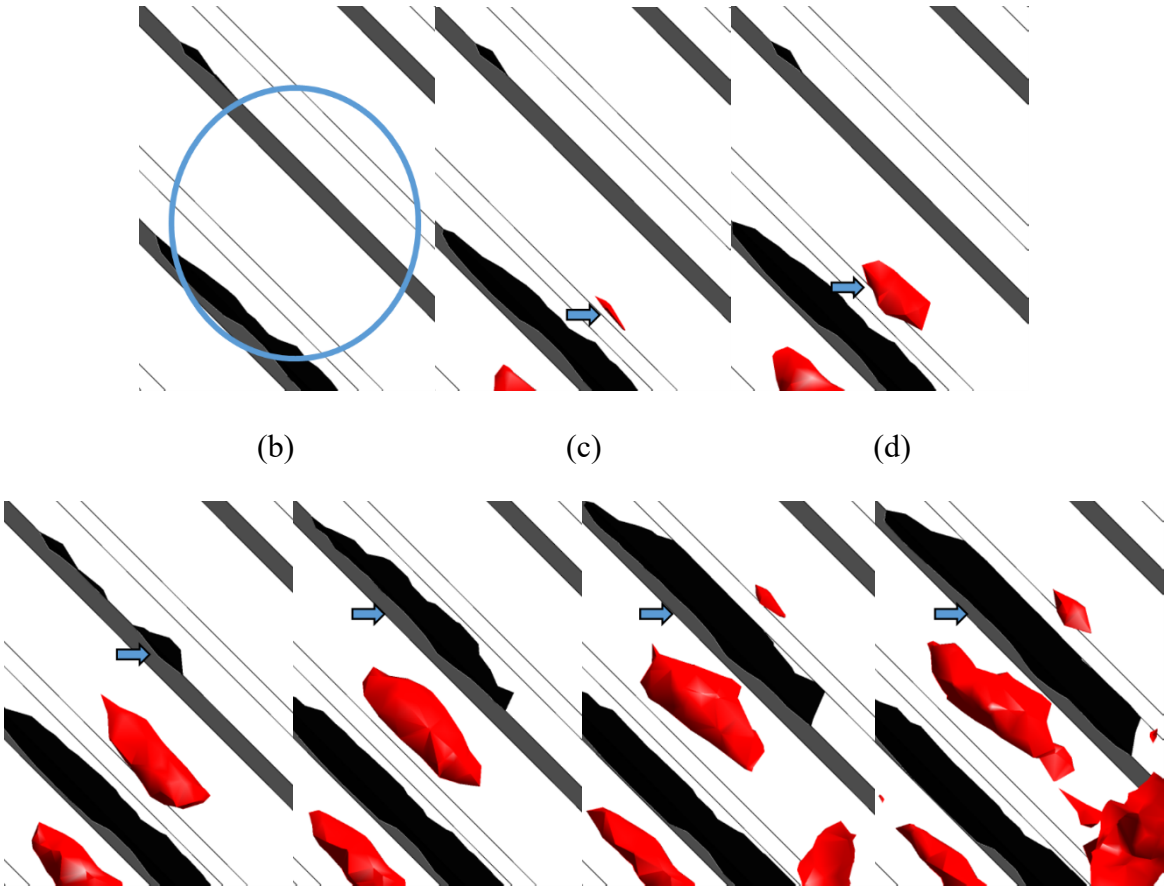

(b) (c) (d)

(e) (f) (g) (h)

Figure 7.9: (a) Q criterions (Q = 50000 s^{-2}) and heat flux for case 1 at 5.5 s; (b)-(h) are zoom-in views of spot 1 at (b) 5.503 s, (c) 5.504 s, (d) 5.505 s, (e) 5.506 s, (f) 5.507 s, (g) 5.508 s, and (h) 5.509 s.

7.4.2. Swirls in zone 1 and zone 2

Fig. 7.10 shows the contours of velocity-swirling vectors for the three cases at t = 5.501 s on the center plane. The Arrow shows the direction of water flow. The figure clearly highlights the difference in transition and fully turbulent flows. Figs. 7.10 (b) and (c) show nearly every fin gap has significant swirl while the lowest Reynolds number has very few. Spot 1 in Fig. 7.10 (a) shows significant swirls existing above the fin. The larger swirls pass by the micro-fins in zone 2, but are not strong enough to penetrate zone 1 completely. The Swirls in zone 1 reinforce the fluid

mixing between zones 1 and 2, which enhances the heat transfer between the two zones. This is one reason why the higher heat-transfer-enhanced ratio occurs in the turbulent flow region (one answer for the second problem in the introduction). It should be noted that Fig. 7.10 represents one moment in time and is not an average plot.

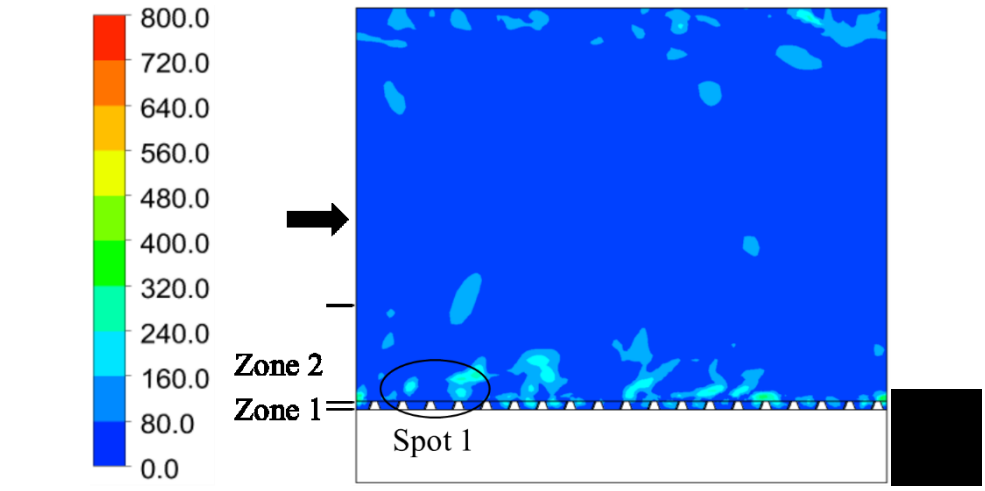

(a)

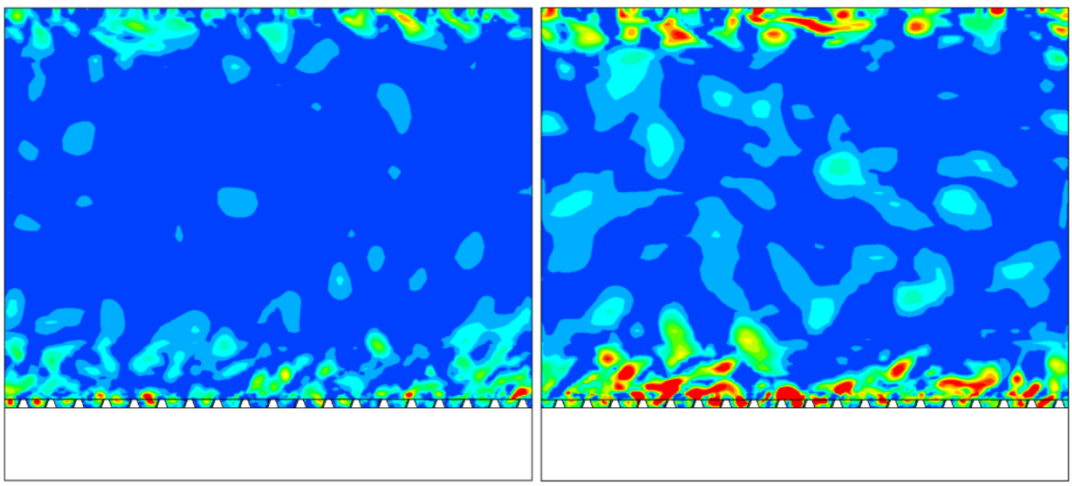

(b) (c)

Figure 7.10: Contours of velocity swirling vector at 5.501 s (a) case 1, (b) case 2, and (c) case 3

The LES simulations can also be used to study the dynamic formation and decay of the swirls between the fins hinted at in the previous figures. Fig. 7.11 shows a time-resolved set of plots for case 2. The swirl structures shown in zones 1 and 2 can be seen moving and evolving. Extended movies show the swirl structures between the fins forming when larger structures in zone 2 pass over the fin. In some cases, intense swirls can be seen jumping to the next fin passage. Fig. 7.9 highlights the formation of these more-intense inter-fin swirls are associated with high-heat fluxes and thus enhanced heat transfer. Another observation was that fluid mixing between zone 2 and the bulk flow occurs much more often for cases 2 and 3.

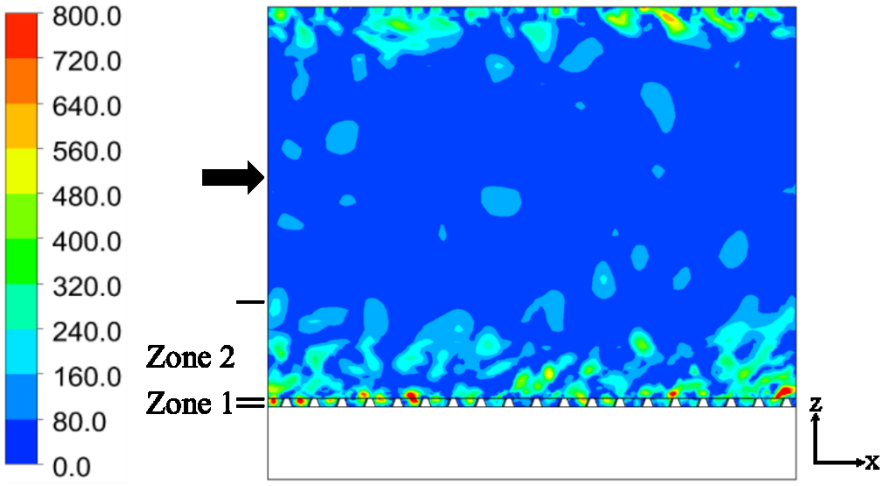

(a)

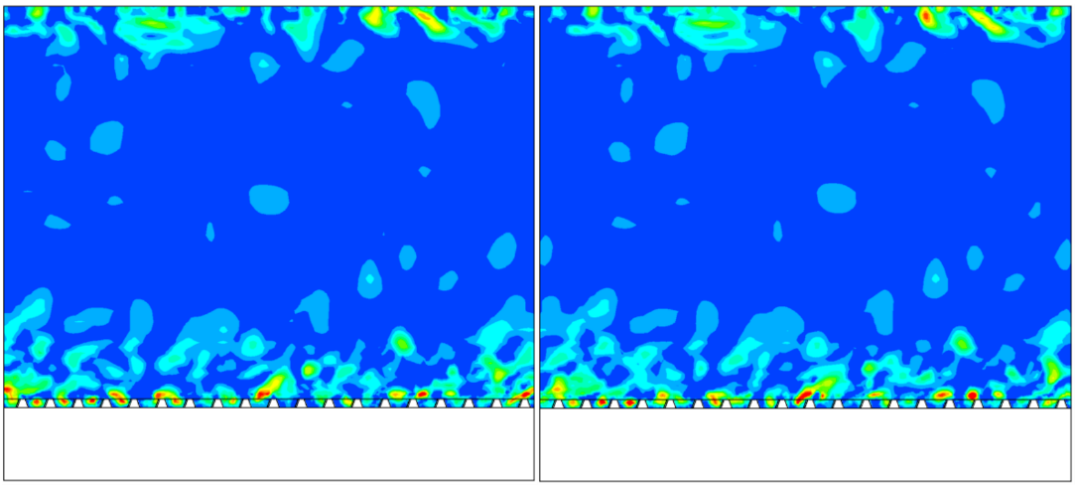

(b) (c)

Figure 7.11: Contours of velocity swirling vector for case 2 at (a) 5.501 s, (b) 5.502 s, and (c) 5.503s

7.4.3. Temperature Contours on the Center Plane

Fig. 7.12 illustrates temperature contours for the three cases in the smooth duct. There are clear temperature sublayers from the bottom to the top in the domain. It is easy to distinguish temperature contours layer by layer, even for case 3 with the highest Reynolds number. Fig. 7.13 displays temperature contours for the three cases in the micro-finned duct. In Fig. 7.13 (a), the temperature contours became unstable and the cool water in zone 3 penetrated almost entirely through zone 2 to the micro-fin surface. This process created large oscillation of temperature boundary layers. In Figs. 7.13 (b) and (c), the process is enhanced with the Reynolds number, and temperature contours are broken and compressed indicating higher heat transfer coefficients. Fluid mixing among the different temperature layers enhances the heat transfer coefficient in the micro-finned surface.

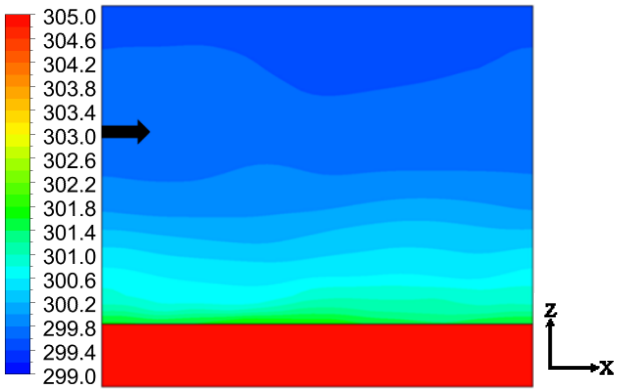

(a)

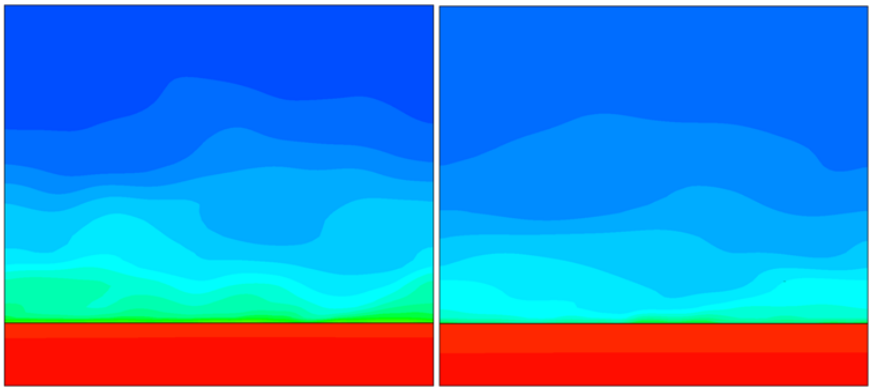

(b) (c)

Figure 7.12: Temperature contours in the smooth duct at 5.5 s (a) case 1, (b) case 2, and (c) case 3

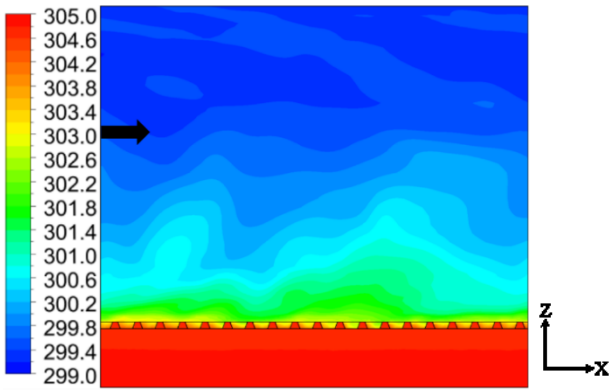

(a)

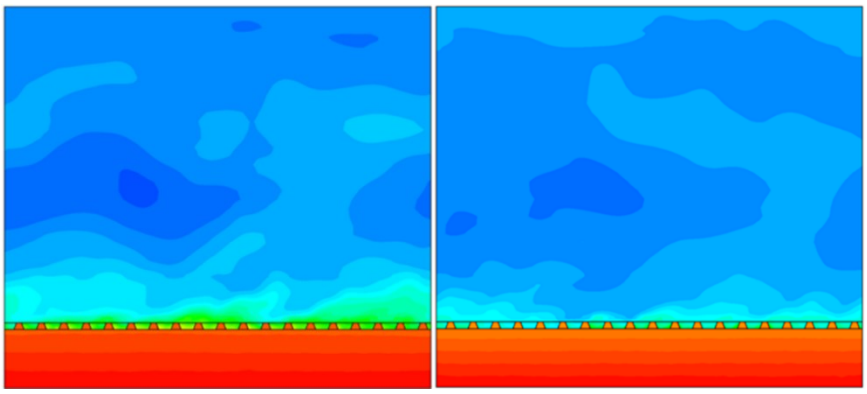

(b) (c)

Figure 7.13: Temperature contours in the micro-finned duct at 5.5 s (a) case 1, (b) case 2, and (c) case 3

7.4.4. Velocity Contours on the Center Plane

Fig. 7.14 illustrates velocity contours in the smooth duct and micro-finned duct for case 2. Fig. 7.14 is taken from the same time step as Figs. 7.12 and 7.13 and thus can be directly compared. First, it is interesting to compare velocity contours between smooth and micro-finned surfaces. Disruption of the zone 2 velocity profiles is clear. This disruption led to higher velocity gradients at the wall, and thus the increased pressure drop was associated with the micro-finned surfaces. The pressure drop was composed of shear and pressure drag, and the later could not be seen on the plots, so an incomplete picture was presented. Mann et al. have more information on the shear and pressure components of the pressure drop for such micro-finned surfaces. It is also useful to compare the temperature contour plots with the velocity plots. Water has a higher Prandtl number, so we did not expect identical contour plots. Some structures in zone 2 between Figs. 7.13 and 7.14 are the same. This is an area of active research and more study.

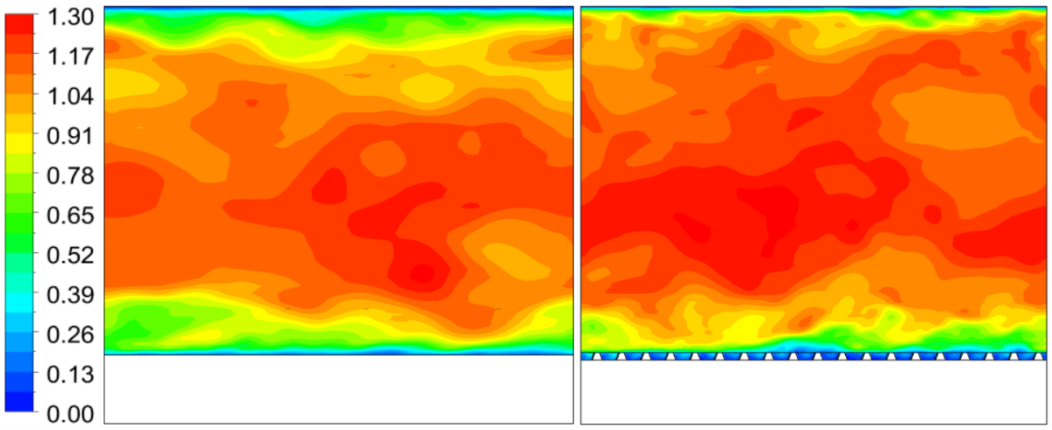

(a) (b)

Figure 7.14: Velocity contours for case 2 at 5.5 s (a) smooth duct, and (b) micro-finned duct

7.4.5. Distributions of Coherent Structures

Figs. 7.15 and 7.16 give another import view of the flow structures within the duct. These figures used Q criterions of 50000 s^{-2} in the smooth duct and in the micro-finned duct, respectively, for the three cases. It is noticeable the coherent structures rose with the increase of the Reynolds number. There were no coherent structures with Q = 50000 s^{-2} in Fig. 7.15 (a). Comparing Figs. 7.15 and 7.16, when the Reynolds number was identical, there were more coherent structures in the micro-finned duct. The micro-fins on the bottom enhanced the production of the coherent structures, which improved the fluid mixing. The fluid mixing generated an effect to enhance the communications among the different temperature layers, which increased the heat transfer coefficient in the micro-finned duct. The micro-fins in the duct not only increased the area of the solid-fluid interfaces but also boosted the fluid mixing among the different temperature layers. Due to the bonus effect of the micro-fins, increases of heat transfer were larger than the area increases in the micro-finned tubes (one answer for the first problem in the introduction).

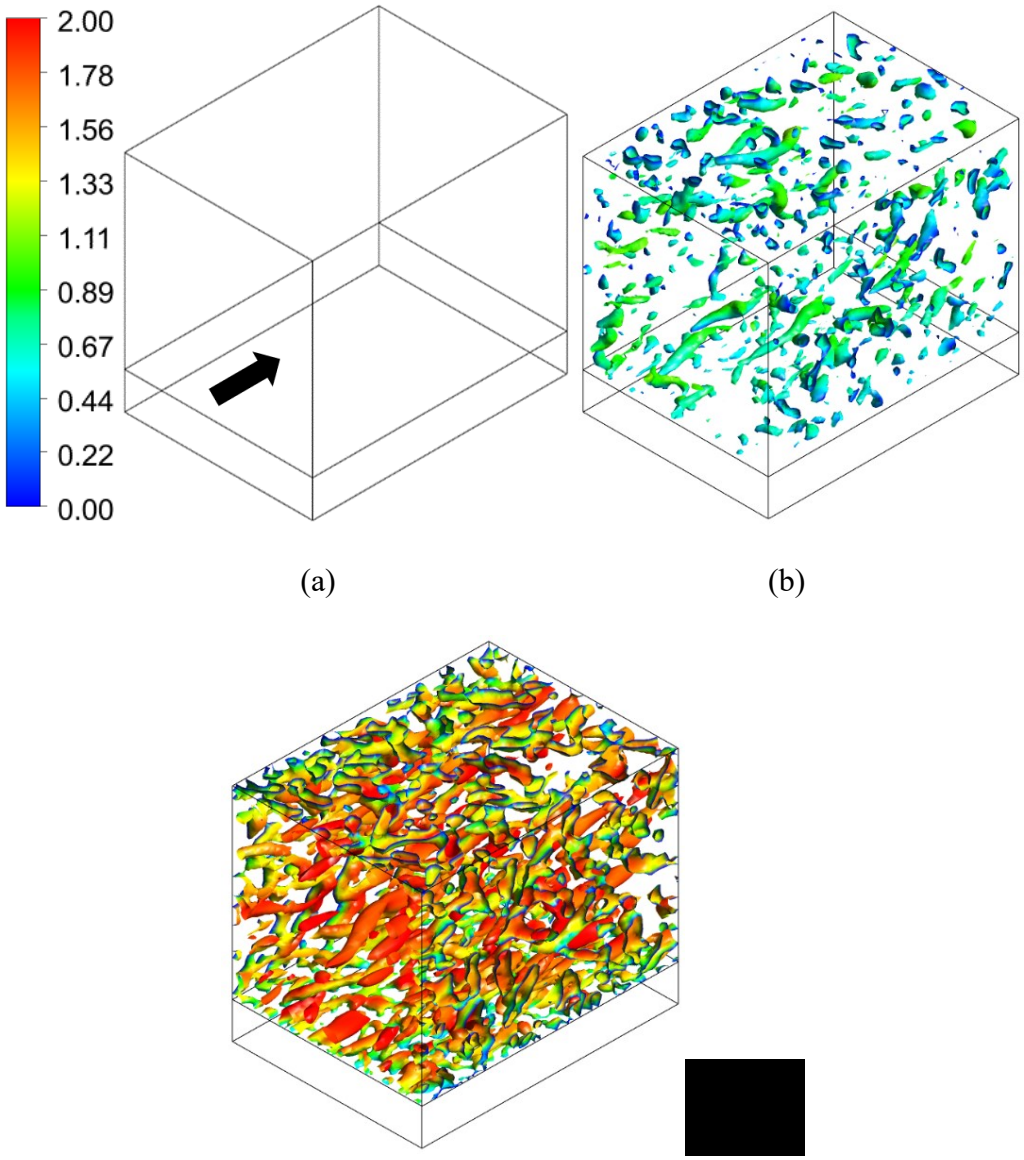

Figure 7.15: Q criterions (Q = 50000 s^{-2}) at 5.5 s in the smooth duct (a) case 1, (b) case 2, and (c) case 3

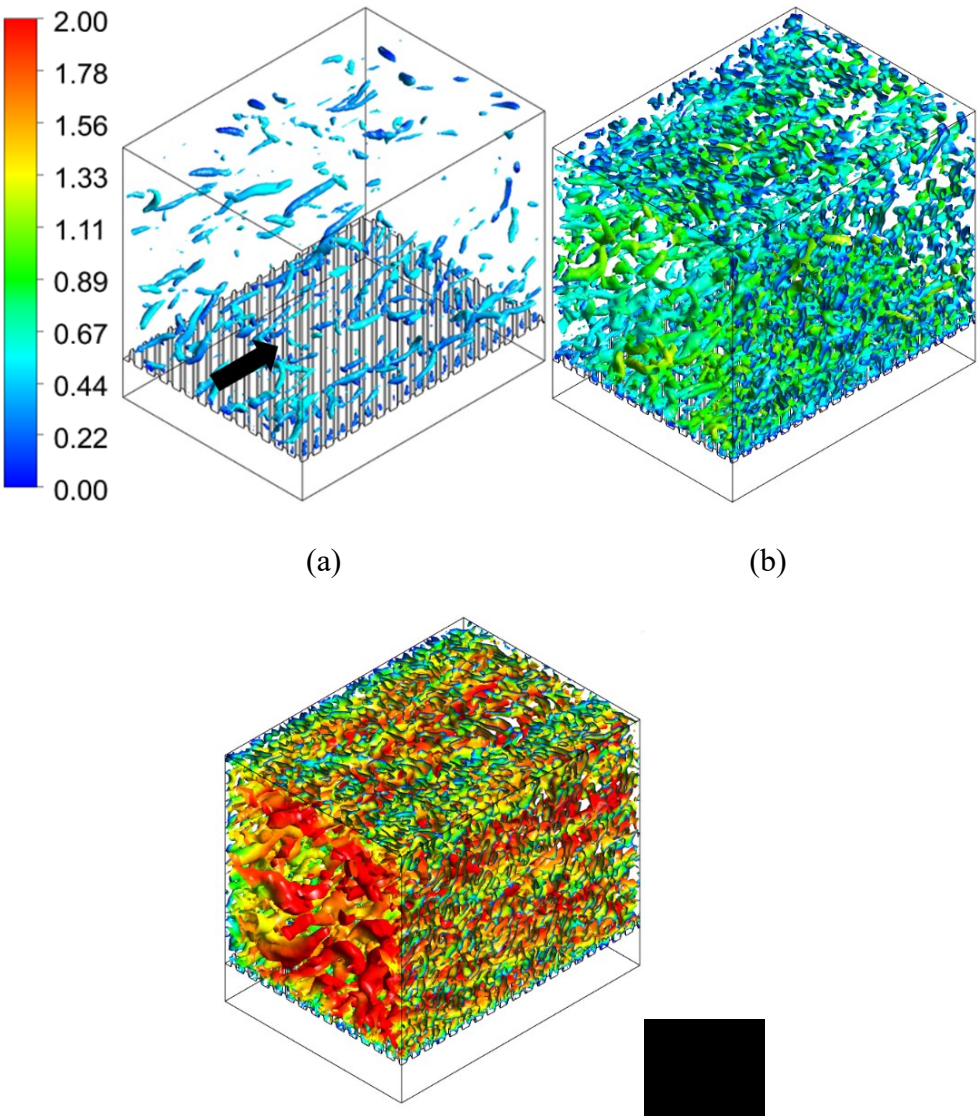

Figure 7.16: Q criterions (Q = 50000 s^{-2}) at 5.5 s in the micro-finned duct (a) case 1, (b) case 2, and (c) case 3

7.5. Conclusions

PIV technology and numerical simulations with LES were used to study the relationship between flow characteristics and heat transfer in a square duct with micro-fins. Good agreements

were found when the experimental results were compared to the numerical simulation results. The conclusions are presented as follows:

(1) Micro-fins affected the surrounding flow characteristics significantly. Furthermore, different regions of the micro-fins disturbed the *TKE* differently.

(2) The study proved the coherent structures had some relationship to heat transfer enhancement. In the future, it would be helpful if some formulas were mathematically generated to link the coherent structures with heat transfer.

(3) Micro-fins in the duct not only enhanced the area of the solid-fluid interface but also boosted the product of coherent structures. The coherent structures contributed to the fluid mixing. The fluid mixing was an effect to enhance communication among the different temperature layers, which led to increased *HTC*. The bonus effect of the micro-fins explained the first problem of why increases of heat transfer were normally larger than area increases in the micro-finned tubes.

(4) Reynolds numbers also affected the enhancement of heat transfer. Reynolds numbers predicted flow patterns in different fluid-flow situations. At a low Reynolds number, such as laminar and transition flow, some gaps of the micro-fins were not filled with swirls, which had a negative effect on the communication between zones 1 and 2. Less communication meant less heat transfer between zones 1 and 2. The effect answered the second problem of why internally micro-finned tubes usually have a lower heat-transfer-enhanced ratio at laminar and transition flow regions.

Chapter 8 - Conclusions and Future Work

In summary, the study validates turbulent coherent structures (TCS) play a dominate role for heat transfer enhancement. Chapter 1 introduces the history of internal micro-finned tubes. Correlations for heat transfer coefficient and friction factor are developed based on experimental and numerical results. Chapter 2 and Chapter 3 describe experimental set-up and numerical simulations for the study, respectively. Large eddy simulations (LES) were applied to the numerical simulations to study the process of TCS. LES is very sensitive with the boundary conditions. A new method of generating boundary conditions by incorporating PIV data was addressed in Chapter 4. Chapter 5 discusses the efficiency of parallel processing in ANSYS Fluent. The goal of Chapter 6 is to demonstrate that an accurate simulation of the smooth tube can be obtained as a benchmark for the start of the micro-fin tubes. Finally, Chapter 7 addresses the contribution of turbulent coherent structures (TCS) for the heat transfer enhancement in micro-finned tubes.

In the future, through analytical and experimental techniques, the following scientific questions centering around TCS and its contributions to heat transfer in the turbulent boundary layer will be addressed and answered: (1) How does TCS form? (2) How does TCS grow or decay? (3) Does TCS have proportionally larger effect on heat transfer than on apparent wall shear stress?

Reference

[1] E. A. McCullough, S. Eckels, and M. Schlabach, "Evaluation of Personal Cooling Systems for Soldiers Using a Sweating Manikin," 2008.

[2] E. A. McCullough and S. Eckels, "Evaluation of personal cooling systems for soldiers," in *Proceedings 13th International Conference on Environmental Ergonomics*, 2009, pp. 200–204.

[3] E. A. McCullough, S. Eckels, and C. Harms, "Determining temperature ratings for children's cold weather clothing," *Appl. Ergon.*, vol. 40, no. 5, pp. 870–877, 2009.

[4] M. Schlabach, E. A. McCullough, and S. J. Eckels, "Determining temperature ratings for children's sleeping bags," *Int. J. Ind. Ergon.*, vol. 65, pp. 153–160, 2018.

[5] J. Elson and S. Eckels, "An objective method for screening and selecting personal cooling systems based on cooling properties," *Appl. Ergon.*, vol. 48, pp. 33–41, 2015.

[6] J. Elson and S. Eckels, "Contribution of wetted clothing to body energy exchange and heat stress," *J. Therm. Biol.*, vol. 78, pp. 343–351, 2018.

[7] J. C. Elson, E. A. McCullough, and S. Eckels, "Evaluation of personal cooling systems for military use," *Ed. James Cotter Samuel JE Lucas Toby Mündel*, p. 280, 2013.

[8] W. Asher, "Fluid dynamics of cavitating sonic two-phase flow in a converging-diverging nozzle," PhD Thesis, Kansas State University, 2014.

[9] W. Asher and S. J. Eckels, "Characterization of liquid refrigerant R-123 flow emerging from a flooded evaporator tube bundle," *Sci. Technol. Built Environ.*, vol. 24, no. 9, pp. 1026–1038, 2018.

[10] W. E. Asher and S. J. Eckels, “Analysis of cavitating high speed liquid flow through a converging-diverging nozzle,” in *ASME 2015 International Mechanical Engineering Congress and Exposition*, 2015, p. V07AT09A006–V07AT09A006.

[11] E. Gorgy, “Experimental evaluation of heat transfer impacts of tube pitch on highly enhanced surface tube bundle.,” PhD Thesis, Kansas State University, 2011.

[12] E. Gorgy and S. Eckels, “Average heat transfer coefficient for pool boiling of R-134a and R-123 on smooth and enhanced tubes (RP-1316),” *HVACR Res.*, vol. 16, no. 5, pp. 657–676, 2010.

[13] E. Gorgy and S. Eckels, “Local heat transfer coefficient for pool boiling of R-134a and R-123 on smooth and enhanced tubes,” *Int. J. Heat Mass Transf.*, vol. 55, no. 11–12, pp. 3021–3028, 2012.

[14] E. Gorgy and S. Eckels, “Convective boiling of R-134a and R-123 on an enhanced tube bundle with standard pitch, RP-1316,” *HVACR Res.*, vol. 19, no. 2, pp. 193–206, 2013.

[15] E. Gorgy and S. Eckels, “Convective boiling of R-134a on enhanced-tube bundles,” *Int. J. Refrig.*, vol. 68, pp. 145–160, 2016.

[16] E. Gorgy and S. Eckels, “Convective boiling of R-123 on enhanced-tube bundles,” *Int. J. Heat Mass Transf.*, vol. 134, pp. 752–767, 2019.

[17] G. W. Mann, G. R. Madamadakala, and S. J. Eckels, “Heat transfer characteristics of R-134a in a converging-Diverging nozzle,” *Int. J. Heat Fluid Flow*, vol. 62, pp. 464–473, 2016.

[18] P. Li, S. J. Eckels, G. W. Mann, and N. Zhang, “A Method of Measuring Turbulent Flow Structures With Particle Image Velocimetry and Incorporating Into Boundary Conditions of Large Eddy Simulations,” *J. Fluids Eng.*, vol. 140, no. 7, p. 071401, 2018.

[19] P. Li, S. J. Eckels, G. W. Mann, and N. Zhang, "Experimental measurements in near-wall regions by particle image velocimetry (PIV)," in *ASME 2014 4th Joint US-European Fluids Engineering Division Summer Meeting collocated with the ASME 2014 12th International Conference on Nanochannels, Microchannels, and Minichannels*, 2014, p. V01DT40A004–V01DT40A004.

[20] P. Li, M. Campbell, N. Zhang, and S. J. Eckels, "Relationship between turbulent structures and heat transfer in microfin enhanced surfaces using large eddy simulations and particle image velocimetry," *Int. J. Heat Mass Transf.*, vol. 136, pp. 1282–1298, Jun. 2019.

[21] G. W. Mann and S. Eckels, "Multi-objective heat transfer optimization of 2D helical micro-fins using NSGA-II," *Int. J. Heat Mass Transf.*, vol. 132, pp. 1250–1261, 2019.

[22] W.-T. Ji, A. M. Jacobi, Y.-L. He, and W.-Q. Tao, "Summary and evaluation on single-phase heat transfer enhancement techniques of liquid laminar and turbulent pipe flow," *Int. J. Heat Mass Transf.*, vol. 88, pp. 735–754, 2015.

[23] M. K. Jensen and A. Vlakancic, "Technical Note Experimental investigation of turbulent heat transfer and fluid flow in internally finned tubes," *Int. J. Heat Mass Transf.*, vol. 42, no. 7, pp. 1343–1351, Apr. 1999.

[24] G. J. Zdaniuk, L. M. Chamra, and P. J. Mago, "Experimental determination of heat transfer and friction in helically-finned tubes," *Exp. Therm. Fluid Sci.*, vol. 32, no. 3, pp. 761–775, Jan. 2008.

[25] G. Tanda, "Effect of rib spacing on heat transfer and friction in a rectangular channel with 45 angled rib turbulators on one/two walls," *Int. J. Heat Mass Transf.*, vol. 54, no. 5–6, pp. 1081–1090, 2011.

[26] J. Nikuradse, *Laws of flow in rough pipes*. National Advisory Committee for Aeronautics Washington, 1950.

[27] D. F. Dipprey and R. H. Sabersky, "Heat and momentum transfer in smooth and rough tubes at various Prandtl numbers," *Int. J. Heat Mass Transf.*, vol. 6, no. 5, pp. 329–353, 1963.

[28] R. L. Webb, E. R. G. Eckert, and Rj. Goldstein, "Heat transfer and friction in tubes with repeated-rib roughness," *Int. J. Heat Mass Transf.*, vol. 14, no. 4, pp. 601–617, 1971.

[29] J.-C. Han, L. R. Glicksman, and W. M. Rohsenow, "An investigation of heat transfer and friction for rib-roughened surfaces," *Int. J. Heat Mass Transf.*, vol. 21, no. 8, pp. 1143–1156, 1978.

[30] D. L. Gee and R. L. Webb, "Forced convection heat transfer in helically rib-roughened tubes," *Int. J. Heat Mass Transf.*, vol. 23, no. 8, pp. 1127–1136, 1980.

[31] C. C. Wang, C. B. Chiou, and D. C. Lu, "Single-phase heat transfer and flow friction correlations for microfin tubes," *Int. J. Heat Fluid Flow*, vol. 17, no. 5, pp. 500–508, 1996.

[32] T. C. Carnavos, "Heat transfer performance of internally finned tubes in turbulent flow," *Heat Transf. Eng.*, vol. 1, no. 4, pp. 32–37, 1980.

[33] T. S. Ravigururajan and A. E. Bergles, "Development and verification of general correlations for pressure drop and heat transfer in single-phase turbulent flow in enhanced tubes," *Exp. Therm. Fluid Sci.*, vol. 13, no. 1, pp. 55–70, 1996.

[34] R. L. Webb, R. Narayanamurthy, and P. Thors, "Heat transfer and friction characteristics of internal helical-rib roughness," *J. Heat Transf.*, vol. 122, no. 1, pp. 134–142, 2000.

[35] H. S. Wang and J. W. Rose, "Prediction of effective friction factors for single-phase flow in horizontal microfin tubes," *Int. J. Refrig.*, vol. 27, no. 8, pp. 904–913, 2004.

[36] W.-T. Ji, D.-C. Zhang, Y.-L. He, and W.-Q. Tao, “Prediction of fully developed turbulent heat transfer of internal helically ribbed tubes–An extension of Gnielinski equation,” *Int. J. Heat Mass Transf.*, vol. 55, no. 4, pp. 1375–1384, 2012.

[37] B. A. Kader and A. M. Yaglom, “Turbulent heat and mass transfer from a wall with parallel roughness ridges,” *Int. J. Heat Mass Transf.*, vol. 20, no. 4, pp. 345–357, 1977.

[38] F. P. Incropera, A. S. Lavine, T. L. Bergman, and D. P. DeWitt, *Fundamentals of heat and mass transfer*. Wiley, 2007.

[39] R. B. Bird, E. N. Lightfoot, and W. E. Stewart, *Transport phenomena*, Rev. 2nd ed. New York ; Wiley, 2007.

[40] L. J. Brognaux, R. L. Webb, L. M. Chamra, and B. Y. Chung, “Single-phase heat transfer in micro-fin tubes,” *Int. J. Heat Mass Transf.*, vol. 40, no. 18, pp. 4345–4357, 1997.

[41] J. B. Copetti, M. H. Macagnan, D. de Souza, and R. D. C. Oliveski, “Experiments with micro-fin tube in single phase,” *Int. J. Refrig.*, vol. 27, no. 8, pp. 876–883, 2004.

[42] D. H. Han and K.-J. Lee, “Single-phase heat transfer and flow characteristics of micro-fin tubes,” *Appl. Therm. Eng.*, vol. 25, no. 11–12, pp. 1657–1669, 2005.

[43] P. Naphon and P. Sriromruln, “Single-phase heat transfer and pressure drop in the micro-fin tubes with coiled wire insert,” *Int. Commun. Heat Mass Transf.*, vol. 33, no. 2, pp. 176–183, 2006.

[44] M. Siddique and M. Alhazmy, “Experimental study of turbulent single-phase flow and heat transfer inside a micro-finned tube,” *Int. J. Refrig.*, vol. 31, no. 2, pp. 234–241, 2008.

[45] S. V. Patankar, M. Ivanovic, and E. M. Sparrow, “Analysis of turbulent flow and heat transfer in internally finned tubes and annuli,” *J. Heat Transf.*, vol. 101, no. 1, pp. 29–37, 1979.

[46] X. Liu and M. K. Jensen, “Numerical investigation of turbulent flow and heat transfer in internally finned tubes,” *J. Enhanc. Heat Transf.*, vol. 6, no. 2–4, 1999.

[47] D. N. Ryu, D. H. Choi, and V. C. Patel, “Analysis of turbulent flow in channels roughened by two-dimensional ribs and three-dimensional blocks. Part I: Resistance,” *Int. J. Heat Fluid Flow*, vol. 28, no. 5, pp. 1098–1111, 2007.

[48] D. N. Ryu, D. H. Choi, and V. C. Patel, “Analysis of turbulent flow in channels roughened by two-dimensional ribs and three-dimensional blocks. Part II: Heat transfer,” *Int. J. Heat Fluid Flow*, vol. 28, no. 5, pp. 1112–1124, 2007.

[49] P. Dupuis, Y. Cormier, M. Fenech, A. Corbeil, and B. Jodoin, “Flow structure identification and analysis in fin arrays produced by cold spray additive manufacturing,” *Int. J. Heat Mass Transf.*, vol. 93, pp. 301–313, 2016.

[50] G. Xia, Z. Chen, L. Cheng, D. Ma, Y. Zhai, and Y. Yang, “Micro-PIV visualization and numerical simulation of flow and heat transfer in three micro pin-fin heat sinks,” *Int. J. Therm. Sci.*, vol. 119, pp. 9–23, 2017.

[51] R. S. Bhatia and R. L. Webb, “Numerical Study of Turbulent Flow and Heat Transfer in Micro-Fin Tubes–Part 1, Model Validation,” *J. Enhanc. Heat Transf.*, vol. 8, no. 5, 2001.

[52] R. S. Bhatia and R. L. Webb, “Numerical Study of Turbulent Flow and Heat Transfer in Micro-Fin Tubes–Part 2, Parametric Study,” *J. Enhanc. Heat Transf.*, vol. 8, no. 5, 2001.

[53] P. Jasiński, “Numerical study of friction factor and heat transfer characteristics for single-phase turbulent flow in tubes with helical micro-fins,” *Arch. Mech. Eng.*, vol. 59, no. 4, pp. 469–485, 2012.

[54] R. Campet, M. Zhu, E. Riber, B. Cuenot, and M. Nemri, “Large Eddy Simulation of a single-started helically ribbed tube with heat transfer,” *Int. J. Heat Mass Transf.*, vol. 132, pp. 961–969, 2019.

[55] “ANSYS FLUENT 12.0 User’s Guide.” [Online]. Available: http://www.afs.enea.it/project/neptunius/docs/fluent/html/ug/main_pre.htm. [Accessed: 20-Feb-2019].

[56] J. Cui, V. C. Patel, and C.-L. Lin, “Large-eddy simulation of turbulent flow in a channel with rib roughness,” *Int. J. Heat Fluid Flow*, vol. 24, no. 3, pp. 372–388, 2003.

[57] Y. Miyake, K. Tsujimoto, and N. Nagai, “Numerical simulation of channel flow with a rib-roughened wall*,” *J. Turbul.*, vol. 3, no. 35, pp. 1–17, 2002.

[58] T. Ikeda and P. A. Durbin, “Direct simulations of a rough-wall channel flow,” *J. Fluid Mech.*, vol. 571, pp. 235–263, 2007.

[59] D. Kalyanmoy, A. Pratap, S. Agarwal, and T. Meyarivan, “A fast and elitist multiobjective genetic algorithm: NSGA-II,” *IEEE Trans. Evol. Comput.*, vol. 6, no. 2, pp. 182–197, 2002.

[60] E. Zitzler, M. Laumanns, and L. Thiele, “Improving the strength Pareto evolutionary algorithm,” *EUROGEN 2001 Evol. Methods Des. Optim. Control Appl. Ind. Probl.*, pp. 95–100, 2000.

[61] S. Fettaka, J. Thibault, and Y. Gupta, “Design of shell-and-tube heat exchangers using multiobjective optimization,” *Int. J. Heat Mass Transf.*, vol. 60, pp. 343–354, 2013.

[62] A. Agarwal and S. K. Gupta, “Jumping gene adaptations of NSGA-II and their use in the multi-objective optimal design of shell and tube heat exchangers,” *Chem. Eng. Res. Des.*, vol. 86, no. 2, pp. 123–139, 2008.

[63] M. A. Elsays, M. N. Aly, and A. A. Badawi, “Design optimization of shell-and-tube heat exchangers using single objective and multiobjective particle swarm optimization,” *Kerntechnik*, vol. 75, no. 1–2, pp. 38–46, 2010.

[64] H. Hajabdollahi, P. Ahmadi, and I. Dincer, “Exergetic optimization of shell-and-tube heat exchangers using NSGA-II,” *Heat Transf. Eng.*, vol. 33, no. 7, pp. 618–628, 2012.

[65] S. Sanaye and H. Hajabdollahi, “Multi-objective optimization of shell and tube heat exchangers,” *Appl. Therm. Eng.*, vol. 30, no. 14–15, pp. 1937–1945, 2010.

[66] H. Hajabdollahi, M. Tahani, and M. S. Fard, “CFD modeling and multi-objective optimization of compact heat exchanger using CAN method,” *Appl. Therm. Eng.*, vol. 31, no. 14–15, pp. 2597–2604, 2011.

[67] P. Ahmadi, H. Hajabdollahi, and I. Dincer, “Cost and entropy generation minimization of a cross-flow plate fin heat exchanger using multi-objective genetic algorithm,” *J. Heat Transf.*, vol. 133, no. 2, p. 021801, 2011.

[68] S. Sanaye and H. Hajabdollahi, “Thermal-economic multi-objective optimization of plate fin heat exchanger using genetic algorithm,” *Appl. Energy*, vol. 87, no. 6, pp. 1893–1902, 2010.

[69] D. Juan and Q. Z. Qin, “Multi-objective optimization of a plain fin-and-tube heat exchanger using genetic algorithm,” *Therm. Eng.*, vol. 61, no. 4, pp. 309–317, 2014.

[70] W. Han, K. Saleh, V. Aute, G. Ding, Y. Hwang, and R. Radermacher, “Numerical simulation and optimization of single-phase turbulent flow in chevron-type plate heat exchanger with sinusoidal corrugations,” *HVACR Res.*, vol. 17, no. 2, pp. 186–197, 2011.

[71] H. Lee, K. Saleh, Y. Hwang, and R. Radermacher, “Optimization of novel heat exchanger design for the application to low temperature lift heat pump,” *Energy*, vol. 42, no. 1, pp. 204–212, 2012.

[72] J. Lee and K.-S. Lee, “Correlations and shape optimization in a channel with aligned dimples and protrusions,” *Int. J. Heat Mass Transf.*, vol. 64, pp. 444–451, 2013.

[73] A. R. Betz and D. Attinger, “Can segmented flow enhance heat transfer in microchannel heat sinks?,” *Int. J. Heat Mass Transf.*, vol. 53, no. 19–20, pp. 3683–3691, 2010.

[74] C.-Y. Yang, C.-W. Chen, T.-Y. Lin, and S. G. Kandlikar, “Heat transfer and friction characteristics of air flow in microtubes,” *Exp. Therm. Fluid Sci.*, vol. 37, pp. 12–18, 2012.

[75] P. Li and S. J. Eckels, “Measurements and Numerical Simulations of Heat Transfer and Pressure Drop in a Duct With Smooth Walls,” presented at the ASME 2017 International Mechanical Engineering Congress and Exposition, 2017, p. V008T10A004-V008T10A004.

[76] Z. Dai, D. F. Fletcher, and B. S. Haynes, “Impact of tortuous geometry on laminar flow heat transfer in microchannels,” *Int. J. Heat Mass Transf.*, vol. 83, pp. 382–398, 2015.

[77] Y. Zhai, G. Xia, Z. Chen, and Z. Li, “Micro-PIV study of flow and the formation of vortex in micro heat sinks with cavities and ribs,” *Int. J. Heat Mass Transf.*, vol. 98, pp. 380–389, Jul. 2016.

[78] C. D. Meinhart, S. T. Wereley, and J. G. Santiago, “PIV measurements of a microchannel flow,” *Exp. Fluids*, vol. 27, no. 5, pp. 414–419, Oct. 1999.

[79] G. W. Mann and S. J. Eckels, “Focal plane model for flat refractive geometry,” *J. Eur. Opt. Soc.-Rapid Publ.*, vol. 13, no. 1, p. 39, 2017.

[80] “Insight 4G Software Manual, Revision B.” TSI, Inc., 2014.

[81] "ITTC–Recommended Procedures and Guidelines, Uncertainty analysis for Particle Imaging Velocimetry (PIV)." The Visualization Society of Japan (VSJ), 2011.

[82] N. Zhang, D. Kee, and P. Li, "Investigation of the impacts of Gulf sediments on Calcasieu Ship Channel and surrounding water systems," *Comput. Fluids*, vol. 77, pp. 125–133, Apr. 2013.

[83] N. Zhang, P. Li, and A. He, "Coupling of One-Dimensional and Two-Dimensional Hydrodynamic Models Using an Immersed-Boundary Method," *J. Fluids Eng.*, vol. 136, no. 4, p. 040907, Apr. 2014.

[84] "A blind detector for Rayleigh flat-fading channels with non-Gaussian interference via the particle learning algorithm - ScienceDirect." [Online]. Available: https://www.sciencedirect.com/science/article/pii/S143484111300174X. [Accessed: 22-Feb-2019].

[85] "A Blind Receiver with Multiple Antennas in Impulsive Noise Modeled as the Sub-Gaussian Distribution via the MCMC Algorithm - IEEE Journals & Magazine." [Online]. Available: https://ieeexplore.ieee.org/abstract/document/6472312. [Accessed: 22-Feb-2019].

[86] N. Zhang, J. Bolton, and P. Li, "A 1-D and 2-D Coupled Sediment Transport Model Using the Immersed-Boundary Method," presented at the ASME 2013 Fluids Engineering Division Summer Meeting, 2013, p. V01AT08A001-V01AT08A001.

[87] N. Zhang, Z. Li, A. Davis, P. Li, and A. He, "Numerical and Experimental Investigation of Wave-Structure Interactions on Coastal Highways and Levees," presented at the ASME 2012 Fluids Engineering Division Summer Meeting collocated with the ASME 2012 Heat

Transfer Summer Conference and the ASME 2012 10th International Conference on Nanochannels, Microchannels, and Minichannels, 2012, pp. 197–202.

[88] N. Zhang, P. Li, E. Gonzalez Pons, J. Kurt, and M. C. Silva, "Numerical Analysis of Erosion and Sediment Control Using Lake-Shore Extensions in Lake Charles," pp. 863–869, Jan. 2011.

[89] J. Pedlosky, *Geophysical fluid dynamics*. Springer Science & Business Media, 2013.

[90] C. K. Batchelor and G. K. Batchelor, *An introduction to fluid dynamics*. Cambridge university press, 1967.

[91] C. G. Speziale, S. Sarkar, and T. B. Gatski, "Modelling the pressure–strain correlation of turbulence: an invariant dynamical systems approach," *J. Fluid Mech.*, vol. 227, pp. 245–272, Jun. 1991.

[92] M. Germano, U. Piomelli, P. Moin, and W. H. Cabot, "A dynamic subgrid-scale eddy viscosity model," *Phys. Fluids Fluid Dyn.*, vol. 3, no. 7, pp. 1760–1765, Jul. 1991.

[93] M. L. Shur, P. R. Spalart, M. K. Strelets, and A. K. Travin, "A hybrid RANS-LES approach with delayed-DES and wall-modelled LES capabilities," *Int. J. Heat Fluid Flow*, vol. 29, no. 6, pp. 1638–1649, Dec. 2008.

[94] W.-W. Kim, S. Menon, W.-W. Kim, and S. Menon, "Application of the localized dynamic subgrid-scale model to turbulent wall-bounded flows," in *35th aerospace sciences meeting and exhibit*, 1997, p. 210.

[95] "Inlet conditions for large eddy simulation: A review - ScienceDirect." [Online]. Available: https://www.sciencedirect.com/science/article/pii/S0045793009001601. [Accessed: 22-Feb-2019].

[96] J.-L. Aider and A. Danet, “Large-eddy simulation study of upstream boundary conditions influence upon a backward-facing step flow,” *Comptes Rendus Mécanique*, vol. 334, no. 7, pp. 447–453, Jul. 2006.

[97] F. Mathey, D. Cokljat, J. P. Bertoglio, and E. Sergent, “Assessment of the vortex method for Large Eddy Simulation inlet conditions,” *Prog. Comput. Fluid Dyn. Int. J.*, vol. 6, no. 1/2/3, p. 58, 2006.

[98] S. Lee, S. K. Lele, and P. Moin, “Simulation of spatially evolving turbulence and the applicability of Taylor’s hypothesis in compressible flow,” *Phys. Fluids Fluid Dyn.*, vol. 4, no. 7, pp. 1521–1530, Jul. 1992.

[99] L. di Mare, M. Klein, W. P. Jones, and J. Janicka, “Synthetic turbulence inflow conditions for large-eddy simulation,” *Phys. Fluids*, vol. 18, no. 2, p. 025107, Feb. 2006.

[100] T. S. Lund, X. Wu, and K. D. Squires, “Generation of Turbulent Inflow Data for Spatially-Developing Boundary Layer Simulations,” *J. Comput. Phys.*, vol. 140, no. 2, pp. 233–258, Mar. 1998.

[101] M. H. Baba-Ahmadi and G. Tabor, “Inlet conditions for LES using mapping and feedback control,” *Comput. Fluids*, vol. 38, no. 6, pp. 1299–1311, Jun. 2009.

[102] C. D. Pierce and P. Moin, “Method for Generating Equilibrium Swirling Inflow Conditions,” *AIAA J.*, vol. 36, no. 7, pp. 1325–1327, 1998.

[103] F. Sbrizzai, R. Verzicco, and A. Soldati, “Turbulent Flow and Dispersion of Inertial Particles in a Confined Jet Issued by a Long Cylindrical Pipe,” *Flow Turbul. Combust.*, vol. 82, no. 1, pp. 1–23, Jan. 2009.

[104] D. Drikakis, “Advances in turbulent flow computations using high-resolution methods,” *Prog. Aerosp. Sci.*, vol. 39, no. 6, pp. 405–424, Aug. 2003.

[105] P. Li, “Hydrodynamics, sediment transport and erosion simulation in Calcasieu Lake and surrounding areas,” M. Engin., McNeese State University, 2012.

[106] P. Li, S. J. Eckels, N. Zhang, and G. W. Mann, “Effects of Parallel Processing on Large Eddy Simulations in ANSYS Fluent,” in *ASME 2016 Fluids Engineering Division Summer Meeting collocated with the ASME 2016 Heat Transfer Summer Conference and the ASME 2016 14th International Conference on Nanochannels, Microchannels, and Minichannels*, 2016, p. V01BT26A004–V01BT26A004.

[107] S. B. Pope and S. B. Pope, *Turbulent Flows*. Cambridge University Press, 2000.

[108] D. Xu and J. Chen, “Accurate estimate of turbulent dissipation rate using PIV data,” *Exp. Therm. Fluid Sci.*, vol. 44, pp. 662–672, Jan. 2013.

[109] K. R. Sreenivasan, “On the universality of the Kolmogorov constant,” *Phys. Fluids*, vol. 7, no. 11, pp. 2778–2784, Nov. 1995.

[110] E. Weher, “Edwards, Allen, L.: An introduction to linear regression and correlation. (A series of books in psychology.) W. H. Freeman and Comp., San Francisco 1976. 213 S., Tafelanh., s 7.00,” *Biom. J.*, vol. 19, no. 1, pp. 83–84, 1977.

[111] R. Courant, K. Friedrichs, and H. Lewy, “On the partial difference equations of mathematical physics,” *IBM J. Res. Dev.*, vol. 11, no. 2, pp. 215–234, 1967.

[112] “Parallel computing -- CFD-Wiki, the free CFD reference.” [Online]. Available: https://www.cfd-online.com/Wiki/Parallel_computing. [Accessed: 23-Feb-2019].

[113] A. G. Ranade, “Fluent parallel computation,” New Haven, CT (US); Yale Univ., Jan. 1989.

[114] S. Gavrilakis, “Numerical simulation of low-Reynolds-number turbulent flow through a straight square duct,” *J. Fluid Mech.*, vol. 244, pp. 101–129, Nov. 1992.

[115] P. Talukdar, C. R. Iskra, and C. J. Simonson, “Combined heat and mass transfer for laminar flow of moist air in a 3D rectangular duct: CFD simulation and validation with experimental data,” *Int. J. Heat Mass Transf.*, vol. 51, no. 11, pp. 3091–3102, Jun. 2008.

[116] J. Smagorinsky, “GENERAL CIRCULATION EXPERIMENTS WITH THE PRIMITIVE EQUATIONS: I. THE BASIC EXPERIMENT*,” *Mon. Weather Rev.*, vol. 91, no. 3, pp. 99–164, Mar. 1963.

[117] J. W. Deardorff, “A numerical study of three-dimensional turbulent channel flow at large Reynolds numbers,” *J. Fluid Mech.*, vol. 41, no. 2, pp. 453–480, Apr. 1970.

[118] “LARGE-EDDY SIMULATION OF TURBULENT COMBUSTION | Annual Review of Fluid Mechanics.” [Online]. Available: https://www.annualreviews.org/doi/full/10.1146/annurev.fluid.38.050304.092133. [Accessed: 23-Feb-2019].

[119] C. Wagner, T. Hüttl, and P. Sagaut, *Large-Eddy Simulation for Acoustics*. Cambridge University Press, 2007.

[120] P. P. Sullivan, J. C. McWilliams, and C.-H. Moeng, “A subgrid-scale model for large-eddy simulation of planetary boundary-layer flows,” *Bound.-Layer Meteorol.*, vol. 71, no. 3, pp. 247–276, Nov. 1994.

[121] W. D. Gropp, D. K. Kaushik, D. E. Keyes, and B. F. Smith, “High-performance parallel implicit CFD,” *Parallel Comput.*, vol. 27, no. 4, pp. 337–362, Mar. 2001.

[122] R. Hilbert, G. Janiga, R. Baron, and D. Thévenin, “Multi-objective shape optimization of a heat exchanger using parallel genetic algorithms,” *Int. J. Heat Mass Transf.*, vol. 49, no. 15–16, pp. 2567–2577, 2006.

[123] A. M. Oler and N. Zhang, “OpenFoam Simulations of Flow Over Flapping Wing Using Parallel Computing,” presented at the ASME/JSME/KSME 2015 Joint Fluids Engineering Conference, 2015, p. V001T29A001-V001T29A001.

[124] F. Nicoud and F. Ducros, “Subgrid-Scale Stress Modelling Based on the Square of the Velocity Gradient Tensor,” *Flow Turbul. Combust.*, vol. 62, no. 3, pp. 183–200, Sep. 1999.

[125] “Turbulence (McGraw-Hill series in mechanical engineering): J. O. Hinze: 9780070290372: Amazon.com: Books.” [Online]. Available: https://www.amazon.com/Turbulence-McGraw-Hill-mechanical-engineering-Hinze/dp/0070290377. [Accessed: 23-Feb-2019].

[126] “Heat Transfer (2nd Edition): A.F. Mills: 9780139476242: Amazon.com: Books.” [Online]. Available: https://www.amazon.com/Heat-Transfer-2nd-F-Mills/dp/0139476245. [Accessed: 24-Feb-2019].

[127] P. Coronel and K. P. Sandeep, “Heat transfer coefficient in helical heat exchangers under turbulent flow conditions,” *Int. J. Food Eng.*, vol. 4, no. 1, 2008.

[128] F. A. Hamad, F. Faraji, C. G. S. Santim, N. Basha, and Z. Ali, “Investigation of pressure drop in horizontal pipes with different diameters,” *Int. J. Multiph. Flow*, vol. 91, pp. 120–129, 2017.

[129] S. W. Chang, K. F. Chiang, and J. K. Kao, “Heat transfer and pressure drop in a square spiral channel roughened by in-line skew ribs,” *Int. J. Heat Mass Transf.*, vol. 54, no. 15–16, pp. 3167–3178, 2011.

[130] L. Redjem-Saad, M. Ould-Rouiss, and G. Lauriat, “Direct numerical simulation of turbulent heat transfer in pipe flows: Effect of Prandtl number,” *Int. J. Heat Fluid Flow*, vol. 28, no. 5, pp. 847–861, 2007.

[131] J. G. M. Eggels *et al.*, “Fully developed turbulent pipe flow: a comparison between direct numerical simulation and experiment,” *J. Fluid Mech.*, vol. 268, pp. 175–210, 1994.

[132] X. Liu and M. K. Jensen, “Geometry effects on turbulent flow and heat transfer in internally finned tubes,” *J. Heat Transf.*, vol. 123, no. 6, pp. 1035–1044, 2001.

[133] L. Micheli, K. S. Reddy, and T. K. Mallick, “General correlations among geometry, orientation and thermal performance of natural convective micro-finned heat sinks,” *Int. J. Heat Mass Transf.*, vol. 91, pp. 711–724, 2015.

[134] S. Pirbastami, S. F. Moujaes, and S. G. Mol, “Computational fluid dynamics simulation of heat enhancement in internally helical grooved tubes,” *Int. Commun. Heat Mass Transf.*, vol. 73, pp. 25–32, 2016.

[135] M. Dastmalchi, G. A. Sheikhzadeh, and A. Arefmanesh, “Optimization of micro-finned tubes in double pipe heat exchangers using particle swarm algorithm,” *Appl. Therm. Eng.*, vol. 119, pp. 1–9, 2017.

Appendix A - Processing Data/Matlab Code

Experimental and numerical data were output and processed in Matlab to obtain the flow characteristics, i.e. velocity magnitude, turbulent kinetic energy and turbulent dissipation rate.

Main Program

```
clc
format long;
viscosity=1.004*(10^-6);
Velocity=[];
Velocityx=[];
Velocityy=[];

for i=1:961

   N=0;

   for k=1:300

     counter= alldata(k) .CHC(i);

     if counter==1 | counter==4
       N=N+1;
       Uvalue=alldata(k) .U(i);
       Vvalue=alldata(k) .V(i);
       Velocitymag=sqrt(Uvalue^2+Vvalue^2);
       Velocity(k,1)=Velocitymag;
       Velocityx(k,1)=Uvalue;
       Velocityy(k,1)=Vvalue;
     else
       N=N;
       Velocitymag=0;
       Velocity(k,1)=Velocitymag;
       Velocityx(k,1)=0;
       Velocityy(k,1)=0;
     end

   end

   CounterN(i,1)=N;

   if N==0
     Averagemag(i)= 0;
     Averagemagx(i)=0;
     Averagemagy(i)=0;
   else
```

```
    Averagemag(i)= (sum (Velocity)) / (N);
    Averagemagx(i)=(sum (Velocityx)) / (N);
    Averagemagy(i)=(sum (Velocityy)) / (N);
  end

end

for i=1:961

  M=0;

  for k=1:300

   counter= alldata(k) .CHC(i);

   if counter==1 | counter==4
      M=M+1;
      Uvalue=alldata(k) .U(i);
      Vvalue=alldata(k) .V(i);
      Rooterrorx(k,1)= (Averagemagx(i)-Uvalue)^2;
      Rooterrory(k,1)= (Averagemagy(i)-Vvalue)^2;
   else
      M=M;
      Rooterrorx(k,1)=0;
      Rooterrory(k,1)=0;
   end

  end

  if M==0
     Kinetic(i)=0;
  else
     Kinetic(i)= (1/2)* ( sum(Rooterrorx)/M + sum(Rooterrory)/M + sum(Rooterrory)/M);
     % Assume that V fluctuation = W fluctuation
  end

end

dx=0.00009344;
dy=0.00009344;
% 1 is v and y; 2 is u and x
for i=1:800

  P=0;
  ii=i+1;
  iii=i+31;
```

```
    for k=1:300

     counter1= alldata(k) .CHC(i);
     counter2= alldata(k) .CHC (ii);
     counter3= alldata(k) .CHC (iii);

     if (counter1==1 | counter1==4) & (counter2==1 | counter2==4) & (counter3==1 |
counter3==4)
        P=P+1;
        Uvalue=alldata(k) .U(i);
        Vvalue=alldata(k) .V(i);
        UUvalue=alldata(k) .U(ii);
        VVvalue=alldata(k) .V(ii);
        UUUvalue=alldata(k) .U(iii);
        VVVvalue=alldata(k) .V(iii);
        delta1y(k,1)=Averagemagy(i)-Vvalue;
        delta3y(k,1)=Averagemagy(iii)-VVVvalue;
        delta2y(k,1)=Averagemagy(ii)-VVvalue;
        delta1x(k,1)=Averagemagx(i)-Uvalue;
        delta2x(k,1)=Averagemagx(iii)-UUUvalue;
        Fluctuation11sq(k,1)= (( delta1y(k,1)-delta3y(k,1) )/dy)^2;
        Fluctuation12(k,1)= ( delta1y(k,1)-delta2y(k,1) )/dx;
        Fluctuation12sq(k,1)= (( delta1y(k,1)-delta2y(k,1) )/dx)^2;
        Fluctuation21(k,1)= ( delta1x(k,1)-delta2x(k,1) )/dy;
     else
        P=P;
        Fluctuation11sq(k,1)=0;
        Fluctuation12(k,1)=0;
        Fluctuation12sq(k,1)=0;
        Fluctuation21(k,1)=0;
     end

    end

    CounterP(i,1)=P;

    if P==0
       Dissipation(i)=0;
    else
       Dissipation(i)= 6*viscosity* (sum(Fluctuation11sq)/P + ...
                                sum(Fluctuation12sq)/P + ...
                                   sum(abs(Fluctuation12.*Fluctuation21))/P );
    end

end
```

```
NewVelocity=Averagemag';
NewVelocityx=Averagemagx';
NewVelocityy=Averagemagy';
NewKinetic=Kinetic';
NewDissipation=Dissipation';

save export_Velocity_Mag03.txt NewVelocity -ascii
save export_Velocity_u03.txt NewVelocityx -ascii
save export_Velocity_v03.txt NewVelocityy -ascii
save export_Kinetic03.txt NewKinetic -ascii
save export_Dissipation03.txt NewDissipation -ascii
save CounterN03.txt CounterN -ascii
save CounterP03.txt CounterP –asci
```

Function for Reading Data

```
function
[TITLECExperiments102015_03_16_VelocityMeasurementTest_window_an,Ymm,Ums,Vms,C
HC,PeakToNoisePeak,DATASETAUXDATAApplicationPIVDATASETAUXDATASourceIma
geWidth2048D,I31,J31,FPOINT] = importfile2(filename, startRow, endRow)
%IMPORTFILE2 Import numeric data from a text file as column vectors.
%
[TITLECEXPERIMENTS102015_03_16_VELOCITYMEASUREMENTTEST_WINDOW_AN
,YMM,UMS,VMS,CHC,PEAKTONOISEPEAK,DATASETAUXDATAAPPLICATIONPIVD
ATASETAUXDATASOURCEIMAGEWIDTH2048D,I31,J31,FPOINT]
%   = IMPORTFILE2(FILENAME) Reads data from text file FILENAME for the
%   default selection.
%
%
[TITLECEXPERIMENTS102015_03_16_VELOCITYMEASUREMENTTEST_WINDOW_AN
,YMM,UMS,VMS,CHC,PEAKTONOISEPEAK,DATASETAUXDATAAPPLICATIONPIVD
ATASETAUXDATASOURCEIMAGEWIDTH2048D,I31,J31,FPOINT]
%   = IMPORTFILE2(FILENAME, STARTROW, ENDROW) Reads data from rows
STARTROW
%   through ENDROW of text file FILENAME.
%
% Example:
%
[TITLECExperiments102015_03_16_VelocityMeasurementTest_window_an,Ymm,Ums,Vms,C
HC,PeakToNoisePeak,DATASETAUXDATAApplicationPIVDATASETAUXDATASourceIma
geWidth2048D,I31,J31,FPOINT]
%   =
%   importfile2('Test_window_and_particle_density000000.T000.D000.P000.H000.L.vec',2,
%   962);
%
```

```
%    See also TEXTSCAN.

% Auto-generated by MATLAB on 2015/03/19 20:53:17

%% Initialize variables.
delimiter = ',';
if nargin<=2
   startRow = 2;
   endRow = inf;
end

%% Format string for each line of text:
%   column1: double (%f)
%   column2: double (%f)
%   column3: double (%f)
%   column4: double (%f)
%   column5: double (%f)
%   column6: double (%f)
%   column7: text (%s)
%   column8: text (%s)
%   column9: text (%s)
%   column10: text (%s)
% For more information, see the TEXTSCAN documentation.
formatSpec = '%f%f%f%f%f%f%s%s%s%s%[^\n\r]';

%% Open the text file.
fileID = fopen(filename,'r');

%% Read columns of data according to format string.
% This call is based on the structure of the file used to generate this
% code. If an error occurs for a different file, try regenerating the code
% from the Import Tool.
dataArray = textscan(fileID, formatSpec, endRow(1)-startRow(1)+1, 'Delimiter', delimiter,
'HeaderLines', startRow(1)-1, 'ReturnOnError', false);
for block=2:length(startRow)
   frewind(fileID);
   dataArrayBlock = textscan(fileID, formatSpec, endRow(block)-startRow(block)+1,
'Delimiter', delimiter, 'HeaderLines', startRow(block)-1, 'ReturnOnError', false);
   for col=1:length(dataArray)
      dataArray{col} = [dataArray{col};dataArrayBlock{col}];
   end
end

%% Close the text file.
fclose(fileID);
```

```
%% Post processing for unimportable data.
% No unimportable data rules were applied during the import, so no post
% processing code is included. To generate code which works for
% unimportable data, select unimportable cells in a file and regenerate the
% script.

%% Allocate imported array to column variable names
TITLECExperiments102015_03_16_VelocityMeasurementTest_window_an = dataArray{:, 1};
Ymm = dataArray{:, 2};
Ums = dataArray{:, 3};
Vms = dataArray{:, 4};
CHC = dataArray{:, 5};
PeakToNoisePeak = dataArray{:, 6};
DATASETAUXDATAApplicationPIVDATASETAUXDATASourceImageWidth2048D =
dataArray{:, 7};
I31 = dataArray{:, 8};
J31 = dataArray{:, 9};
FPOINT = dataArray{:, 10};
```

Appendix B – Autocorrelation Check for PIV Data/Matlab Code

To check the autocorrelation for PIV data, the Matlab code as follow was used. The range of correlation coefficient is from -1 to 1. That correlation coefficient is close to 1 means that the time series is statistically dependent. If the correlation coefficient is close to 0, the time series is statistically independent.

Main Program

```
clc
format long
filename = 'V_1_0_m_s_data_file.txt';
A = importdata(filename);

N=41263;
Asum1=zeros(1,100);
Aaver1=zeros(1,100);
diffA1=zeros(41262,100);
Asum2=zeros(1,100);
Aaver2=zeros(1,100);
diffA2=zeros(41262,100);
diffA1TdiffA2=zeros(41262,100);
SumDiffA1TdiffA2=zeros(1,100);
SquareDiffA1=zeros(1,100);
RootDiffA1=zeros(1,100);
SquareDiffA2=zeros(1,100);
RootDiffA2=zeros(1,100);
Correlation=zeros(1,100);

for j=1:100
   for i=1:N-138
      Asum1(1,j)=Asum1(1,j)+A(i,j);
   end
      Aaver1(1,j)=Asum1(1,j)/(N-138);
end

for j=1:100
   for i=139:N
      Asum2(1,j)=Asum2(1,j)+A(i,j);
   end
      Aaver2(1,j)=Asum2(1,j)/(N-138);
end
```

```
for j=1:100
   for i=1:N-138
      diffA1(i,j)=A(i,j)-Aaver1(1,j);
   end
end

for j=1:100
   for i=1:N-138
      diffA2(i,j)=A(i+1,j)-Aaver2(1,j);
   end
end

for j=1:100
   for i=1:N-138
      diffA1TdiffA2(i,j)=diffA1(i,j)*diffA2(i,j);
   end
end

for j=1:100
   for i=1:N-138
     SumDiffA1TdiffA2(1,j)= SumDiffA1TdiffA2(1,j)+ diffA1TdiffA2(i,j);
   end
end

for j=1:100
   for i=1:N-138
      SquareDiffA1(1,j)=SquareDiffA1(1,j)+(diffA1(i,j))^2;
   end
   RootDiffA1(1,j)=(SquareDiffA1(1,j))^0.5;
end

for j=1:100
   for i=1:N-138
     SquareDiffA2(1,j)=SquareDiffA2(1,j)+ (diffA2(i,j))^2;
   end
   RootDiffA2(1,j)=(SquareDiffA2(1,j))^0.5;
end

for j=1:100
   Correlation(1,j)=SumDiffA1TdiffA2(1,j)/(RootDiffA1(1,j)*RootDiffA2(1,j));
end
```

Appendix C – Setup in ANSYS Fluent

Numerical simulations were conducted in ANSYS Fluent. This section shows the setup in Fluent.

General

We setup solver type, velocity formulation, time type and gravity in this panel. The numerical simulations were pressure-based. The velocity formulation is absolute. The gravitational acceleration was 9.81 m/s^2.

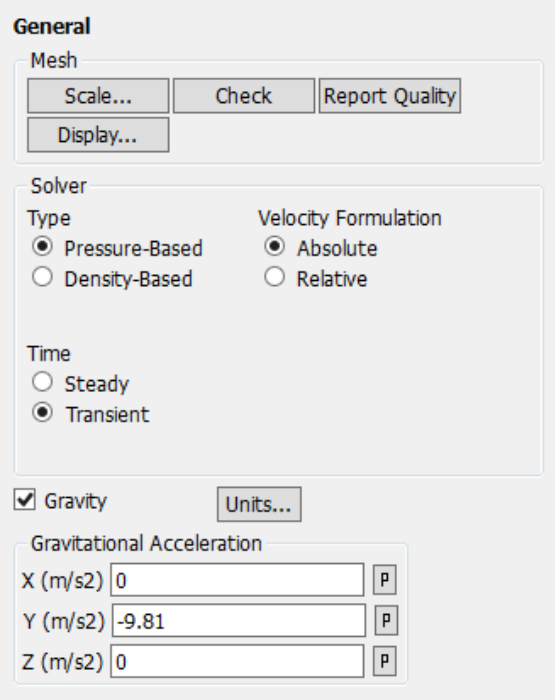

Fig. C.1: General Setup

Materials

We setup materials which we need in simulations in this section. The fluid in the study was water. The material of the block was copper. We input the properties based on the experiments.

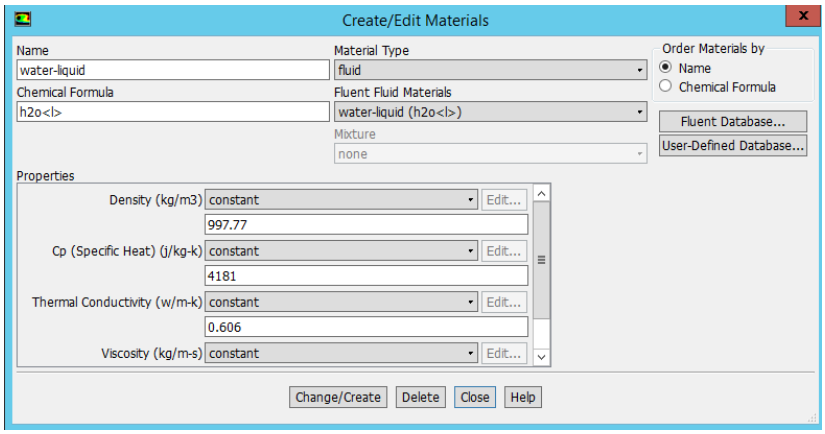

(a)

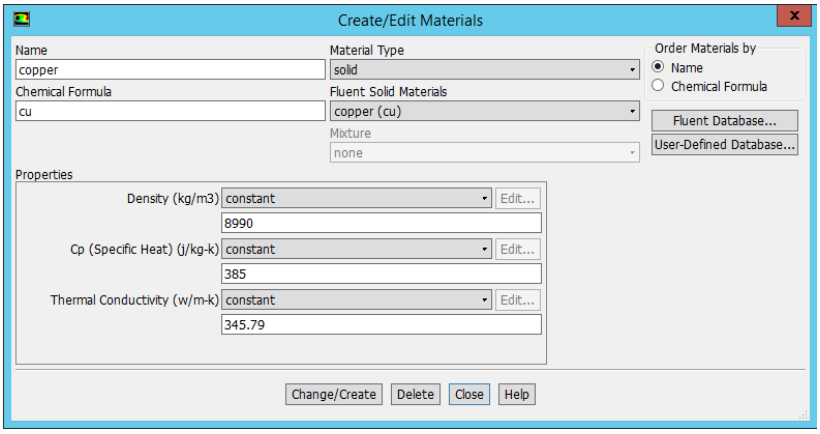

(b)

Fig. C.2: Materials used in the Numerical Simulations (a) Water (b) Copper

Boundary Conditions

We setup boundary conditions in Fig. C.3. Fig. C.3. (a) illustrates the regular boundary conditions. We can specify the velocity magnitude and fluctuating velocity algorithm with constant values or UDF. Fig. C.3 (b) shows the setup of periodic boundary conditions. We can specify mass flow rate of pressure gradient in the panel.

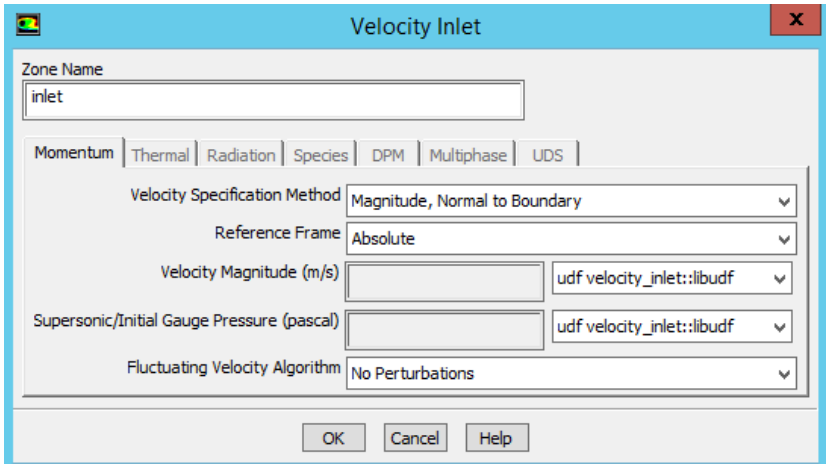

(a)

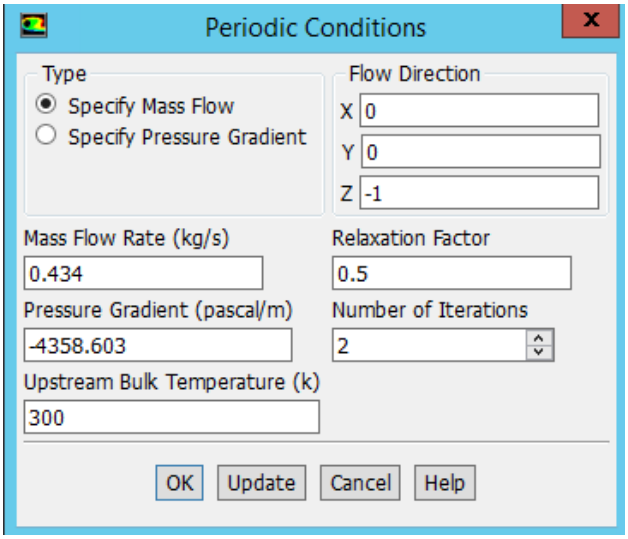

(b)

Fig. C.3: Boundary Conditions (a) Regular Boundary Conditions (b) Periodic Boundary Conditions

Solution Methods

Fig. C.4 shows the all the solution methods which used in the numerical simulations. The details of the solution methods can be found in ANSYS Fluent manual [55].

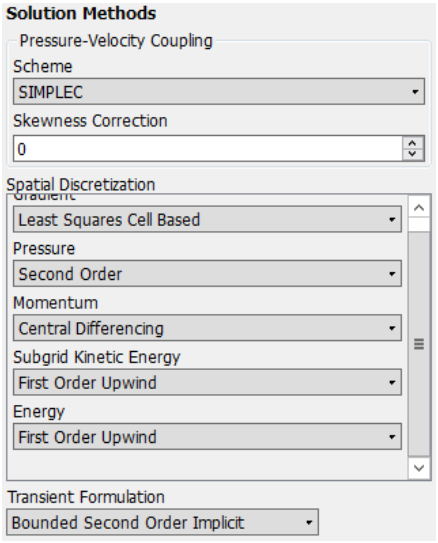

Fig. C.4: Solution Methods

Initialization

Fig. C.5 shows the initial conditions for the case with 1.8 m/s inlet velocity. Standard initialization and relative to cell zone were selected.

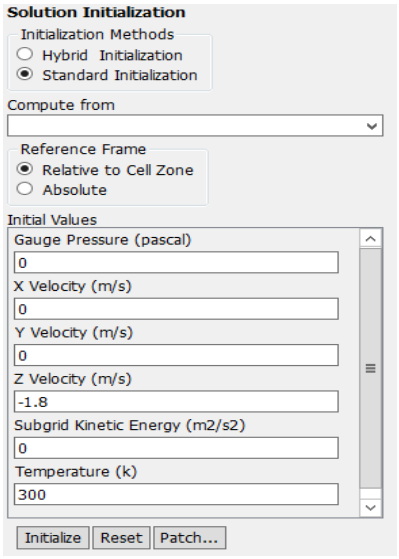

Fig. C.5: Initial Conditions

Data Output

Fig. C.6 shows the panel of automatic export during calculation. The output quantities can be specified in the panel. We can setup output frequency and output directory in this panel.

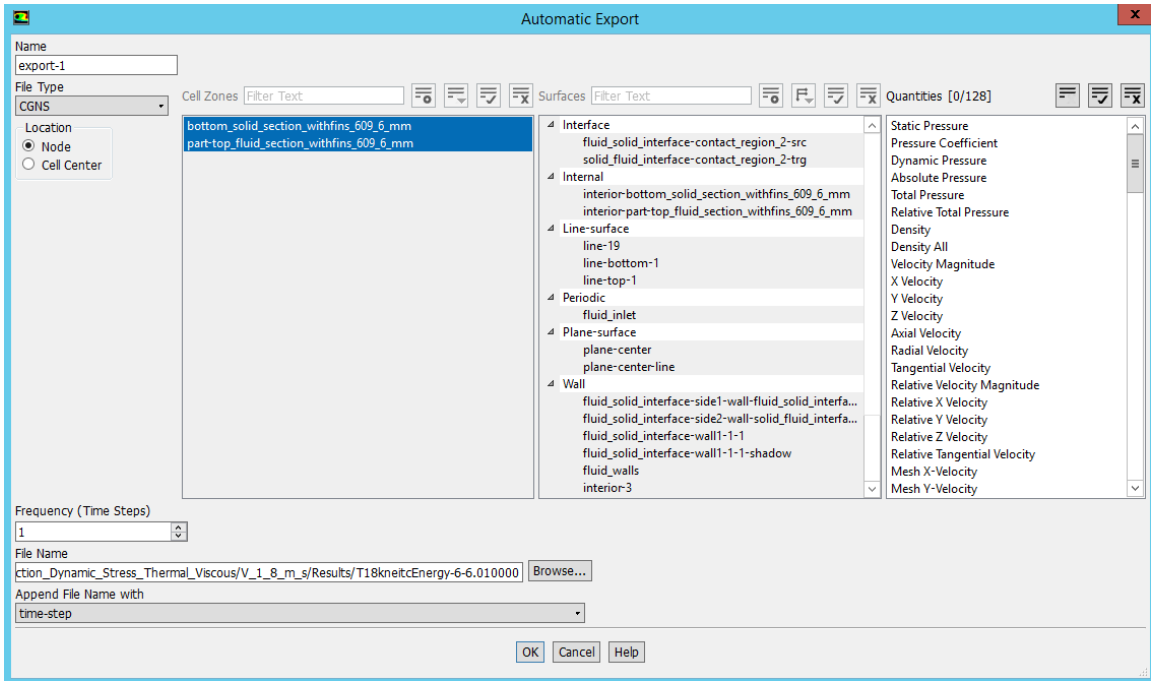

Fig. C.6: Setup for Data Output

Appendix D – User-Defined Function (UDF)

A user-defined function (UDF) is a function provided by the user of a program or environment [55]. In ANSYS Fluent, UDF can be used to customize boundary conditions.

Transient Velocity Profile

```
/************************************************************************
/* UDF for specifying a transient velocity profile boundary condition */
/************************************************************************
#include "udf.h"

DEFINE_PROFILE(velocity_inlet,thread,index)
{
 real x[ND_ND];  /* this will hold the position vector */
 real xx;
 real yy;
 face_t f;
 real t;
 real T=1;
 int i,j,n;
 int num=3;
 real vel[3][3];
 real velin;

 FILE *fp;
 fp=fopen("TS_03.txt","r");

 i=0; j=0;
 for(i=0; i<num; i++)
 {
  for (j=0; j<num; j++)
  {
   fscanf(fp, "%f", &vel[j][i]) ;
  }
 }
 fclose(fp);

 begin_f_loop(f,thread)
  {
   F_CENTROID(x,f,thread);
   xx=x[0];
   yy=x[1];
   F_PROFILE(f,thread,index)= vel[1][1];
```

```
   }
  end_f_loop(f,thread)
}
```

Steady Velocity Profile

```
/************************************************************************
/* unsteady.c */
/* UDF for specifying a transient temperature profile boundary condition */
/************************************************************************
#include "udf.h"
/* #include "math.h" */
DEFINE_PROFILE(velocity_inlet_1,thread,index)
{
  real x[ND_ND];  /* this will hold the position vector */
  real xx;
  real yy;
  face_t f;

  begin_f_loop(f,thread)
    {
      F_CENTROID(x,f,thread);
      xx=x[0];
      yy=x[1];


      if( xx >= -1.0 & xx <= 0.000762 && yy >= 0.0144378 && yy<= 0.02)
      {
      F_PROFILE(f,thread,index)= 0.494780484;
      }
      if( xx > 0.000762 & xx <= 0.001524 && yy >= 0.0144378 && yy<= 0.02)
      {
      F_PROFILE(f,thread,index)= 0.555170333;
      }
      if( xx > 0.001524 & xx <= 0.002178 && yy >= 0.0144378 && yy<= 0.02)
      {
      F_PROFILE(f,thread,index)= 0.56112179;
      }
      if( xx > 0.002178 & xx <= 0.003048 && yy >= 0.0144378 && yy<= 0.02)
      {
      F_PROFILE(f,thread,index)= 0.571804612;
      }
      if( xx > 0.003048 & xx <= 0.00381 && yy >= 0.0144378 && yy<= 0.02)
      {
      F_PROFILE(f,thread,index)= 0.5723879;
      }
```

```
if( xx > 0.00381 & xx <= 0.004572 && yy >= 0.0144378 && yy<= 0.02)
{
F_PROFILE(f,thread,index)= 0.586432589;
}
if( xx > 0.004572 & xx <= 0.005334 && yy >= 0.0144378 && yy<= 0.02)
{
F_PROFILE(f,thread,index)= 0.605578963;
}
if( xx > 0.005334 & xx <= 0.006096 && yy >= 0.0144378 && yy<= 0.02)
{
F_PROFILE(f,thread,index)= 0.620445896;
}
if( xx > 0.006096 & xx <= 0.006858 && yy >= 0.0144378 && yy<= 0.02)
{
F_PROFILE(f,thread,index)= 0.631818054;
}
if( xx > 0.006858 & xx <= 0.008 && yy >= 0.0144378 && yy<= 0.02)
{
F_PROFILE(f,thread,index)= 0.629497996;
}


if( xx >= -1.0 & xx <= 0.000762 && yy >= 0.0136357 && yy< 0.0144378)
{
F_PROFILE(f,thread,index)= 0.575661604;
}
if( xx > 0.000762 & xx <= 0.001524 && yy >= 0.0136357 && yy< 0.0144378)
{
F_PROFILE(f,thread,index)= 0.644613333;
}
if( xx > 0.001524 & xx <= 0.002178 && yy >= 0.0136357 && yy< 0.0144378)
{
F_PROFILE(f,thread,index)= 0.673464664;
}
if( xx > 0.002178 & xx <= 0.003048 && yy >= 0.0136357 && yy< 0.0144378)
{
F_PROFILE(f,thread,index)= 0.68478582;
}
if( xx > 0.003048 & xx <= 0.00381 && yy >= 0.0136357 && yy< 0.0144378)
{
F_PROFILE(f,thread,index)= 0.68222181;
}
if( xx > 0.00381 & xx <= 0.004572 && yy >= 0.0136357 && yy< 0.0144378)
{
F_PROFILE(f,thread,index)= 0.698029566;
}
```

```
    if( xx > 0.004572 & xx <= 0.005334 && yy >= 0.0136357 && yy< 0.0144378)
    {
    F_PROFILE(f,thread,index)= 0.680794566;
    }
……(Omitted Parts)……

    DEFINE_PROFILE(Turbulence_Kinetic_inlet_1,thread,index)
{
 real x[ND_ND];  /* this will hold the position vector */
 real xx;
 real yy;
 face_t f;

 begin_f_loop(f,thread)
   {
    F_CENTROID(x,f,thread);
    xx=x[0];
    yy=x[1];

    if( xx >= -1.0 & xx <= 0.000762 && yy >= 0.0144378 && yy<= 0.02)
    {
    F_PROFILE(f,thread,index)= 0.01785426;
    }
    if( xx > 0.000762 & xx <= 0.001524 && yy >= 0.0144378 && yy<= 0.02)
    {
    F_PROFILE(f,thread,index)= 0.021966533;
    }
    if( xx > 0.001524 & xx <= 0.002178 && yy >= 0.0144378 && yy<= 0.02)
    {
    F_PROFILE(f,thread,index)= 0.024489561;
    }
    if( xx > 0.002178 & xx <= 0.003048 && yy >= 0.0144378 && yy<= 0.02)
    {
    F_PROFILE(f,thread,index)= 0.026334981;
    }
    if( xx > 0.003048 & xx <= 0.00381 && yy >= 0.0144378 && yy<= 0.02)
    {
    F_PROFILE(f,thread,index)= 0.027884568;
    }
    if( xx > 0.00381 & xx <= 0.004572 && yy >= 0.0144378 && yy<= 0.02)
    {
    F_PROFILE(f,thread,index)= 0.02854237;
    }
    if( xx > 0.004572 & xx <= 0.005334 && yy >= 0.0144378 && yy<= 0.02)
    {
    F_PROFILE(f,thread,index)= 0.0304589622;
```

```
    }
    if( xx > 0.005334 & xx <= 0.006096 && yy >= 0.0144378 && yy<= 0.02)
    {
    F_PROFILE(f,thread,index)= 0.03122367;
    }
    if( xx > 0.006096 & xx <= 0.006858 && yy >= 0.0144378 && yy<= 0.02)
    {
    F_PROFILE(f,thread,index)= 0.032210045;
    }
    if( xx > 0.006858 & xx <= 0.008 && yy >= 0.0144378 && yy<= 0.02)
    {
    F_PROFILE(f,thread,index)= 0.03167537;
    }
……(Omitted Parts)……

DEFINE_PROFILE(Turbulence_Dissipation_Rate_1,thread,index)
{
 real x[ND_ND];  /* this will hold the position vector */
 real xx;
 real yy;
 face_t f;

 begin_f_loop(f,thread)
   {
    F_CENTROID(x,f,thread);
    xx=x[0];
    yy=x[1];

    if( xx >= -1.0 & xx <= 0.000762 && yy >= 0.0144378 && yy<= 0.02)
    {
    F_PROFILE(f,thread,index)= 2.526930286;
    }
    if( xx > 0.000762 & xx <= 0.001524 && yy >= 0.0144378 && yy<= 0.02)
    {
    F_PROFILE(f,thread,index)= 2.642498429;
    }
    if( xx > 0.001524 & xx <= 0.002178 && yy >= 0.0144378 && yy<= 0.02)
    {
    F_PROFILE(f,thread,index)= 2.681341186;
    }
    if( xx > 0.002178 & xx <= 0.003048 && yy >= 0.0144378 && yy<= 0.02)
    {
    F_PROFILE(f,thread,index)= 2.787938817;
    }
    if( xx > 0.003048 & xx <= 0.00381 && yy >= 0.0144378 && yy<= 0.02)
    {
```

```
F_PROFILE(f,thread,index)= 2.879388104;
}
if( xx > 0.00381 & xx <= 0.004572 && yy >= 0.0144378 && yy<= 0.02)
{
F_PROFILE(f,thread,index)= 3.0236971;
}
if( xx > 0.004572 & xx <= 0.005334 && yy >= 0.0144378 && yy<= 0.02)
{
F_PROFILE(f,thread,index)= 3.256987412;
}
if( xx > 0.005334 & xx <= 0.006096 && yy >= 0.0144378 && yy<= 0.02)
{
F_PROFILE(f,thread,index)= 3.403698;
}
if( xx > 0.006096 & xx <= 0.006858 && yy >= 0.0144378 && yy<= 0.02)
{
F_PROFILE(f,thread,index)= 3.510239929;
}
if( xx > 0.006858 & xx <= 0.008 && yy >= 0.0144378 && yy<= 0.02)
{
F_PROFILE(f,thread,index)= 3.539074071;
}
```

……(Omitted Parts)……

```
if( xx >= -1.0 & xx <= 0.000762 && yy >= -1.0 && yy<= 0.0008021)
{
F_PROFILE(f,thread,index)= 2.526930286;
}
if( xx > 0.000762 & xx <= 0.001524 && yy >= -1.0 && yy<= 0.0008021)
{
F_PROFILE(f,thread,index)= 2.642498429;
}
if( xx > 0.001524 & xx <= 0.002178 && yy >= -1.0 && yy<= 0.0008021)
{
F_PROFILE(f,thread,index)= 2.681341186;
}
if( xx > 0.002178 & xx <= 0.003048 && yy >= -1.0 && yy<= 0.0008021)
{
F_PROFILE(f,thread,index)= 2.787938817;
}
if( xx > 0.003048 & xx <= 0.00381 && yy >= -1.0 && yy<= 0.0008021)
{
F_PROFILE(f,thread,index)= 2.879388104;
}
if( xx > 0.00381 & xx <= 0.004572 && yy >= -1.0 && yy<= 0.0008021)
```

```
    {
    F_PROFILE(f,thread,index)= 3.0236971;
    }
    if( xx > 0.004572 & xx <= 0.005334 && yy >= -1.0 && yy<= 0.0008021)
    {
    F_PROFILE(f,thread,index)= 3.256987412;
    }
    if( xx > 0.005334 & xx <= 0.006096 && yy >= -1.0 && yy<= 0.0008021)
    {
    F_PROFILE(f,thread,index)= 3.403698;
    }
    if( xx > 0.006096 & xx <= 0.006858 && yy >= -1.0 && yy<= 0.0008021)
    {
    F_PROFILE(f,thread,index)= 3.510239929;
    }
    if( xx > 0.006858 & xx <= 0.008 && yy >= 0.0 && yy<= 0.0008021)
    {
    F_PROFILE(f,thread,index)= 3.539074071;
    }
   }
  end_f_loop(f,thread)
}
```

Appendix E – Setup in TSI 4G Insight

General Setup

Before capturing images, we need to specify and set values for the hardware components. Fig. E.1 describes how to set the parameters for the following hardware components: synchronizer, camera and laser.

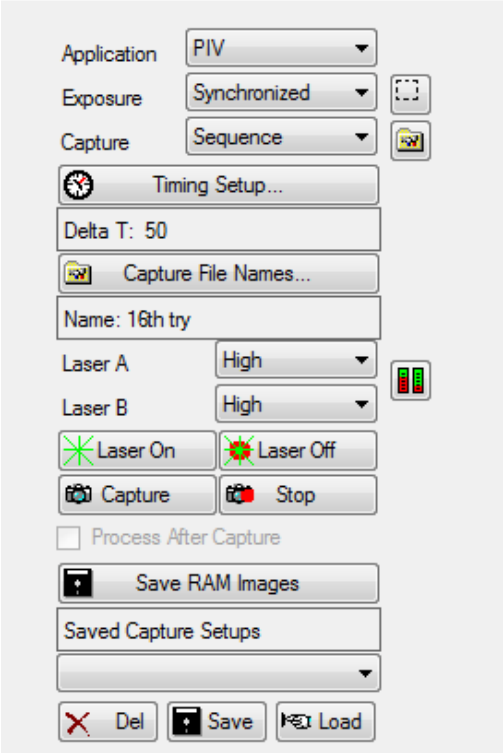

Fig. E.1: General Setup

Capture Timing Setup

Depending on our application, we need to adjust the timing for the selected hardware components to help capture the desired images. All the options to set timing are available in the Capture Timing Setup dialog box (shown in Fig. E.2).

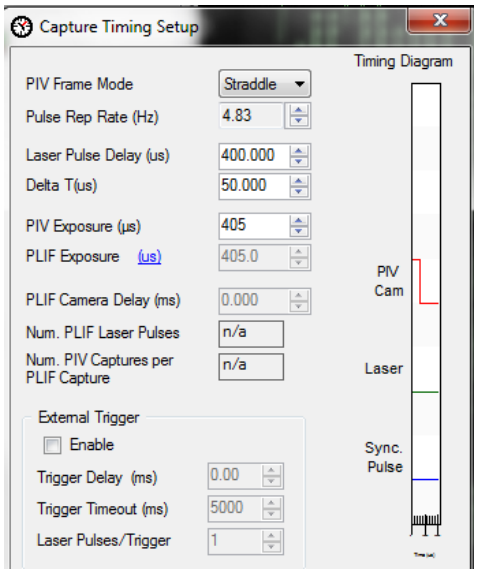

Fig. E.2: Capture Timing Setup

2D Spatial Calibration

Fig. E.3 shows 2D spatial calibration. It allows us to enter a calibration factor to compute the flow velocity using meters per second. In the study, the object size was 3 mm and 2048 pixels.

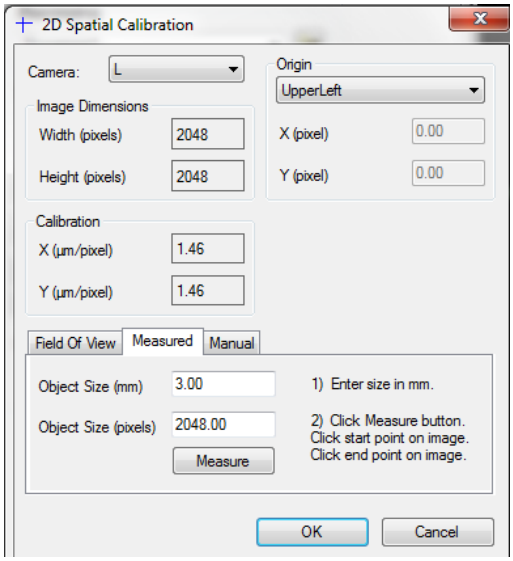

Fig. E.3: 2D Spatial Calibration

PIV Processor Setup

Fig. E.4 shows PIV processor setup. We had to specify the starting spot dimensions and final spot dimensions. Insight software implements PIV processing algorithm in the following four plugin engines: (1) grid engines, (2) spot mask engines, (3) correlation engines, and (4) peak engines.

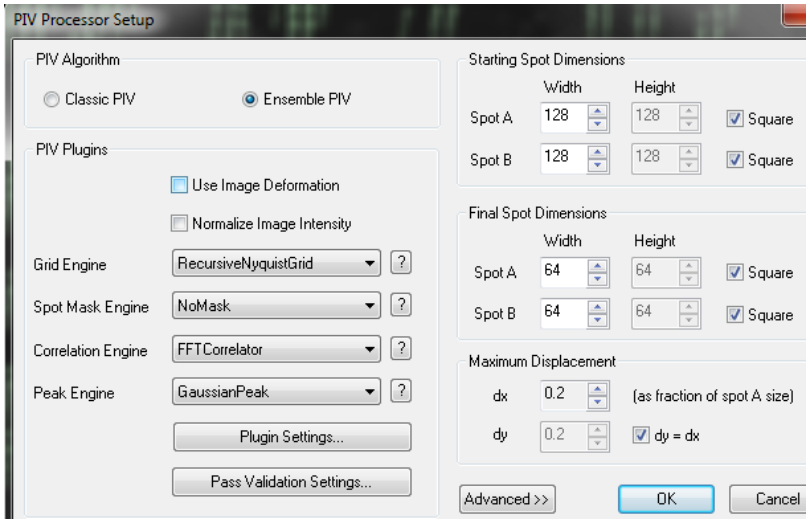

Fig. E.4: PIV Processor Setup

Appendix F – LabView Program

To monitor and output the experimental data, we made program in Labview. All experimental data we needed were displayed and output from LabView.

Water Loop Panel

Fig. F.1 shows water loop panel. It displays mass flow rate, water density, inlet/outlet pressures, Reynolds number, and inlet/outlet temperatures.

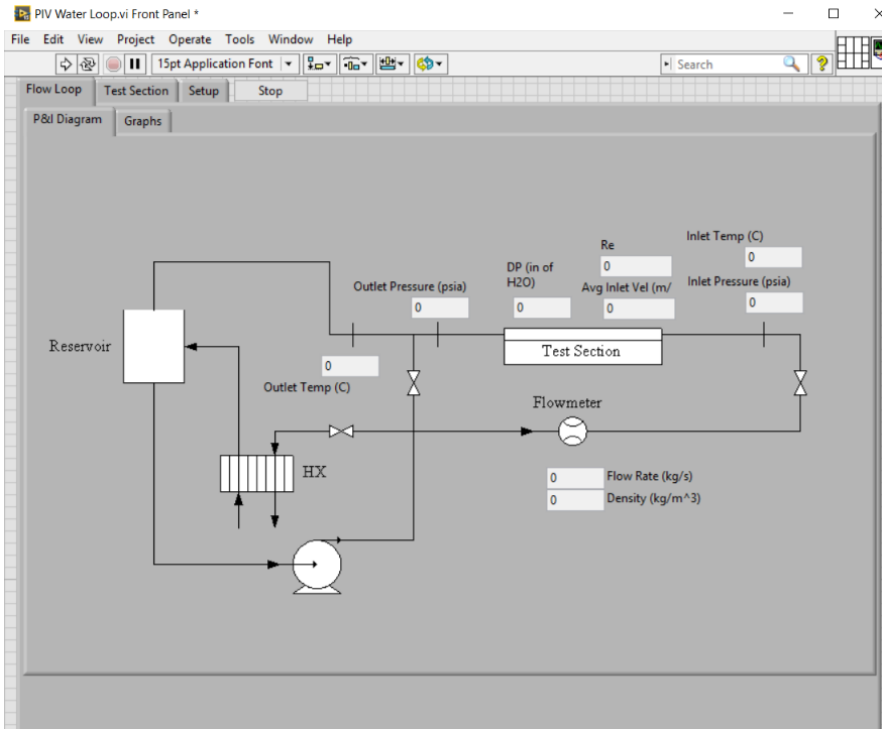

Fig. F.1: Water Loop Panel

Test Section Panel

Fig. F.2 shows the test section panel. It displayed all the quantities in the test section, i.e. the copper block. We used temperature profiles on the block to get the heat flux and the surface temperatures.

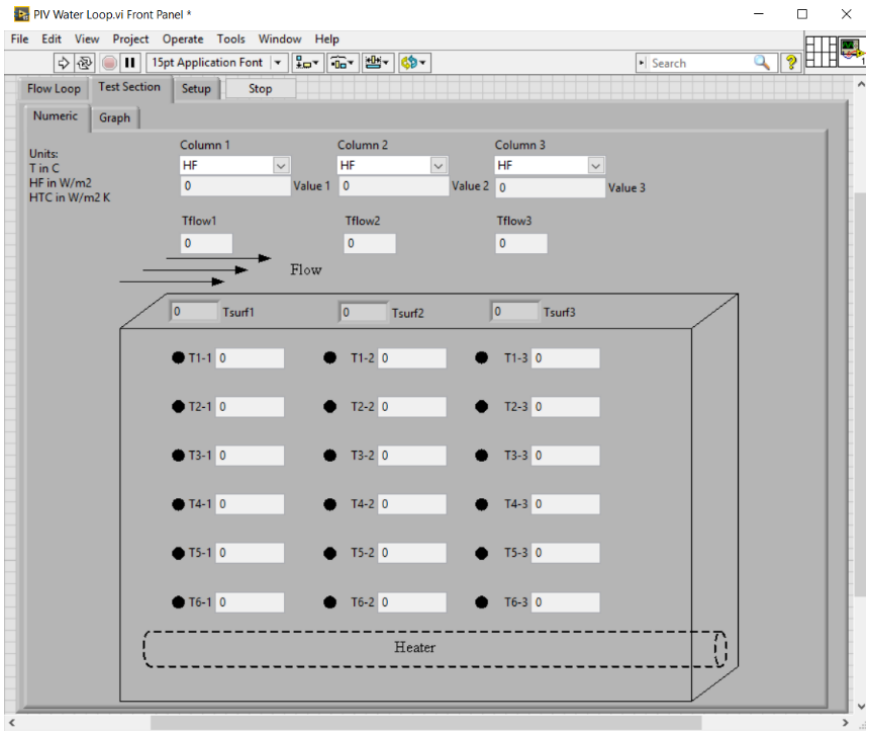

Fig. F.2: Test Section Panel

Data Output Panel

Fig. F.3 shows the data output panel. We setup output frequency and output directory in this panel.

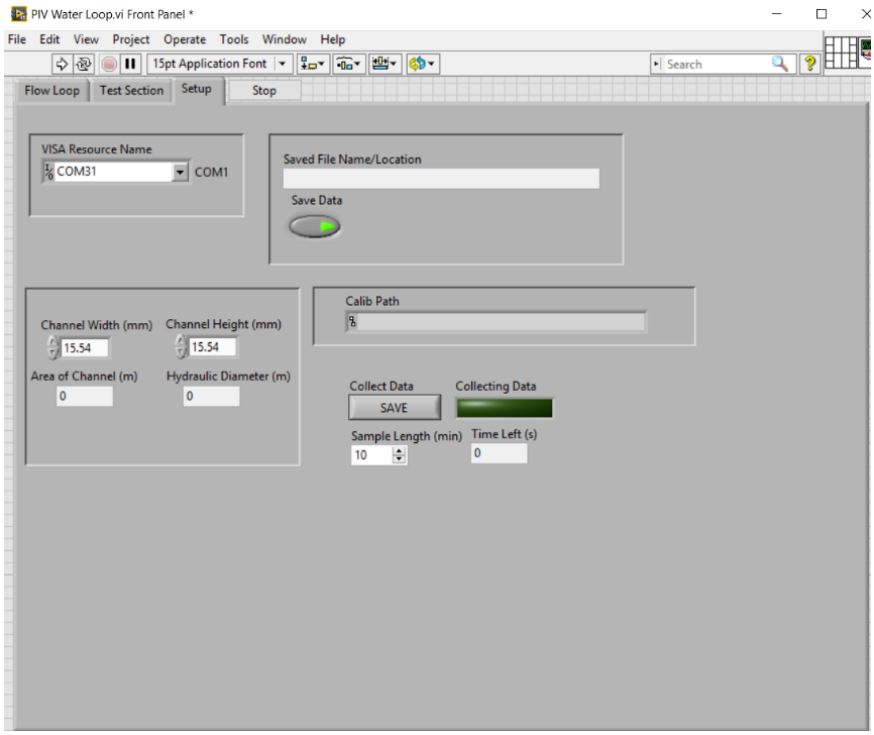

Fig. F.3: Data Output Panel